Modelling the diurnal variation of sea surface temperature using a one-dimensional ocean turbulence model

Stephen Hallsworth

Doctor of Philosophy

2005

Declaration

This thesis has been composed by myself and all work reported herein is my own except where otherwise stated.

Stephen Hallsworth

For my mum and my dear sister Sally

Acknowledgements

A huge thanks to my supervisor, Chris Merchant. His boundless patience, insight and encouragement saw me through the enormous task of producing this work. Without him of course this thesis would have been impossible.

Thanks also to the following people:

Massimo Vieno my climbing buddy, drinking buddy and good friend. Thanks for all your help with computers Massimo!

Helen Kettle a brilliant postdoc and moreover a great friend in times of need.

Nicholas Fournier and Hannah Clark, true friends when I needed you.

Angela, for all the fun times and laughs.

Mum, Dad and Sally for all their support.

All the other PhD students and postdocs at the institute, it was great working alongside you all.

All the teaching staff in the institute for their input.

Abstract

Sea surface temperature (SST) is an important parameter in ocean and atmospheric sciences. Direct measurements of air-sea fluxes are too few to enable accurate global estimates with good resolution. Therefore the fluxes must be parameterised and SST is a critical parameter. Accurate air-sea fluxes are essential to climate change studies, numerical weather forecasting, hurricane prediction, oceanic general circulation modelling and ocean data assimilation. As an example of the scientific role of accurate, high-resolution SST, the Global Ocean Data Assimilation Experiment (GODAE) requires that SST be resolved at a spatial resolution of 5 to 10 km at 6 hour intervals or better, with an accuracy of 0.1 to 0.2 °C.

Solar radiation warms the ocean surface during the day. During periods of low wind, there is little mixing at the surface and with strong solar heating, the sea surface temperature can warm to several degrees above the SST of the previous night. This is known as diurnal-warming of the SST and it must be accounted for when interpreting SST measurements since the SST can significantly vary with the time of day that the measurements are taken. Also, the depth at which the SST is measured can be critical, since thermal stratification near the surface is associated with strong diurnal-warming. With strong diurnal-warming, the temperature at the air-sea interface could be several degrees warmer than the temperature at one or two metres depth. To correctly interpret SST measurements during conditions of diurnal-warming of SST, the diurnal response to environmental conditions must be understood.

This thesis is a study of the response of diurnal-warming of SST to the primary environmental conditions that cause it. A one-dimensional ocean turbulence model is used to simulate the diurnal-cycle of warming of SST. The model is developed and enhanced to enable accurate predictions of

amplitudes of the night to day difference in SST and the stratification associated with strong warming events. The enhanced model is validated with data from in-situ instrumented-moorings. The model is used to investigate the shape and timing of the warming response to environmental causes, including the timing of those causes.

The one-dimensional turbulence model must be forced with air-sea fluxes. Available data sets for these fluxes have various temporal resolutions, from just a few minutes (high-resolution) to daily averages. The performance of the model is tested against temporal resolution of the air-sea fluxes. This allows for a realistic interpretation of the modelled SST for applications where data is only available at low temporal resolution.

SSTs from the Meteosat Second Generation (MSG) (now called Meteosat 8) satellite have recently become available. SSTs (at the air-sea interface) from the new model are compared with the satellite SSTs at buoy locations in the Atlantic and show useful agreement with the shape and amplitude of the diurnal cycle for several events, (within the limits imposed by the low-resolution forcing data presently available for the satellite / buoy match-ups).

Chapter 1 Introduction 4

1.1 Fluxes 5

1.1.1 Ocean surface heat energy budget 6

1.1.2 Momentum transfer (wind stress) 7

1.2 Oceanic temperature profiles near the surface 8

1.2.1 Diurnal warming 8

1.2.2 Skin-bulk sea surface temperature difference 9

1.2.3 Classification of the vertical structure of SST 13

1.3 Turbulence and range of scales 15

1.4 Consequences of diurnal warming and the cool skin for fluxes 17

1.5 Consequences of diurnal warming and the cool skin for ocean modelling 18

1.6 Scope of the thesis 19

1.7 Layout of the thesis 20

Chapter 2 Comparison of mixing models 23

2.1 Convective-adjustment models 24

2.2 Bulk mixed layer models 24

2.3 Turbulence closure models 26

2.4 Comparison of the GOTM turbulence closure and PWP models 27

2.4.1 Comparison of simulation of sea surface temperatures (GOTM vs. PWP). 28

2.4.2 Comparison of simulation of temperature profiles to 10 m (GOTM vs. PWP) 30

2.4.3 Summary of PWP vs. GOTM 34

2.5 How the GOTM model works 36

2.5.1 Dynamical Module 37

2.5.2 Eddy-viscosity and eddy-diffusivity 39

2.5.3 Turbulence Module. 40

2.5.4 Stability functions 41

2.6 Model resolution 46

2.7 Summary 48

Chapter 3 Fluxes background 49

3.1 Short-wave radiation – the Solar flux 50

3.1.1 Radiative transfer in the atmosphere 51

3.1.2 Dividing the spectrum into a number of discrete bands 53

3.1.3 The attenuation of the entrant solar radiation within the water column 54

3.1.4 2 bands 55

3.1.5 9 bands 55

3.1.6 *278 bands* 56
3.1.7 *Proportions of SSI and attenuation lengths comparisons* 61
3.1.8 *Model grid and SSI attenuation* 62
3.1.9 *Geometrical modifications* 66
3.1.10 *Short wave radiation summary* 68
3.2 *Turbulent flux forcing* 69
3.2.1 *Methods of obtaining the turbulent fluxes* 69
3.2.2 *Vertical fluxes at the surface* 70
3.2.3 *Surface roughness and the Charnock formula* 72
3.2.4 *Monin Obukhov Similarity Theory (MOST)* 75
3.2.5 *Transfer coefficients* 78
3.2.6 *Options* 79
3.2.7 *Implementing turbulent flux options in GOTM* 83
3.3 *Downwelling longwave radiation* 83
3.3.1 *Longwave radiation and cloud fraction.* 85
3.4 *Turbulence mixing scheme* 87
3.5 *Ocean-leaving flux forcing* 88
3.6 *Summary* 89

Chapter 4 Testing combinations of options 90
4.1 *Data Sets* 92
4.2 *Definitions of properties for testing model skill* 95
4.3 *Root mean square of residuals* 98
4.4 *Approach to selecting the best combinations* 99
4.5 *Option-set 1, turbulence closure model* 100
4.6 *Option set 3, Longwave radiation* 103
4.6.1 *A note on model stability for some combinations* 106
4.6.2 *Lowest 10 RMS of residuals of various properties* 106
4.6.3 *Detailed observations* 107
4.7 *Option-set 5: Pre-calculated fluxes versus interactively calculated fluxes* 110
4.7.1 *Analysis by RMS of residuals comparison.* 116
4.8 *Option set 4 Non – radiative flux calculation from meteorology, including wind stress* 116
4.9 *Option-set 2 - Short wave radiation parameterisation* 120
4.10 *Time series comparisons of original and improved models* 122
4.10.1 *Statistical comparisons of original and improved models.* 127
4.11 *Validation data sets* 128

4.12 Summary 131

Chapter 5 Model response to meteorological forcing 132

5.1 Sensitivity test of model skill to the resolution of forcing data 133

5.2 Alternatives to in situ data: ECMWF meteorological data and calculated SSI. 141

5.3 Summary 150

Chapter 6 Comparisons with SST from Meteosat Second Generation 151

6.1 Motivation 151

6.2 The Data 152

6.2.1 The Meteosat 8 satellite 152

6.2.2 PIRATA data 155

6.3 High-resolution satellite – buoy match-ups 155

6.4 Low-resolution satellite – buoy match-ups 159

6.4.1 Methodology for producing 6-hourly forcing fluxes 159

6.5 Testing this methodology 161

6.6 Chapter 6 summary 169

Chapter 7 Conclusions and further work 171

7.1 Ocean model 171

7.2 Solar radiation distribution. 172

7.3 Modelled SST sensitivity to fluxes, SSI distribution and turbulence model 173

7.4 Model sensitivity to forcing data resolution 174

7.5 Sources of data alternative to in situ data 174

7.6 Modelled SSTs compared to satellite SSTs 175

7.7 Further Work 176

7.7.1 Validation of the model for large diurnal amplitudes 176

7.7.2 Investigation of more properties of the diurnal cycle 176

7.7.3 Longer time scales 180

Chapter 1 Introduction

Sea surface temperature (SST) is the basic ocean variable which influences the magnitude of the surface turbulent fluxes and also the upward flux of longwave radiation. Accurate air-sea fluxes are essential to climate change studies, numerical weather forecasting, hurricane prediction, oceanic general circulation modelling (OGCM) and ocean data assimilation.

The tropical oceans play a major role in climate variability. The tropical regions of Earth possess the warmest SSTs and the deepest atmospheric convection with the large scale convection constrained to lie within the 28 °C SST contour (Webster,1994). Fairall et al. (1996a) have shown that to estimate the surface energy budget in the tropical ocean to within 10 W m^{-2} requires SST accuracy to within ±0.2 K. An important international programme on ocean data assimilation, the Global Ocean Data Assimilation Experiment (GODAE), requires that SST be resolved at a spatial resolution of 5 to 10 km at 6 hour intervals or better, with an accuracy of 0.1 to 0.2 °C.

The research presented in this thesis focuses on the diurnal variation of SST in the tropical oceans. Solar radiation reaches the highest intensities in the tropics and the tropical oceans exhibit the largest day-to-night variations in SST. The aim is to understand the environmental processes involved in SST variability and improve existing methods of SST prediction using routinely observed meteorological parameters. Before defining why diurnal warming of SST is important to geophysical research, the characteristic features and the principal causes of diurnal warming are explained below.

1.1 Fluxes

The principal environmental processes that affect SST are illustrated in Figure 1.1

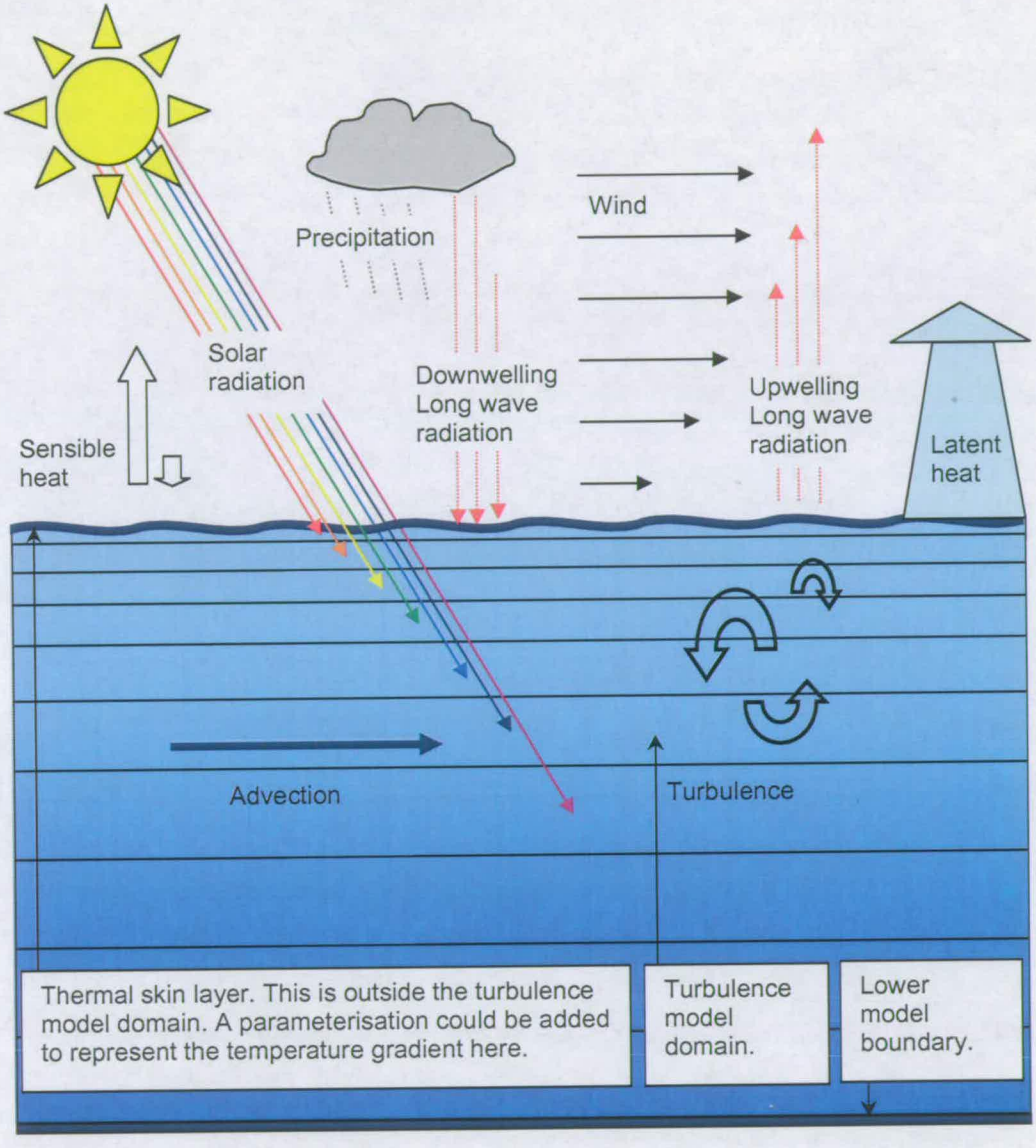

Figure 1.1 Schematic of the atmosphere / ocean fluxes and an ocean model domain

The two major influences on diurnal warming are the air-sea heat fluxes and the momentum transferred to the ocean by the wind.

1.1.1 Ocean surface heat energy budget

The budget of heat energy at the air-sea interface is represented by the sum of the fluxes of heat to and from the ocean. Heat fluxes are the amount of heat energy passing through a given area in a given time (i.e. power per unit area) and the units used throughout this thesis are W m^{-2}.

The surface heat energy budget for a column of the ocean is

$$H_{net} = H_{rad} + H_L + H_S + H_{PR} + H_{adv} \tag{1.1}$$

where H_{net} is the ocean heat balance, H_{rad} is the sum of net solar radiation and longwave fluxes at the surface, H_L and H_S are the surface turbulent fluxes of latent and sensible heat respectively, H_{PR} is the heat transfer by precipitation and H_{adv} is net heat energy transport by advection.

The net surface radiation flux H_{rad} is given by

$$H_{rad} = (1-\alpha)H_{SSI} + H_{LW} - \varepsilon\sigma T^4 \tag{1.2}$$

where H_{SSI} is the downwelling solar radiation at the surface or surface solar irradiance (SSI), α is the surface albedo (for solar radiation), H_{LW} is the downwelling longwave radiation at the surface (from the atmosphere and clouds), T is the surface temperature, σ is the Stefan-Boltzmann constant and ε is the longwave emissivity. The last two terms on the right hand side of equation (1.2) define the net longwave radiation at the air-sea interface. The various oceanic heat sources and sinks are presented in detail in chapter 3. A positive H_{net} provides a source for diurnal warming and potentially stable thermal stratification at the surface.

1.1.2 Momentum transfer (wind stress)

The wind exerts a shear stress at the surface and the vertical flux of momentum must be continuous across the air-sea interface. Momentum is transferred by this shear stress. The shear stress transferred to the ocean is a source of mixing (wind induced mixing) and acts to reduce diurnal warming and to erode any surface stratification. Continuity of stresses across the interface gives:

$$\tau_a + \tau_{pr} = \tau_w + \tau_{wv} \tag{1.3}$$

where τ_a is the air-side wind stress, τ_w is the water-side shear stress, τ_{wv} is the momentum flux radiated out by wind-generated propagating surface waves and τ_{pr} is the momentum flux due to precipitation. τ_w is the drag exerted by the ocean on the atmosphere. Through this term, momentum is directly transferred to the ocean currents. For a fully developed wave field, momentum flux generating the waves is immediately transferred to the ocean currents and τ_{wv} can be neglected. In the absence of precipitation, $\tau_w = \tau_a$.

Direct measurements of air-sea fluxes are too few to enable accurate global estimates with good resolution. The fluxes must be parameterised in terms of readily available meteorological observations. Details of current theory and various parameterisations are given in chapters 3 and 4.

1.2 Oceanic temperature profiles near the surface

Figure 1.2 illustrates typical temperature profiles when diurnal warming occurs. In the absence of sufficient wind mixing, strong solar heating produces warming within a shallow surface layer (Price et al., 1986).

1.2.1 Diurnal warming

With strong solar heating, the warm surface layer can be as shallow as one metre with night to day temperature differences at a given depth, (the diurnal amplitude) reaching as much as 3.5 °C (Stramma et al. 1986). Flament *et al.* (1994) report that under extreme conditions, the diurnal amplitude can reach 6 °C.

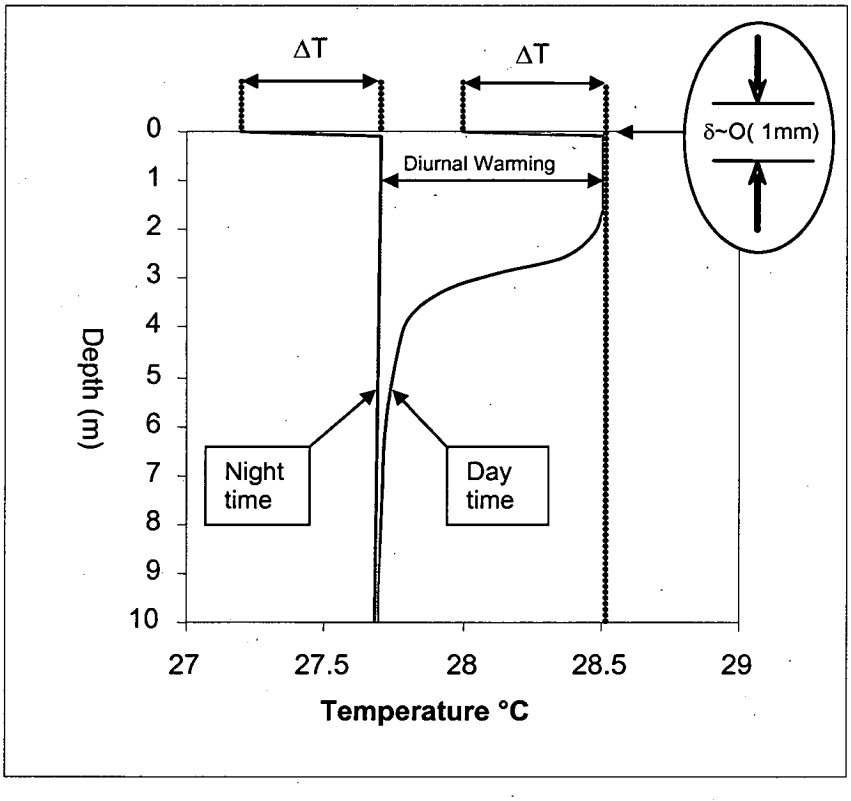

Figure 1.2 Schematic of a near surface temperature profile with diurnal warming.

An example of the modelled temperature profile response to solar radiation and wind speed is illustrated in Figure 1.3.

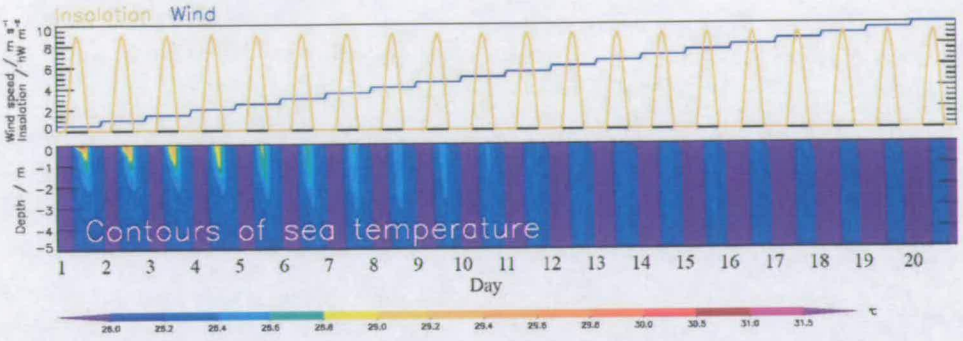

Figure 1.3 20 days of model derived contours of sea temperature in the top 5m of water. Solar radiation is synthesised for clear skies at 0N 0W. Start day is 1st January 2000. Constant wind during the day increases every 24 hours by 0.5 m/s at midnight.

1.2.2 Skin-bulk sea surface temperature difference

Another feature of the temperature profile is a temperature gradient that persists in a very thin layer at the surface and is known as the cool skin. The temperature distribution within the cool skin is illustrated in Figure 1.4. Field observations suggest that the skin sea surface temperature (see Section 1.2.3) can be 0.1 to 0.5 °C cooler than water a few centimetres deeper, Robinson et al (1984). The characteristic depth δ of the cool skin is O(1mm).

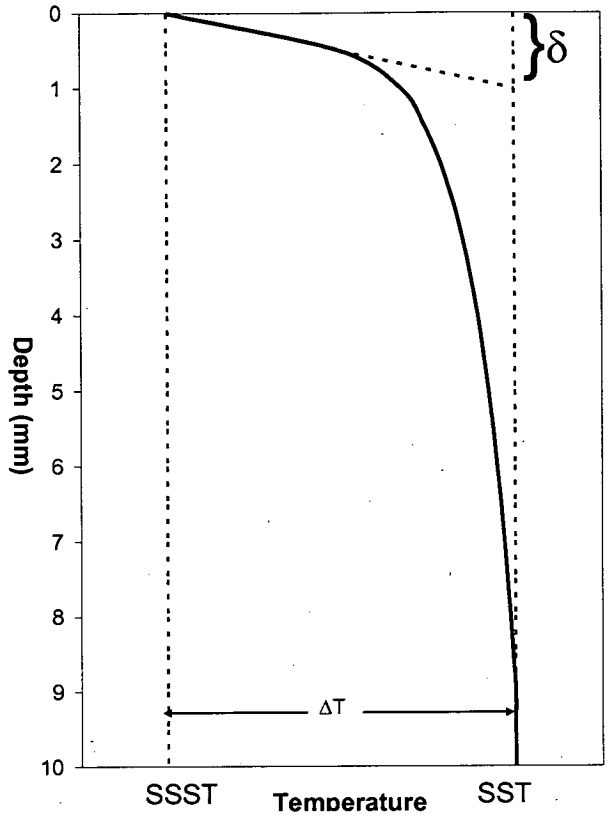

Figure 1.4 Schematic diagram of the vertical distribution in the cool skin of the ocean. SSST is the surface temperature, SST is the bulk temperature and δ is the characteristic thickness of the conduction sublayer (after Paulson and Simpson 1981).

The cool skin is caused by a combination of sources and sinks of heat and the suppression of turbulent mixing at the interface. Although some fraction of the solar irradiance is absorbed in the top 1mm of the ocean, the majority of the radiation is absorbed and transformed into heat energy at greater depths. This heat energy is distributed to greater depths by wind-induced shear. A temperature difference must exist for heat to move from depth to the skin. An unbroken sea surface inhibits turbulent motion near the surface and so the heat transport there must occur by molecular conduction, thereby supporting comparatively large temperature gradients (Robinson et al 1984). Although it is almost always present, it can be destroyed by breaking waves or precipitation.

Parameterisation of the cool skin

The majority of the temperature drop occurs in the conduction sublayer, of characteristic thickness 1 mm. The thickness of the conduction sublayer δ is dependent upon the wind speed and can be parameterised as

$$\delta = \frac{\upsilon}{\left(\tau/\rho_w\right)^{1/2}} \tag{1.4}$$

where ν is the viscosity, τ is the wind induced shear stress and ρ_w is the density of water (Saunders, 1967). Given δ, ΔT can be calculated as follows

$$\Delta T = \frac{Q\delta}{k} \tag{1.5}$$

where Q is the total outgoing heat flux and k is the thermal conductivity.

Typical values of these parameters are given in table 1.1.

Parameter	Typical values
Viscosity ν	10^{-6} m^2s^{-1} at 20 °C
Wind-induced shear stress τ	~0.01 Nm^{-2} at 2 ms^{-1} (depends on atmospheric stability)
Density ρ_w (at the sea surface)	1020 to 1030 kgm^{-3}
Thermal conductivity	0.6 $Wm^{-1}K^{-1}$ at 30 °C

Table 1. 1 Typical values of ocean parameters pertaining to cool skin temperature parameterisation.

Zonal mean values of heat fluxes are given Figure 1.5. The total outgoing heat flux is the sum of the latent, sensible and net longwave heat fluxes.

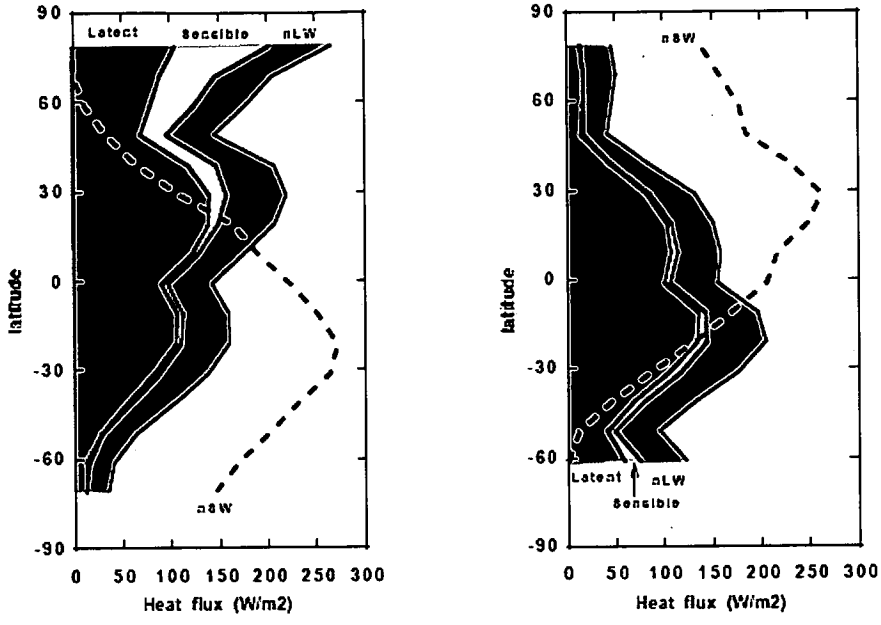

Figure 1. 5 Zonal mean values of flux components derived from the SOC climatology for (a) January; (b) July, reproduced from Taylor, *et al.*, (October, 1999).

The parameterisation for ΔT, equation (1.5) was formulated for night time conditions but should be applicable during the day provided that solar heating of the skin layer is accounted for. Defant (1961) suggests that 15% of the energy in the direct solar beam is absorbed in the top 1 mm of the ocean. Saunders (1967) suggested integrating the solar radiation over the depth δ and adjusting the heat in the formula for ΔT by this amount.

Therefore, Q in equation 1.5 is replaced by:

$$Q - \frac{1}{\delta}\int_0^{\delta}(I_0 - I)dz \qquad (1.6)$$

Where I is the insolation at depth z and I_0 is the surface value (SSI).

The response of ΔT to wind using equation (1.5) (with adjusted heat) is shown in Figure 1.6 and the solar heat absorbed by the skin is shown in Figure 1.7.

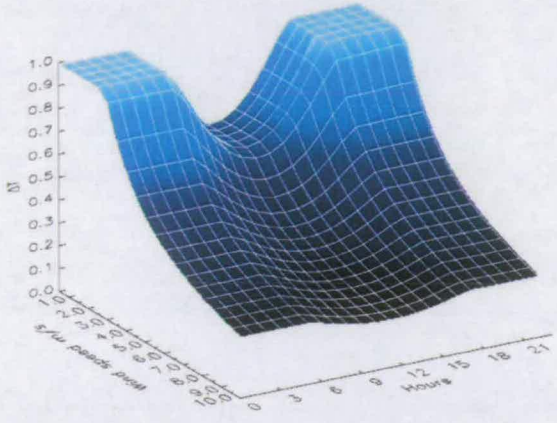

Figure 1.6 Response of ΔT to wind speed and solar absorption given a constant heat flux from the ocean, (upwelling heat flux set to 310 W/m2 to balance the insolation).

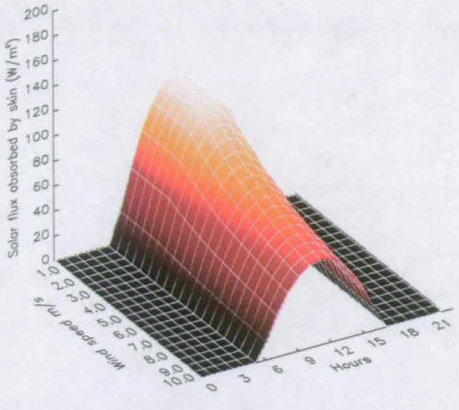

Figure 1.7 Absorption of solar flux in the cool skin.

1.2.3 Classification of the vertical structure of SST

It is clear from the above that there is not a single definitive SST and the concept of SST needs some analysis. The classification of the vertical structure of SST given below follows Donlon *et al.*, (2002).

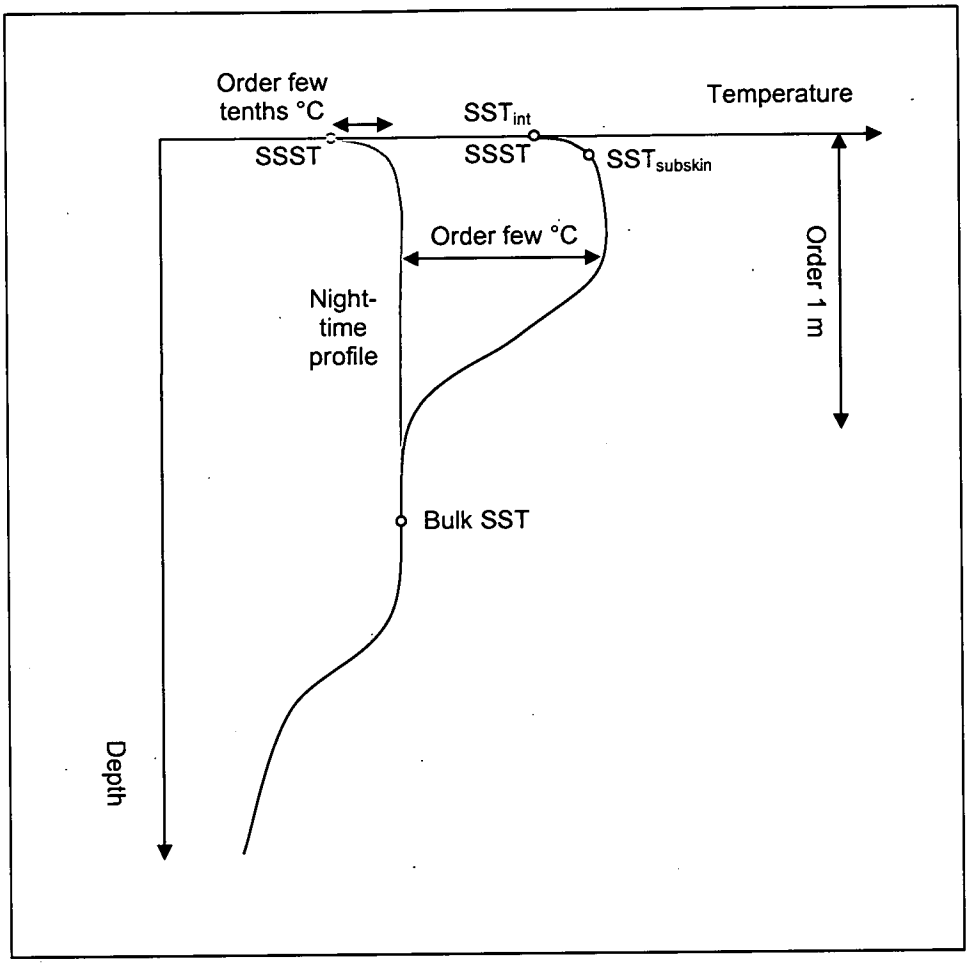

Figure 1.8. Schematic of typical temperature profiles with (black profile) and without (grey profile to 'Bulk SST') strong surface warming, illustrating various definitions of sea surface temperature.

The interface temperature (SST_{int}) is the temperature at the exact air-sea interface.

The skin sea surface temperature (SSST) is a temperature as measured by a radiometer (infrared) at a depth within a thin layer on the water side of the air-sea interface where conductive and diffusive processes dominate. In the main infrared window, the layer is 10 μm.

The sub-skin sea surface temperature $SST_{subskin}$ is representative of the SST at the bottom of the cool skin.

The subsurface temperature SST, traditionally referred to as bulk SST, considers any temperature within the water column below $SST_{subskin}$ where turbulent heat transfer processes dominate, see Section 1.3. It may be significantly influenced by local solar heating and varies on a scale of hours and typically varies with depth. Therefore, SST should be quoted at a specific depth. Bulk SST is measured with temperature sensors on buoys or ships.

The region below $SST_{subskin}$ is dominated by turbulent mixing. The physics involved in this region are introduced in Section 1.3 together with the limitations on representing the processes of turbulence with current numerical methods.

1.3 Turbulence and range of scales

The so called Navier-Stokes equations fully describe the motion of a Newtonian fluid. There are no analytical solutions to these equations but they can be discretised and solved numerically. Under the Boussinesq approximation (see Section 2.5.1), the Navier-Stokes equations are simplified and these have been solved numerically for many years for a range of computational fluid dynamical problems (Burchard, 2002). Numerically solving such equations is known as direct numerical simulation (DNS).

This method is limited because of the range of spatial and temporal scales involved in real world situations. For the ocean, these cover several orders of magnitude, see Figure 1.9.

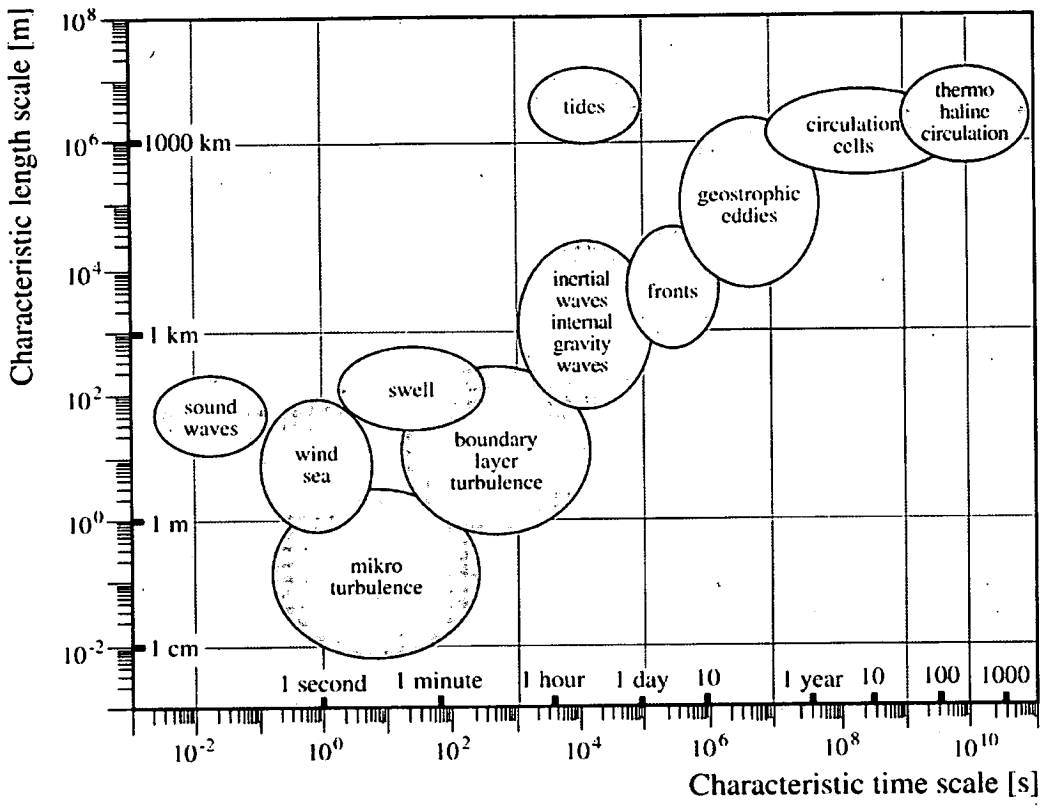

Figure 1.9 Temporal and spatial scales of various typical processes in the ocean, reproduced from Burchard (2002)

A measure of turbulence in the water column is the Reynolds number (Re). A general form of the Reynolds number is,

$$\mathrm{Re} = \frac{UL}{\nu} \tag{1.7}$$

where ν is the kinematic viscosity, U is a typical flow speed and L is a characteristic length scale.

The Reynolds number provides a ratio of inertia to viscosity in a flow. Flows with high Reynolds numbers are often unstable to small disturbances and may

become turbulent. With typical values for the mixed layer of U=0.1 ms^{-1} and L=1m, Re ~ O(10^5). The number of grid points required to fully resolve the smallest eddies is proportional to $Re^{9/4}$ and with a time-step proportional to the grid size the numerical effort goes like Re^3. Only problems with Reynolds numbers up to Re ~ 10^4 can be solved by DNS with present computing power (Burchard, 2002). To solve problems involving turbulent flow with less computational expense than DNS, all or at least part of the turbulence must be parameterised. A method known as large eddy simulation (LES) resolves the large energy containing eddies whilst the smaller scales into which the energy is transferred are parameterised. Less computationally expensive than LES are turbulence closure models. In these models, all of the turbulence is parameterised. Another even more basic model is the bulk mixed layer model where all of the physics of mixing is parameterised.

Therefore, there exists a hierarchy of models to deal with the problem of how to resolve turbulence in the ocean, from DNS to LES to one-dimensional turbulence closure models and bulk, mixed layer models.

1.4 Consequences of diurnal warming and the cool skin for fluxes

For monthly or annual mean air-sea flux determination, the skin to bulk difference of SST is not too problematic. Fairall et al. (1996b) found that, averaged over 70 days of the Coupled Ocean Atmosphere Response Experiment (COARE), the cool skin decreased heat output from the ocean by 11 W m^{-2}, while the warm layer increased it by about 4 W m^{-2}. However, the effect can be 50 W m^{-2} at midday and therefore it cannot be ignored in applications requiring surface flux fields with high spatial and temporal resolution, e.g. OGCM, and regional weather forecasting. The skin sea surface temperature determines latent and sensible heat fluxes and upwelling longwave radiation fluxes, whereas the bulk SST determines potential heat exchange between ocean and atmosphere (Hasse, 1971).

Transfer coefficients in traditional bulk formulae for calculating fluxes (see Section 3.2.5) have been found using bulk SST. Most traditional SST products are in effect, fields of estimated bulk SST (Report of the Joint WCRP/SCOR Working Group on Air-Sea Fluxes, 2000.). Some newer forms of flux formulae use transfer coefficients derived from so called surface renewal theory where the SSST is the appropriate value. SSST may be measured radiometrically from ships or in-situ platforms and by satellite borne radiometers. With satellite based measurement, SSST over the global ocean is made possible, with good temporal and spatial coverage. Therefore, when assimilating sources of SST, it is important to take into account the depth at which the SST is measured or calculated.

1.5 Consequences of diurnal warming and the cool skin for ocean modelling

Diurnal warming also influences the depth of the oceanic mixed layer, OML. Stratified, convectively stable warm layers at the surface suppress mixing so that increased SSTs are associated with shallower mixed layers. Since the diurnal process modulates the depth that the wind-driven transport penetrates the upper ocean, it influences which water makes up the volume transported (Price et al 1986).

Recent research has shown that it is important to include the diurnal cycle of SST in the modelling of processes with intraseasonal timescales (30 to 60 days), such as the Madden-Julian Oscillation (MJO). The MJO significantly affects the atmospheric circulation throughout the global Tropics and subtropics and also the wintertime jet stream and atmospheric circulation features over the North Pacific.

Intraseasonal variability of SST is associated with the MJO, yet coupled models generally under predict the magnitude of this variability, Bernie *et al.*

(2003). However, Bernie *et al.* (2003) show that the rectification of the diurnal cycle of SST onto the daily mean SST accounts for about one third of the magnitude of intraseasonal variability of SST associated with the MJO in the west Pacific warm pool.

1.6 Scope of the thesis

This research is mainly concerned with accurate prediction of sea surface temperature (SST) with respect to the following properties:

Property	Definition
SST with high spatial and time resolution	Sea Surface Temperature at time resolution matching any observed data and at any depth to 10 m.
Diurnal amplitude of SST	The maximum daytime temperature minus the minimum night-time temperature at any given depth.
Thermal stratification	The temperature at less than 1 m depth minus the temperature at depths (5 or 10 m).

Table 1. 2 This research requires the model to skilfully simulate the properties defined in this table.

The principal parameters that affect diurnal amplitudes of SST are: surface solar irradiance, turbulent heat fluxes (i.e. latent and sensible heat), wind stress (i.e. from wind speed) and cloud. These are the parameters upon which this research is focussed. Other parameters that will influence SST are: sea spray, fog and breaking waves.

A one-dimensional turbulence model is used to simulate temperatures in a column of open ocean. The bulk of this thesis describes enhancements made to the model and improvements in the prescription of forcing fluxes from the atmosphere. This research brings together data from diverse sources and combines them with numerical modelling to investigate diurnal warming of SST.

1.7 Layout of the thesis

Chapter 2

In this chapter, models that simulate vertical mixing of water in the ocean are described. The advantages and disadvantages as set out in the literature are discussed and two types of model are compared using open ocean buoy data with respect to the properties given in Table 1.2. The basic principles of how these models simulate mixing and details of their calibration are outlined to give the reader insight to the merits of each model. Model resolution is also defined here, with high resolution near the surface to accurately model the distribution of solar radiation.

Chapter 3

The accurate prescription of fluxes of heat and momentum between ocean and atmosphere and heating from solar radiation is critical to the skilful modelling of diurnal cycling of SSTs. For the model used in this research, these fluxes must be parameterised from available measured meteorological variables. Several parameterisations from the literature are described in Chapter 3 and the physical principles on which they are based are explained. Possible deficiencies in existing solar radiation parameterisations are indicated and solutions to such deficiencies proposed.

The most novel work in this chapter is the incorporation of relatively recent research on optical properties of water into ocean modelling and improving existing solar radiation parameterisations with new coefficients from radiative transfer modelling.

Chapter 4

In this chapter, the parameterisations described in Chapter 3 are grouped into sets of options and the performances of these options are compared within each 'option-set'. The data sets that are used as input to the model and for

comparison of observed SSTs with modelled SST are described. The method of how to determine the best parameterisations for this research is set out. The skill of the model is determined by comparison with observed SSTs using a root mean square statistic over the time period of each model simulation. Estimates are given of how much improvement each modification has made.

In the latter part of this chapter, the best configuration of the new model is compared with the original model and significant improvements are shown. The model is also run with data sets alternative to the 'calibration' part of this work as a validation of the improvements.

Chapter 5

There are many sources of meteorological data with which to force the one dimensional ocean model. Some of the data has high temporal resolution, with intervals of the order of 10 minutes. Such high resolution data doesn't have global spatial coverage but lower resolution data exists that does encompass the global oceans. This chapter explores the possibility of exploiting lower resolution data and quantifies the losses in accuracy associated with low temporal resolutions of forcing data.

Chapter 6

SSTs simulated by the improved model at buoy locations (for available meteorological data) are compared with collocated SSTs retrieved from satellite measurements. This work is further validation of the improved model, specifically at depths shallower than the uppermost buoy temperature sensors.

At the time of this research, very little high resolution meteorology was available synchronous with the Meteosat 8 SST buoy match-ups database. Therefore the viability of using alternative data sources to buoy data is also

investigated. This work is a useful step towards exploring the viability of incorporating SSTs obtained from the Meteosat 8 satellite into ocean modelling of the diurnal cycle of SSTs.

Chapter 7

In this chapter, the novel features of the research are summarised. Further work is also proposed that would merit consideration by researchers interested in the diurnal cycle of SSTs and applications in operational and climate modelling.

Chapter 2 Comparison of mixing models

The three main considerations to modelling the sea surface temperature at a single location are:

(1) Heat source and the vertical distribution of solar radiation.

(2) Interactions between the ocean and the atmosphere.

(3) The vertical mixing of properties such as heat, momentum and salinity.

In this chapter, three models that simulate mixing in an ocean column are investigated for their suitability for predicting diurnal-warming of the sea surface. The focus here is on how the models simulate mixing in the water column (3) rather than on sources and sinks of heat and momentum (1) and (2), which are explored in Chapters 3 and 4.

The classes of one-dimensional mixing model considered here are:

- convective-adjustment
- bulk mixed-layer
- turbulence-closure

Implementations of all three classes of model are available for free download on the World Wide Web. The convective adjustment and turbulence-closure models are options that are coded in the General Ocean Turbulence Model (GOTM). The Price Weller Pinkel (PWP) model is a type of bulk mixed-layer model that was developed by J. Price, R. Weller and R. Pinkel (1984).

The URL for downloading the GOTM code is http://www.gotm.net and the URL for downloading the PWP model code is http://www.whoi.edu/science/PO/people/jprice/website/projects_upperocean.html. These are the models investigated in this chapter.

2.1 Convective-adjustment models

The convective-adjustment class of model simulates the mixing of water whenever a density gradient is unstable. In the convective adjustment module in GOTM, this is done by adjusting the temperature and salinity profiles. It is often employed in general circulation models for its simplicity and computational economy. However, diurnal warming is sensitive to wind-driven mixing which convective-adjustment does not account for. It is useful for global ocean models where resolution is too coarse for differential turbulence closure schemes such as those coded in the turbulence module of GOTM. Computational economy arguments favouring this type of model are now only applicable to climate models used to simulate several hundred or thousands of years of climate (Burchard, 2002).

2.2 Bulk mixed layer models

The Price-Weller-Pinkel (PWP) model is often chosen for its simplicity whilst maintaining an acceptable accuracy for many purposes, (Curry and Webster, 1999). In this model, the bulk Richardson number R_b is employed to determine the tendency for instability in the mixed layer. The bulk Richardson number is a measure of the stabilising effect of stratification relative to the destabilising effect of shear. Mixing occurs in the model whenever this number falls below an empirically derived critical value (Price et al. 1986).

The PWP model is essentially the dynamic instability model (DIM) of Price *et al.* (1978), a conventional, bulk, mixed-layer model. The DIM model was modified by PWP to include mixing in the stratified water below the mixed layer. In this region, shear flow instability is governed by the gradient Richardson number R_g, see equation (2.10). This modification was made to smooth the unrealistic, step-like jump in density at the base of the mixed layer that is a characteristic of bulk mixed layer models, Price *et al.* (1978).

The criteria for vertical mixing in the PWP model are summarised below.

$$\frac{\partial \rho}{\partial z} \geq 0 \tag{2.8}$$

for static stability.

$$R_b = \frac{g \Delta \rho h}{\rho_0 (\Delta V)^2} \geq R_b^{critical} \tag{2.9}$$

for mixed layer stability.

$$R_g = \frac{g\, \partial \rho / \partial z}{\rho_0 (\partial V / \partial z)^2} \geq R_g^{critical} \tag{2.10}$$

for shear flow stability.

Where ρ is water density, z is depth, Ri_b is the bulk Richardson number, $R_b^{critical}$ is the critical value of the bulk Richardson number, ρ_0 is the reference or background water density, h is the mixed layer height, g is acceleration due to gravity and v is water velocity. Price et al. 1986 suggest $R_b^{critical} = 0.65$ and $R_g^{critical} = 0.25$.

R_g is calculated by first differences over the stratified part of the profile (i.e. not in the mixed layer). If the smallest R_g in the profile is found to be less than the critical value of 0.25, then density, temperature, salinity and velocity at the two grid levels that produce the smallest R_g say j and $j+1$, are partially mixed according to

$$\rho_j' = \rho_j - \left(1 - \frac{R_g}{R_g'}\right) \frac{(\rho_j - \rho_{j+1})}{2} \tag{2.11}$$

$$\rho_{j+1}' = \rho_{j+1} + \left(1 - \frac{R_g}{R_g'}\right) \frac{(\rho_j - \rho_{j+1})}{2} \tag{2.12}$$

where primes indicate values after mixing. $R_g' = 0.3$ is a specified constant.

R_g' is set just slightly larger than the critical value to speed convergence and this has no appreciable consequence in the solutions, versus say a value of 0.25. R_g is recalculated from *j-1* to *j+2* and this mixing procedure continues until $R_g \geq 0.25$ throughout the stratified portion of the profile.

However, the DIM model [and therefore the PWP model] is less than fully predictive because some of the model constants are considered adjustable (Price *et al.*, 1978). In the DIM model, 'free' constants (i.e. $R_b^{critical}$) can be adjusted so that simulated mixed-layer depth (or temperature) matches observed mixed layer depth (or temperature) at some particular time (usually at the start or end of the simulated period). The model can thus be made [tuned] to simulate any given event with some success (Price *et al.*, 1978).

One of the goals of this research (see chapter 1) is to improve understanding of the interactions between the ocean and the atmosphere. Fluxes to and from the atmosphere affect mixing which affects SST but SST affects fluxes. By tuning the mixing to fit the event that is to be simulated, it is unclear whether or not the SSTs are correctly modelled only because the 'adjusted' mixing is compensating for poorly prescribed fluxes. This makes it difficult to determine (with sensitivity experiments) the best options for modelling fluxes. This limits how much can be understood about the physics and the parameters that are important in characterising the diurnal cycle.

2.3 Turbulence closure models

In one-dimensional turbulence closure models, the mixing is determined by solving hydrodynamic equations, the equations for turbulent kinetic energy (tke) and turbulent length scale, and evaluating the turbulent fluxes.

The General Ocean Turbulence Model (GOTM) incorporates several 1-D turbulence closure models. GOTM has a wide range of options for exploring the parameterisations governing mixing. There are two turbulent kinetic energy (tke) methods to choose from, the Mellor Yamada (kL equation) method and the kappa-epsilon (k-ε equation) method. There are also ten length scale methods and twelve stability methods, providing many mixing scheme combinations. However, no particular turbulence closure scheme has been found which is superior to all others (Burchard, 2002). The goal here is to find the scheme most suited for modelling diurnal variability of SST that also remains applicable between data sets and seasons.

Turbulence closure models cannot be properly calibrated with field observations (Burchard, 2002). The models have to be validated by theoretical considerations and with laboratory experiments or numerical experiments with higher-order models such as large eddy simulations (LES). The two-equation turbulence closure models coded in GOTM are calibrated in this way. Following the calibration, the models were validated by simulation of field campaigns (Burchard, 2002).

2.4 Comparison of the GOTM turbulence closure and PWP models

The GOTM turbulence closure and PWP models are compared in this Section. It is not possible to determine the quantitative performance of the mixing simulated by each model directly without high resolution measurements of the turbulence field. Instead, mixing is first qualitatively assessed by comparing the simulated vertical temperature distributions.

Only alternative mixing schemes are being compared here, and therefore surface heat fluxes, the distribution of solar radiation and momentum transfer

must be identical in each model. Forcing fluxes are externally calculated from meteorological data using the COARE 3.0 algorithm developed by Fairall *et al.* (2003). This algorithm is described in Section 3.2.6. Distribution of solar radiation is parameterised here by the 2 stream distribution of Paulson and Simpson (1977), which is described in Section 3.1.4.

2.4.1 Comparison of simulation of sea surface temperatures (GOTM vs. PWP).

In Figure 2.1 the modelled time series of SST for two data sets are shown. The blue series are from the k-ε model in GOTM, the red series are from the PWP model and the black series are the observations.

Arabian Sea SSTs

SST is modelled for 9 days at 15N 61E in the Arabian Sea, commencing on 22nd May 1995. In this simulation (Figure 2.1 top), GOTM (k-ε) predicts greater diurnal amplitudes of SST at the top sensor than PWP. The afternoon cooling is also more rapid in the GOTM (k-ε) simulation and more closely matches the observed rate of cooling for most of the days. This was unexpected because in comparison with bulk mixed-layer models, turbulence closure models are sometimes criticised for under-predicting the mixed layer depth and this is mainly attributed to insufficient mixing (Burchard, 2002). In this example the GOTM (k-ε) model better simulates mixing in the afternoon cooling-phase of the diurnal cycle.

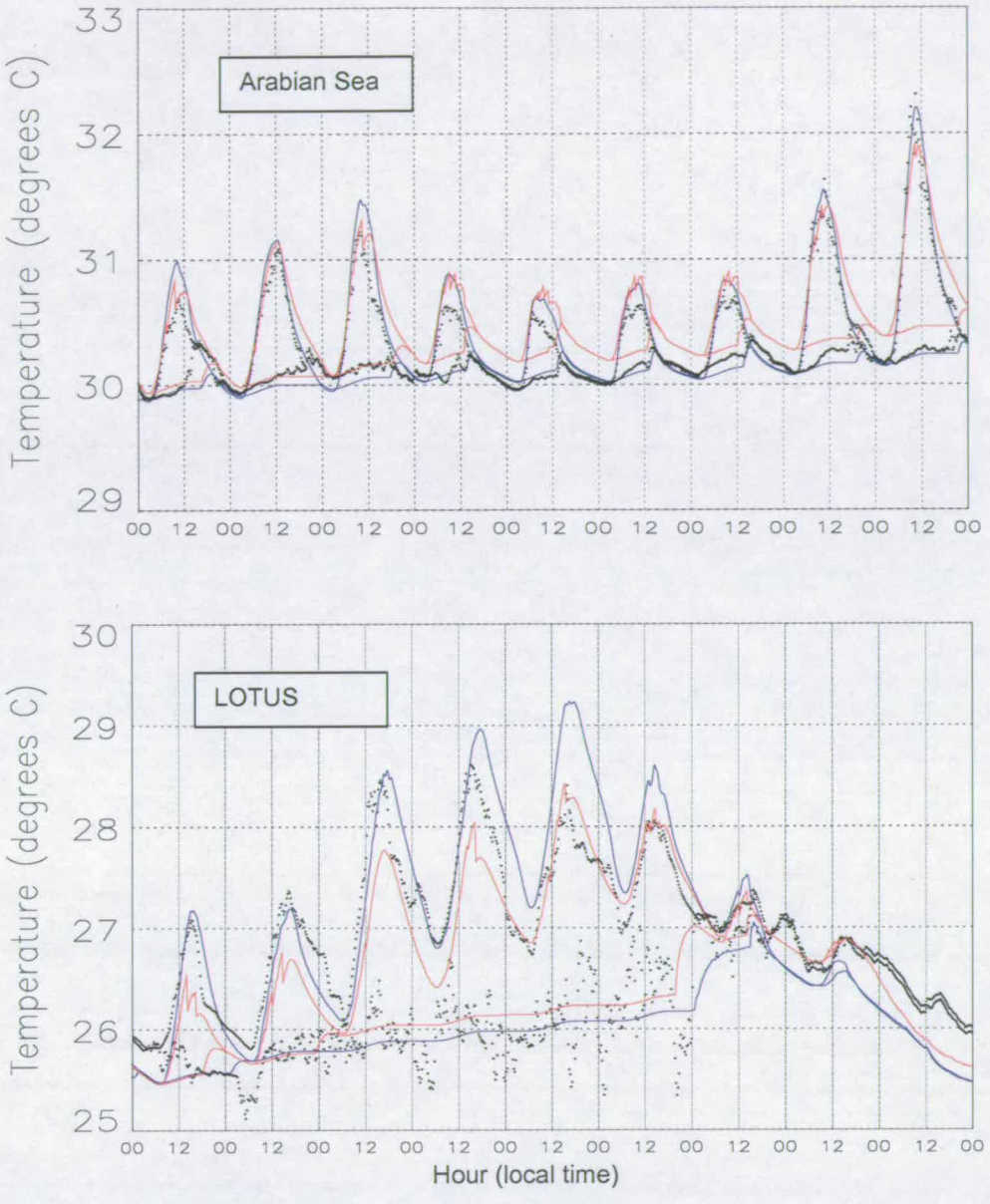

Figure 2.1 Time series of SST for Arabian Sea (top) and LOTUS (bottom) at the top sensor depth and at 5 m. GOTM *k-ε* (blue line), PWP (red line), observed data (black points). The 5 m SST is distinguishable from the top sensor SST by being generally cooler with a smaller diurnal amplitude.

Long Term Upper Ocean Study (LOTUS) SSTs

SST is modelled for 9 days at 34N 70W in the Pacific, commencing on 13th July 1982 (Figure 2.1 bottom). In the LOTUS simulations, the SSTs at the depth of the top sensor are better modelled by GOTM (k-ε) than by PWP for the first four days, in terms of diurnal amplitude and actual SSTs. The rate of afternoon cooling is similar for both models. Although the PWP modelled SSTs are nearer the observed SSTs than the GOTM (k-ε) SSTs on days 5 and 6, the diurnal amplitudes of GOTM (k-ε) SSTs are not much worse than the PWP diurnal amplitudes. The difference in the residuals between GOTM (k-ε) and observations on days 5 and 6 can be partly attributed to the over prediction of the peak SST on day 4.

These are simulations for just two data sets. No tuning has been carried out for either model, the parameters that might be considered tuning parameters having been set to their defaults. Note that the PWP model simulates the Arabian Sea SSTs quite well for the first few days so that the model should not warrant tuning of mixing parameters for this data set.

The GOTM mixing parameters have already been calibrated against laboratory experiments and higher order models, and therefore the parameters that could be adjusted for any given simulation are not adjusted from the default values here. For the LOTUS data then, an alternative tuning of PWP could improve the prediction of SSTs.

2.4.2 Comparison of simulation of temperature profiles to 10 m (GOTM vs. PWP)

Arabian Sea temperature profiles

Modelled temperature profiles from day 10 of the simulation of 15N 61E in the Arabian Sea, are shown in Figure 2.2. The blue profiles are from the k-ε

model in GOTM and the red profiles are from the PWP model. The dashed lines are the observed temperature.

The PWP model profiles always have an isothermal layer at the surface, ½ m deep or more in this example. In contrast, the k-ε model profiles can present some degree of stratification all the way to the surface layer. Neither model can be said to perform better than the other at this stage but the qualitative differences are interesting, nonetheless. The PWP bulk, mixed-layer model simulates complete mixing of all water to the calculated mixed layer depth. The k-ε model also predicts mixed layers at nighttime but the mixed layer can be very shallow during the day with more of the heat in the water column nearer the surface than the PWP model profiles suggest.

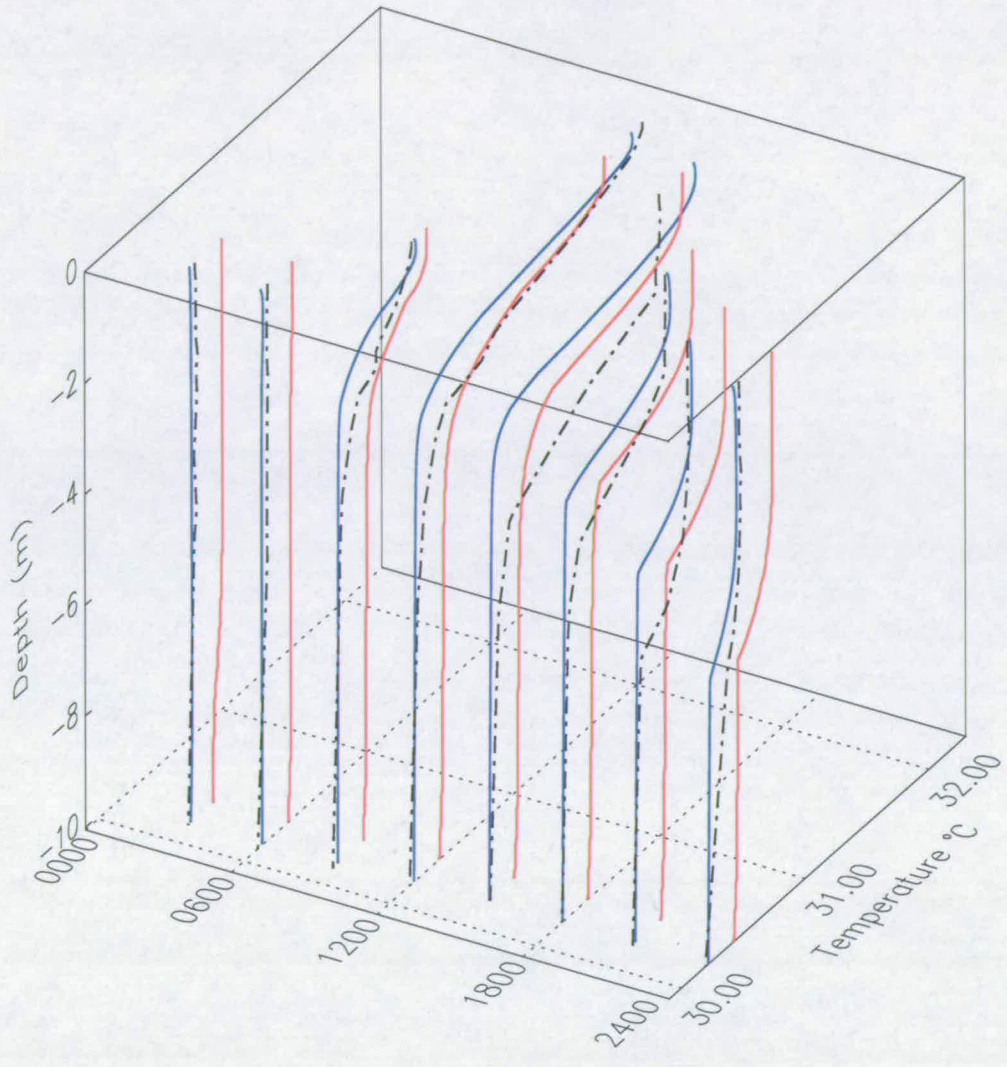

Figure 2.2 GOTM (blue) and PWP (red) modelled temperature profiles from day 10 of Arabian Sea data. The black dashed-lines are the observed temperature profiles. Profiles are at 3 hour intervals.

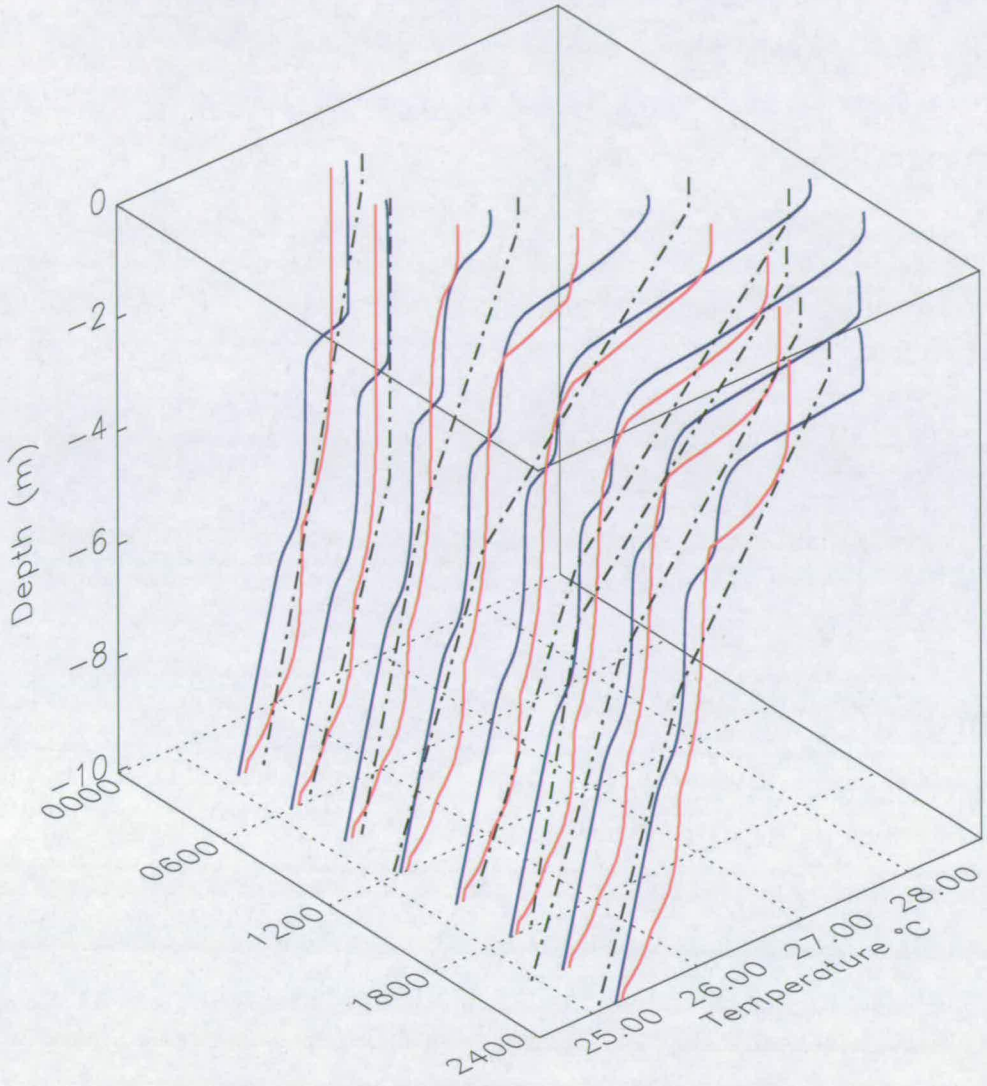

Figure 2.3 GOTM (blue) and PWP (red) modelled temperature profiles from day 3 of LOTUS data. The black dashed-lines are the observed temperature profiles. Profiles are at 3 hour intervals.

LOTUS temperature profiles

The GOTM temperature profiles for day 3 of the LOTUS data set generally exhibit shallower mixed layer depths than the PWP profiles, see Figure 2.3. The modelled SSTs close to the surface are thus warmer with more of the heat distributed near the surface.

The observed temperature profiles (black dashed lines) are linearly interpolated between sensor depths. The interpolation is quite clear in Figure 2.3 with sensors at 0.6 m, 5 m, 10 m and so on. This must be accounted for when comparing modelled profiles with the observations.

2.4.3 Summary of PWP vs. GOTM

Qualitative comparison

Both models simulate temperature profiles that are qualitatively good approximations to the observed profiles. The very near surface SSTs from GOTM are warmer than those from PWP and this is consistent with PWP predicting deeper mixed layers than GOTM. Therefore the interface SST will be generally cooler with more of the available heat mixed over a greater volume of water. This is evident in the SST plots of the two data sets. GOTM also better simulates the cooling-phase of the diurnal cycle in these examples.

Quantitative comparison

If the fluxes predicted by the COARE 3.0 algorithm are accurate then the k-ε model is performing better quantitatively. The metric used here for discerning the quantitative performance between the two models is root mean square of residuals. The definition of this metric is given in Section 4.3. The PWP and GOTM models are compared in Table 2.1. The properties in this table are defined in Section 4.2.

Property	Data set	PWP	GOTM (k-ε)
SST at top sensor depth	Arabian Sea	0.20	0.13
	LOTUS	0.43	0.37
Diurnal amplitude at top sensor depth	Arabian Sea	0.25	0.18
	LOTUS	0.36	0.33
Stratification	Arabian Sea	0.16	0.77
	LOTUS	0.44	0.40

Table 2. 1 Comparison of PWP and GOTM (k-ε) by RMS of residuals (°C) of three properties of the SST

Overall, the GOTM (k-ε) is performing better for these two data sets. The GOTM model will be used for this research on the diurnal cycle. Some details of how the model works are now examined.

2.5 How the GOTM model works

Components of the model

1. Forcing Module: The sources and sinks of heat and momentum
2. Dynamical Module: The basic hydrodynamic equations for velocities and tracers (Reynold's equations)
3. Turbulence Module:
   a. Length scale related equations
      choices here are between the kappa-epsilon (k-ε) and Mellor Yamada (MY) models.
   b. Stability functions
      Twelve options are available from simple constants to functions that are dependent on stratification.

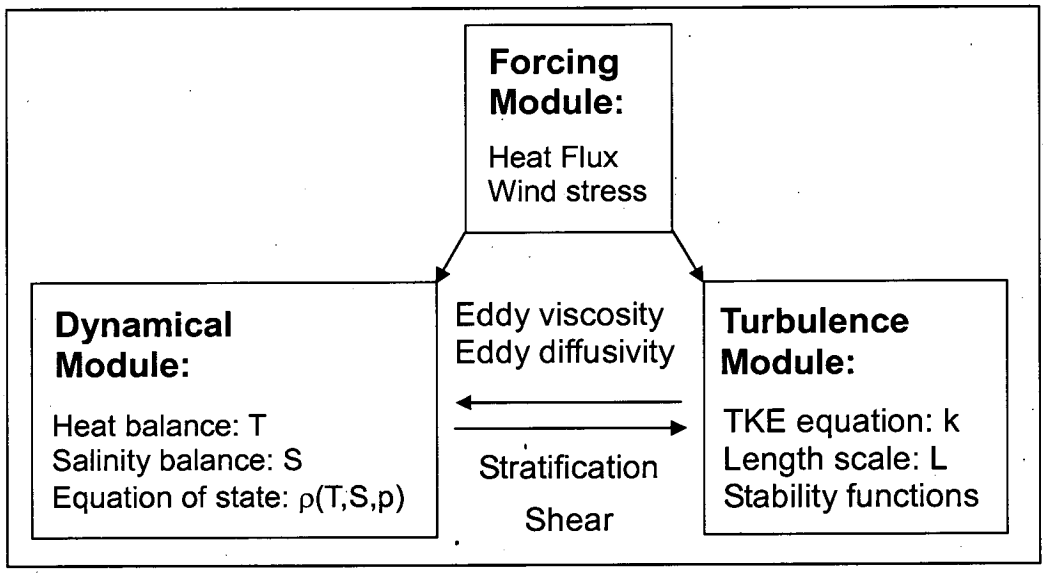

Figure 2.4 The GOTM module structure

It is unclear from the literature which stability functions suit best the purposes of this research and therefore some of the options available in GOTM will be investigated in this Section.

2.5.1 Dynamical Module

The model is 'forced' by fluxes of heat and momentum. This means that at each time-step, values for heat sources and sinks and for wind stress are required as input. From this data, the state of the ocean profile is calculated using the primitive equations (Burchard *et al.*, GOTM manual, 1999).

For homogeneous flow, the hydrodynamic equations can be written as,

$$\frac{\partial u}{\partial t} - \frac{\partial}{\partial z}\left((\nu_t + \nu)\frac{\partial u}{\partial z}\right) - fv = F_u \tag{2.13}$$

$$\frac{\partial v}{\partial t} - \frac{\partial}{\partial z}\left((\nu_t + \nu)\frac{\partial v}{\partial z}\right) - fu = F_v \tag{2.14}$$

where u and v are the horizontal velocity components. ν_t is the eddy viscosity (see Section 2.5.2), ν is the molecular viscosity, z is the vertical Cartesian coordinate, positive upwards, and f is the Coriolis acceleration. F_u and F_v together denote the prescribed barotropic pressure gradient as a function of time.

Under the Boussinesq approximation (vertical density deviations from the mean value are small), the continuity equation for this system is,

$$\frac{\partial u}{\partial x} + \frac{\partial v}{\partial y} = 0 \tag{2.15}$$

The density field ρ is determined by the temperature T and salinity S which are modelled as follows:

$$\frac{\partial T}{\partial t} - \frac{\partial}{\partial z}\left((\nu_t' + \nu')\frac{\partial T}{\partial z}\right) = F_T \tag{2.16}$$

$$\frac{\partial S}{\partial t} - \frac{\partial}{\partial z}\left((\nu_t' + \nu'')\frac{\partial S}{\partial z}\right) = F_S \tag{2.17}$$

where ν_t' is the eddy-diffusivity. ν' and ν'' are the molecular-diffusivities for temperature and salinity and F_T and F_S are the sources and sinks of T and S respectively. Note that the eddy-coefficients, eddy-viscosity (ν_t) and eddy-diffusivity (ν_t'), have the same dimensions as their molecular counterparts but their values are typically orders of magnitude larger than the molecular values (Curry and Webster, 1999).

For the density, the linear equation of state is:

$$\rho = \rho_0 + \beta_T(T - T_0) + \beta_S(S - S_0) \tag{2.18}$$

where ρ_0, T_0 and S_0 are reference values and β_T and β_S constant expansion coefficients. An approximate equation for the buoyancy b is

$$\frac{\partial b}{\partial t} - \frac{\partial}{\partial z}\left(\nu_t'\frac{\partial b}{\partial z}\right) = 0 \tag{2.19}$$

where

$$b = -g\frac{\rho - \rho_0}{\rho_0} \tag{2.20}$$

Together with suitable initial and boundary conditions, equations 2.11 to 2.16 form a closed system for the prognostic quantities, u, v, p, T, S and ρ. Dynamic equations for other properties or dissolved substances (e.g. carbon dioxide) could be added to this system to model those environmental factors (Burchard, 2002).

2.5.2 Eddy-viscosity and eddy-diffusivity

The movement, or flow, of water in the column can be conceptually divided into mean and rapidly fluctuating parts. Whilst the mean part is predictable, the fluctuating part is random. The fluctuations (turbulence) are irregular swirls of motion known as eddies. Eddies are the dominant mode of vertical transport of heat. Molecular conduction is included in the model but is insignificant when compared to turbulence except at extremely low wind speeds and near the boundaries.

The vertical transport of many properties is governed by turbulent fluxes. The fluxes are related to the gradients of the transported properties, x, by means of the eddy-viscosity (for momentum) and the eddy-diffusivity (for tracers such as temperature) (Curry and Webster, 1999), see equation (2.21).

$$\overline{u_z' x'} = -\nu_t' \frac{\partial \bar{x}}{\partial z} \tag{2.21}$$

where, $\overline{u_z' x'}$ is the vertical turbulent flux, ν_t' is the turbulent eddy-diffusivity (subscript t denotes turbulent), x is the property transported and u_z' is a velocity fluctuation. Strictly, the turbulent eddy-diffusivity at each time-step could be different for each scalar quantity but in GOTM, the turbulent diffusivity for salinity is assumed equal to the turbulent diffusivity for heat. The equation is similar in form to the molecular diffusion equation. Vertical transport of the property temperature is equivalent to 'mixing of heat'. To determine this, the eddy diffusivity must be evaluated. To calculate eddy-diffusivity and eddy-viscosity, the turbulent kinetic energy (tke) and the length scale of turbulence must first be determined.

2.5.3 Turbulence Module.

Turbulent kinetic energy and length scale of turbulence.

The turbulent kinetic energy per unit mass (k) can be modelled by equation (2.22)

$$\frac{\partial k}{\partial t}-\frac{\partial}{\partial z}\left(\nu_k'\frac{\partial k}{\partial z}\right)=P+B-\varepsilon \tag{2.22}$$

where ε is the dissipation rate of tke. P is the shear production of tke and B is the buoyancy production of tke. P is a function of the shear frequency M and B is a function of the Brunt-Vaisala frequency N. The eddy-diffusivity for tke (ν_k') is also dependent on the tke and the turbulent length scale. The eddy-diffusivity for tke is calculated as $\nu_k'=\nu_t'$ for the k-ε model and as $\nu_k'=0.283k^{1/2}L$ for the Mellor-Yamada model.

$$\begin{aligned} P&=\nu_t M^2\\ B&=-\nu_t' N^2 \end{aligned} \tag{2.23}$$

where,

$$\begin{aligned} M^2&=\left(\frac{\partial u}{\partial z}\right)^2+\left(\frac{\partial v}{\partial z}\right)^2\\ N^2&=\frac{\partial b}{\partial z} \end{aligned} \tag{2.24}$$

where b is given by (2.20). The turbulent length scale can be parameterised by dimensional arguments to obtain:

$$L=\left(c_\mu^0\right)^3\frac{k^{3/2}}{\varepsilon} \tag{2.25}$$

where c_μ^0 is a constant. The value for this constant given by Rodi (1987) is 0.5562 and this value is used in both the MY and k-ε models in GOTM.

In the k-ε model, the dissipation rate ε is given by:

$$\frac{\partial \varepsilon}{\partial t}-\frac{\partial}{\partial z}\left(\frac{\nu_\varepsilon \partial \varepsilon}{\partial z}\right)=\frac{\varepsilon}{k}\left(c_{\varepsilon 1}P+c_{\varepsilon 3}B-c_{\varepsilon 2}\varepsilon\right) \tag{2.26}$$

where ν_ε is the eddy diffusivity of ε.

In MY,

$$\frac{\partial kL}{\partial t} - \frac{\partial}{\partial z}\left(\frac{\nu_L \partial kL}{\partial z}\right) = L\left(c_{L1}P + c_{L3}B - c_{L2}\varepsilon\right) \tag{2.27}$$

where ν_L is the eddy diffusivity of *kL*.

From k and L, the eddy-viscosity and eddy-diffusivity can be calculated using the Kolmogorov and Prandtl relationship:

$$\begin{aligned} \nu_t &= c_\mu k^{1/2} L \\ \nu_t' &= c_\mu' k^{1/2} L \end{aligned} \tag{2.28}$$

where c_μ and c_μ' are stability functions.

Boundary conditions for the surface and base of the model are

$$L = \kappa z_0 \tag{2.29}$$

for the boundary value of the length scale *L*, where z_0 is the roughness length at the surface or the bed (base of the model) and κ is the Von-Karman constant. For tke, a no-flux condition is imposed:

$$\nu_k \frac{\partial k}{\partial z} = 0 \tag{2.30}$$

2.5.4 Stability functions

Stability functions generally damp turbulent exchange for stable stratification and enhance it for unstable stratification (Burchard *et al.*, 1998). There are twelve parameterisations of the stability functions in GOTM. Burchard *et al.* (1998) suggest that the choice of stability functions has a stronger influence on the performance of the turbulence model than the choice of length scale related equation (i.e. MY or *k*-ε).

Despite their differences, the stability functions depend [for all models] only on two non-dimensional parameters, the shear number (α_M) and the buoyancy number (α_N) (Burchard, 2002).

$$\alpha_M = \frac{k^2}{\varepsilon^2} M^2 \qquad \alpha_N = \frac{k^2}{\varepsilon^2} N^2 \tag{2.31}$$

where,

$$M^2 = \left(\frac{\partial u}{\partial z}\right)^2 + \left(\frac{\partial v}{\partial z}\right)^2$$
$$N^2 = \frac{\partial b}{\partial z} \tag{2.32}$$

The conditions that give rise to diurnal warming are low wind speeds and for significant warming, strong solar radiation. Some insight for the choice of length scale equation and stability function parameterisation suitable for this research might be obtained by comparing combinations of turbulence related options under these conditions. Eight of the stability function parameterisations are explored here with the MY model and the *k*-ε model in turn, giving sixteen combinations. The models are forced with idealised meteorology, simulating conditions that give rise to diurnal warming. The eight stability function parameterisations tested are given in Table 2.2.

Number	Stability function
1	Kantha and Clayson [1994], full version
2	Burchard and Baumert [1995], full version
3	Canuto et al. [2000], version A, full version
4	Canuto et al. [2000], version B, full version
5	Kantha and Clayson [1994], quasi-eq. version
6	Burchard and Baumert [1995], quasi-eq. version
7	Canuto et al. [2000], version A, quasi-eq. version
8	Canuto et al. [2000], version B, quasi-eq. version

Table 2. 2 Stability functions parameterisations by author

Numerical instability caused the model to terminate the simulations with stability functions 3 and 8. The vertical resolution and model time-step could be adjusted to reduce the numerical instabilities but this would slow the model. Since the remaining options completed the simulations, they seem more suitable without incurring a loss in computational speed. Options 3 and 8 then are eliminated on these grounds.

The turbulent diffusivity is dependent on the stability functions. Profiles of this parameter for the remaining stability function options are plotted in Figure 2.5 for the MY model and Figure 2.6 for the k-e model.

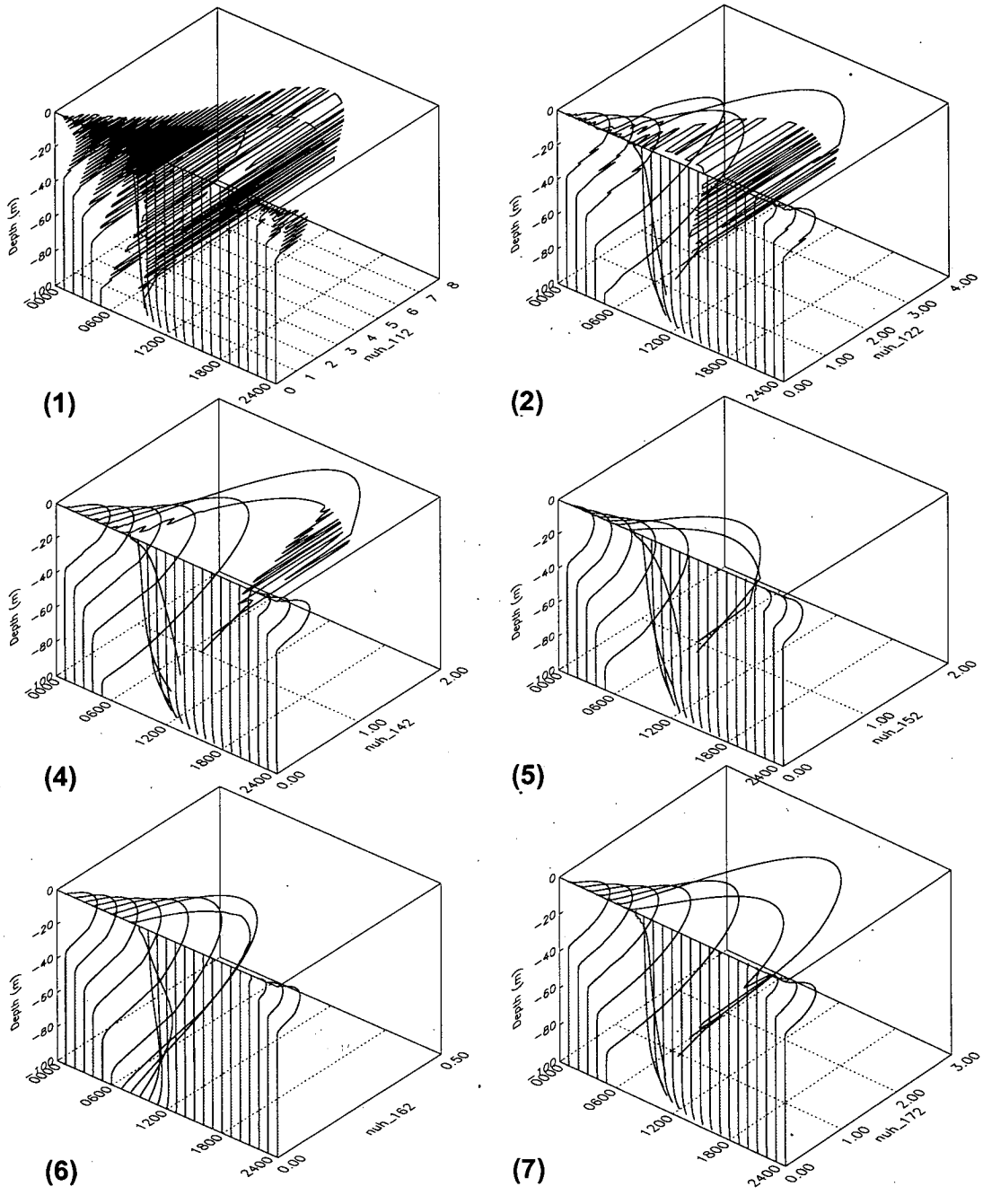

Figure 2.5 Eddy-diffusivity profiles for 6 alternative stability functions with the MY model. The numbers correspond to the stability functions listed in Table 2.1. Units of diffusivity are m^2s^{-1}. The 3 digit code after 'nuh' can be ignored.

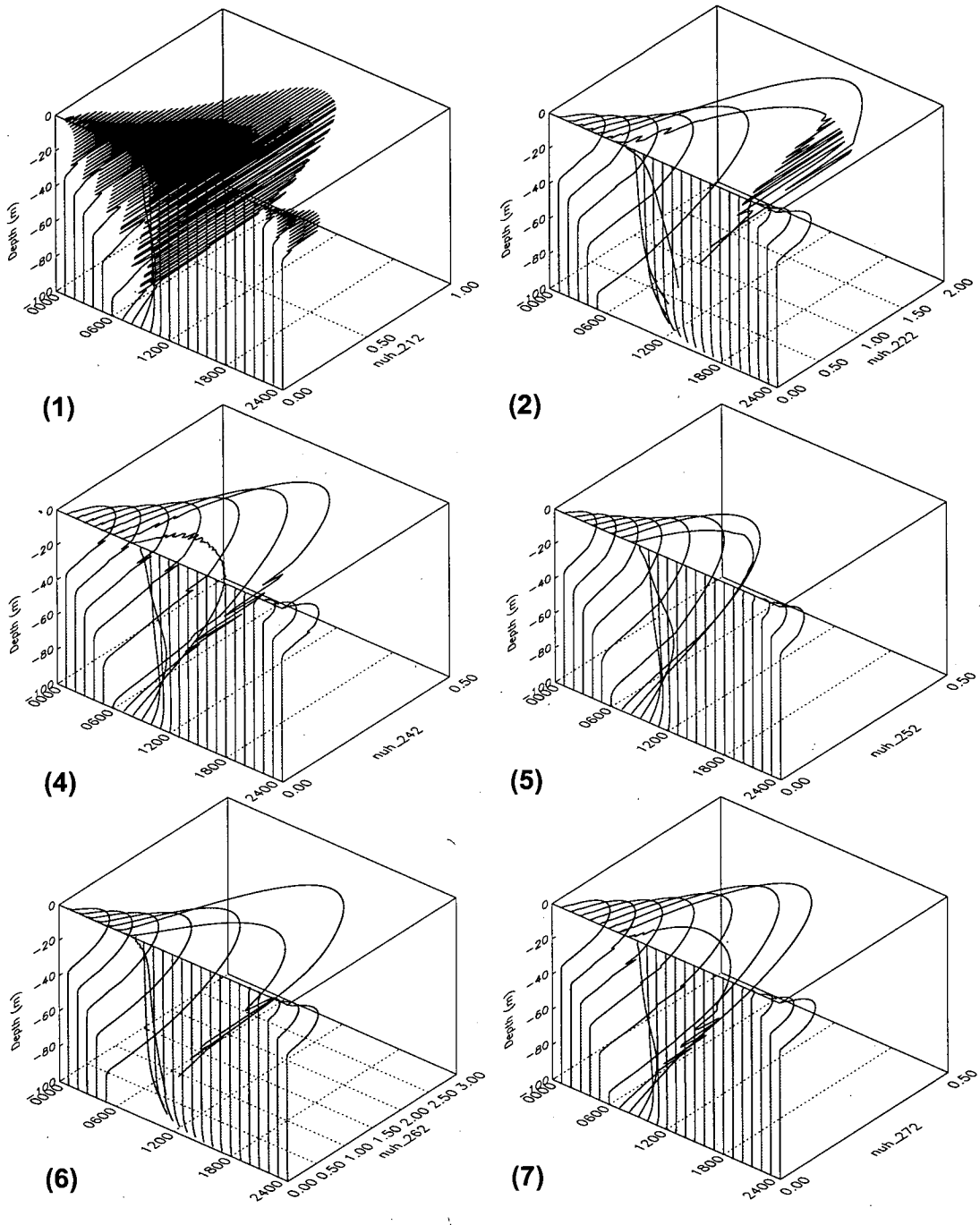

Figure 2.6 Eddy-diffusivity (nuh) profiles for 6 alternative stability functions with the *k*-ε model. The numbers correspond to the stability functions listed in Table 2.1. Units of diffusivity are m^2s^{-1}. The 3 digit code after 'nuh' can be ignored.

The numerical instability caused by the stability functions (1) Kantha and Clayson [1994], full version original functions rule these functions out for this research. These stability functions are the same form as the original functions suggested by Mellor and Yamada. These functions may be poorly defined under some conditions (Deleersnijder and Luyten, 1994), particularly instable stratification (Burchard, 2002). It can be seen from Figures 2.5 (1) and 2.6 (1) that the instabilities occur at night when unstable stratification is present but disappear during the day as the surface layers stratify.

Oscillations in eddy diffusivity can be reduced to some extent by the choice of discretisation in time and space. However, a fine near surface resolution is required which would necessitate very small time steps to mitigate the oscillations of the stability functions. Well-behaved stability functions allow a wider choice of discretisation options without oscillations.

The stability functions that present the least instability are (5) Kantha and Clayson [1994], quasi-equilibrium version and (6) Burchard and Baumert [1995], quasi-equilibrium version. There was no significant difference in the temperature profiles (0.05 K at the surface) between these two options so I chose the Kantha and Clayson [1994], quasi-equilibrium version (5) for the remainder of the research.

2.6 Model resolution

The vertical grid resolution was optimised to be sufficiently detailed to model the absorption of shortwave radiation at the correct depths in the model whilst maintaining an acceptable run time to carry out many investigations of the parameter space (high resolution near the surface, progressively lower resolution at depth), see Figure 2.7. Below 50 cm, the model grid layer thickness was set to 1 metre with a total model depth of 100 metres.

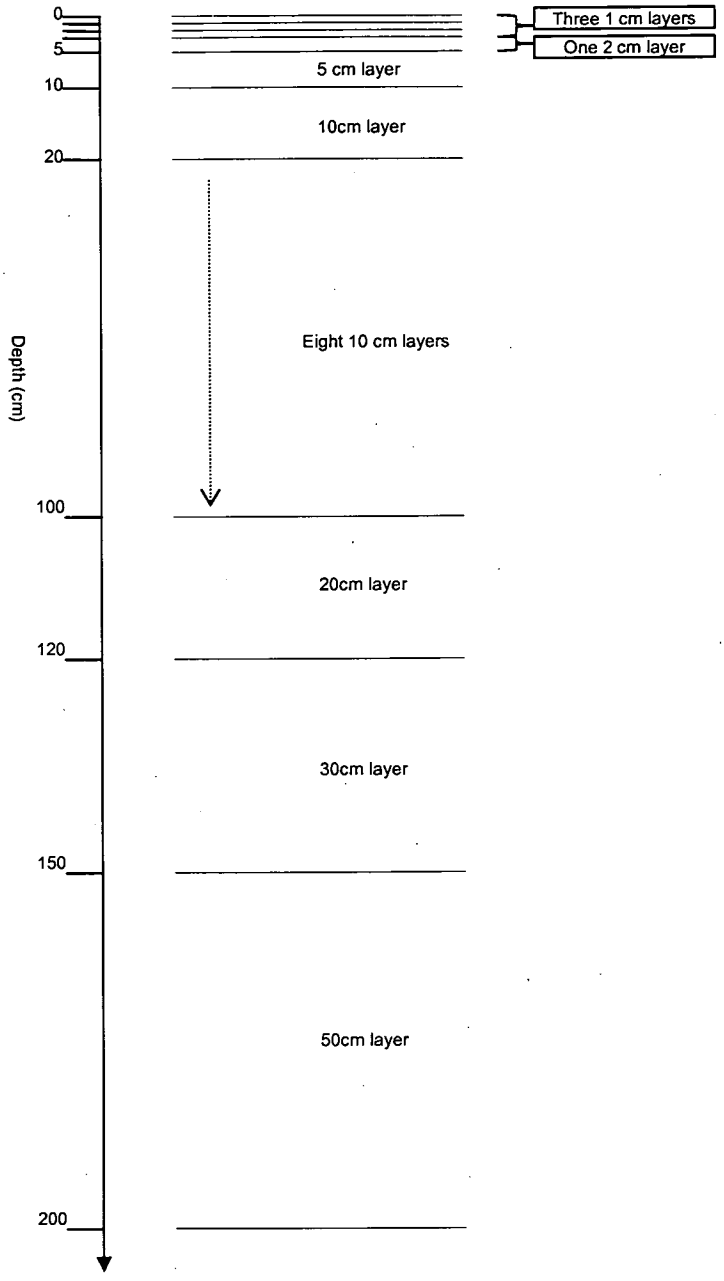

Figure 2.7 Model resolution

The description of the model has been fairly general thus far. The specifics of the MY and k-ε models are described in the next chapter where they are compared as one part of a larger sensitivity study.

2.7 Summary

A one dimensional turbulence closure model was compared with a bulk, mixed-layer model. The 1-d turbulence closure model was found to be more suitable for this research with better 'portability' between locations and times without re-tuning. The details of the 1-d turbulence closure model were introduced. Eight stability functions were investigated and the Kantha and Clayson [1994], quasi-equilibrium found to be suitable. A high resolution vertical model grid was also defined.

Chapter 3 Fluxes background

Introduction

The purpose of the work presented in the next two chapters is to ascertain the best setup for GOTM to predict diurnal warming. Specifically, I seek to minimise the residuals of sea surface temperatures (SSTs) (the differences between simulated and observed SSTs) at 1 m and at one or more depths less than 1 m, at hourly time intervals. A residual of SST is the magnitude of modelled SST minus observed SST at the same depth. I also endeavour to optimise the prediction of diurnal amplitude of SST (maximum day SST minus minimum previous night SST). Accurately modelled skin temperatures would also be required to compare the model with satellite derived SSTs but this is a subject for later chapters.

Many options can be set within GOTM that will have varying degrees of influence on the output surface temperatures. There are also several ways to specify forcing by physical processes that significantly affect predicted temperatures. Modelled temperatures then are expected to depend on flux forcing, turbulence closure equations, and whether modelled or observed SSTs are used in the equations for calculating flux from meteorology.

In this chapter and chapter 4, I examine in detail five sets of options (hereafter referred to as 'option-sets') that are expected to have a significant influence on the surface temperatures output from GOTM. Quantitatively, the sensitivity of modelled SST to the choice of option within an option set will be at least one tenth of a degree. Some option-sets can interact and therefore affect surface temperatures in a way that is not necessarily intuitive or predictable. With several options for each option-set, there is a large matrix of permutations that must be examined to isolate the most skilful combination for predicting diurnal amplitude and surface stratification. I define this matrix and reasons why each option within an option-set was selected for

experimentation. I outline an experiment to test all the permutations of all 5 option-sets. In chapter 4, I present 4 data sets for the experiment, reasons for choosing the data locations and limitations concerning accuracy with measuring the data. The statistics of model skill corresponding to permutations of options will be presented in chapter four.

Information on the instruments used to produce the data sets was obtained from the Woods Hole Oceanographic Institute web site, http://uop.whoi.edu/uopdata/.

The five option-sets that are expected to significantly affect diurnal amplitudes and surface stratification are given in Table 3.1

1) Turbulence mixing scheme: How to distribute heat in a column of water.
2) Short-wave radiation: The dominant source of ocean heating.
3) Downwelling long-wave radiation: parameterisations or measurements.
4) Turbulent flux forcing: Momentum transfer, Latent heat and Sensible heat. [1]
5) Ocean-leaving flux forcing: Use measured or modelled temperatures.[2]

Table 3.1 Five option-sets that significantly affect diurnal amplitudes and stratification

3.1 Short-wave radiation – the Solar flux

Radiation from the sun is comprised of a spectrum of wavelengths. This radiation is attenuated somewhat by the atmosphere with some wavelengths attenuated more strongly than others. Water and carbon dioxide are the molecules of the atmosphere that cause most of the attenuation of solar wavelengths.

[1] Momentum transfer is from atmosphere to ocean via the wind. Latent and sensible heat transfer are usually in the direction from ocean to atmosphere, especially in the open ocean.
[2] Ocean leaving flux includes latent, sensible and longwave (radiative) fluxes that all depend on SST at the interface. The option is simply whether to use modelled or observed SST in the parameterisation of these fluxes. The observed SST is usually at some depth whereas interface SST can be readily obtained from the model with a sufficiently fine vertical grid.

Total solar radiation reaching the ocean surface is known as surface solar irradiance (SSI). All of the data sets used in the experiments include measured SSI from an Eppley pyranometer (or Eppley PSP). The Eppley PSP is an instrument for the measurement of spectrally integrated radiation in the range 285 and 2800 nm. During daylight hours, radiation from all angles impinges on a dome filter that transmits radiation from this spectrum of wavelengths to a thermopile and the resulting voltage is converted to SSI (W m^{-2}). The temporal resolution of the data loggers connected to the PSP (for the data sets in chapters 3 and 4) is 2 minutes. The accuracy of the Eppley PSP is nominally +/- 3 %.

In this Section (3.1), there are two main aspects to consider in modelling the shortwave radiation in the ocean model.

1) The division of solar radiation incident at the ocean surface into a number of discrete wavelength bands.
2) The wavelength dependent attenuation lengths of the entrant solar radiation within the water column.

Water attenuates the red and infrared part of the solar spectrum more strongly than the blue and green parts. It is necessary to estimate the spectral structure of the SSI to some degree of detail. Specifically, it must be determined what fraction of the SSI is associated with each part of the solar spectrum. The spectral structure of SSI can vary with latitude and atmospheric composition. A radiative transfer model of the spectrum of attenuation in the atmosphere can be used to model the spectral structure.

3.1.1 Radiative transfer in the atmosphere

The radiometric quantities that are required for a more complete description of SSI are as follows (mostly following the symbols from Andrews (2000)).

The spectral radiance $L_\lambda(\mathbf{r},\mathbf{s})$ is the power per unit area, per unit solid angle, per unit wavelength interval in the neighbourhood of the wavelength λ, at a point **r**, in the direction of the unit vector **s**. It's units are (e.g.) W m^{-2} sr^{-1} nm^{-1}.

The spectral irradiance $I_\lambda(\mathbf{r},\mathbf{n})$ can be defined as the power per unit area, per unit wavelength interval in the neighbourhood of the wavelength λ, at a point **r** through a surface of normal **n**. Its units are (e.g.) W m^{-2} nm^{-1} but it may also be expressed per unit frequency interval with units W m^{-2} Hz^{-1}. It is obtained from the spectral radiance by integration over a hemisphere on one side of the surface:

$$I_\lambda(\mathbf{r},\mathbf{n}) = \int_{2\pi} L_\lambda(\mathbf{r},\mathbf{s})\mathbf{n}\cdot\mathbf{s}\,d\Omega(\mathbf{s}) \tag{3.1}$$

where $d\Omega(\mathbf{s})$ is the element of solid angle in the direction **s**, see Figure 3.1.

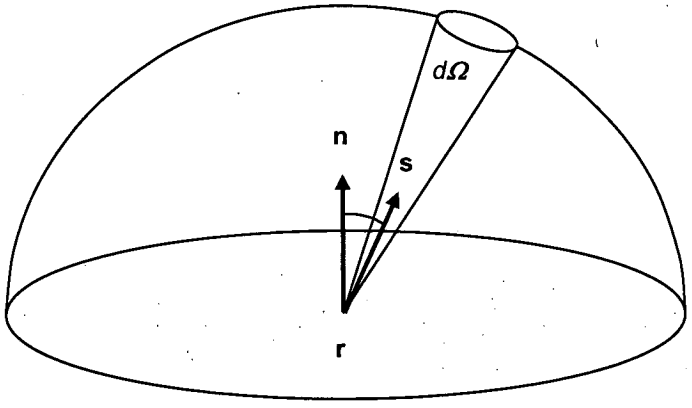

Figure 3.1 Integration of the spectral radiance over a hemisphere to obtain the spectral irradiance, following Andrews (2000).

The irradiance (or flux density) $I(\mathbf{r},\mathbf{n})$ is the power per unit area at a point **r** through a surface of normal **n**, ie the integral of I_λ over all wavelengths λ:

$$I(\mathbf{r},\mathbf{n}) = \int_0^\infty I_\lambda(\mathbf{r},\mathbf{n})\,d\lambda \tag{3.2}$$

with units W m^{-2}.

Solar radiation incident at the top of the Earth's atmosphere (TOA) can be approximated by a black body curve, see Figure 3.2. The spectrum of radiation is scattered and attenuated by the atmosphere, to varying degrees depending on the wavelength, and the resulting surface spectral irradiance curve is also shown. The TOA and surface spectral irradiance curves in Figure 3.2 were derived using the MODTRAN radiative transfer model for a typical tropical atmosphere.

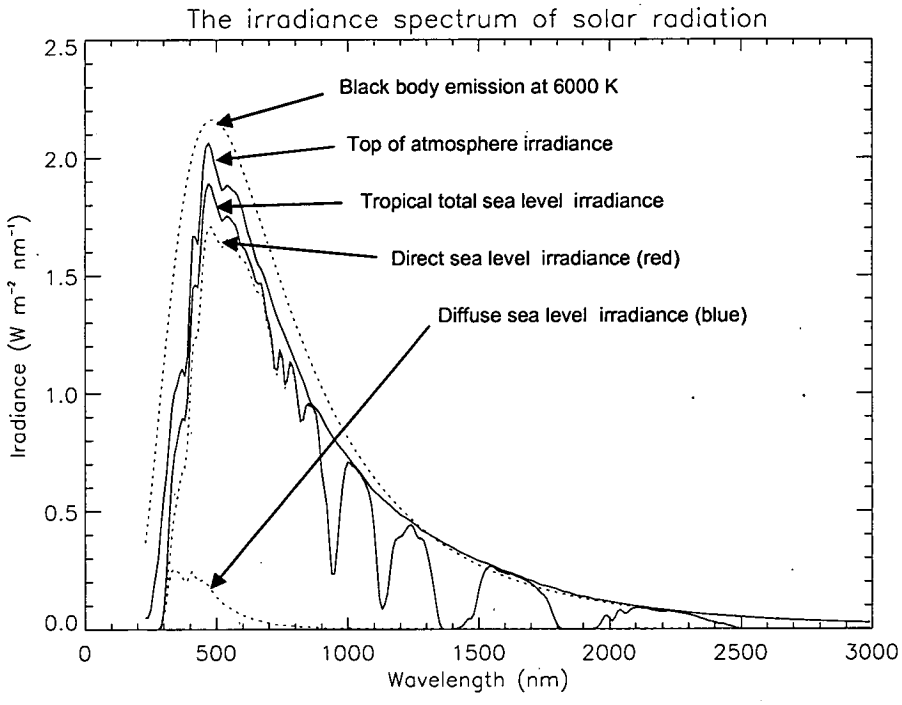

Figure 3.2 The irradiance spectrum of solar radiation at the TOA and at sea level compared to a black-body curve with data from the MODTRAN model of a clear-sky tropical atmosphere, following Andrews (2000).

3.1.2 Dividing the spectrum into a number of discrete bands

The irradiance spectrum shown in Figure 3.2 can be divided into any number of discrete bands to model the wavelength-dependent power of the SSI. More bands provide more detail but at the expense of computational speed when

introduced into the ocean model. The SSI, $I_j(0)$, for each band, j, is obtained by integrating the spectral irradiance curve between the wavelength bounds of the band:

$$I_j(0) = \int_{\lambda - w_j/2}^{\lambda + w_j/2} I_\lambda(0) d\lambda \tag{3.3}$$

where w is the width of the band and $I_\lambda(0)$ is the SSI at wavelength λ. In this way, the fractions of SSI in each wavelength band can be derived.

3.1.3 The attenuation of the entrant solar radiation within the water column

In the absence of suspended matter, the ocean is optically homogeneous. A beam of radiation of wavelength λ passing through a distance δs in water is reduced in intensity by an amount δI_λ which is proportional to the intensity I_λ and to the distance δs travelled through the water (Defant, 1961). Therefore,

$$\delta I_\lambda = -\kappa_\lambda I_\lambda \delta s \tag{3.4}$$

where κ_λ, is the absorption coefficient (m^{-1}). κ_λ can be replaced with the attenuation length $\zeta_\lambda = 1/\kappa_\lambda$, since it is a more intuitive quantity with units of metres. Equation (3.4) can be integrated:

$$\int_{I_\lambda(0)}^{I_\lambda(s)} \frac{dI_\lambda(s)}{I_\lambda(s)} = \int_{s=0}^{s} -\frac{1}{\zeta_\lambda} ds \tag{3.5}$$

to obtain the irradiance per unit wavelength:

$$I_\lambda(s) = I_\lambda(0) \exp(-s/\zeta_\lambda) \tag{3.6}$$

with the intensity of the radiation equal to $I_\lambda(0)$ when s=0, i.e. at the water surface. This equation is the basis for all of the solar parameterisation options tested.

Some authors attempted to model the solar radiation distribution in the ocean by assuming an average attenuation length for the whole solar spectrum, e.g. Denman and Miyake (1973), Haney and Davies (1976). This was shown to be a poor approximation for the top 10 m of the ocean by Paulson and Simpson (1977). Therefore, approaches involving 2 or more wavelength bands are examined in this option-set.

3.1.4 2 bands

Paulson and Simpson (1977) used a bi-modal exponential parameterisation (a 2 band model) to represent attenuation of SSI in the ocean:

$$I = I_0\left(A\exp(-z/\zeta_1)+(1-A)\exp(-z/\zeta_2)\right) \tag{3.7}$$

Radiation is assumed vertical in this model and therefore z is used to specify distance. The first term of equation (3.7) models the rapid absorption of red wavelengths and the less strongly attenuated blue and green wavelengths are incorporated in the second term. The coefficient A and the attenuation lengths ζ are empirically derived from observations of I/I_0. Jerlov (1968) classified 6 water types of increasing turbidity, with clear water, type 1, most representative of the open ocean (Simpson and Dickey 1981). For type 1 water, A=0.58 and ζ_1=0.35 m, ζ_2=23 m.

The bi-modal equation (3.7) for the radiation distribution from Paulson and Simpson (1977) is in the current public domain version of GOTM. The Jerlov type I form of this distribution is the first option tested in the solar radiation distribution option-set.

3.1.5 9 bands

As computational speed increased, researchers were able to increase the number of bands and sum the contributions from each band within each layer of an ocean model e.g. Paulson and Simpson (1981), Morel and Prieur (1977).

For radiation incident normal to the ocean surface then, the remaining radiation intensity summed over n bands at a depth z is

$$I(z) = I_0 \sum_{j=1}^{n} F_j e^{z/\zeta_j} \tag{3.8}$$

where the mean attenuation length of band j is ζ_j and each F_j is the fraction of SSI in band j:

$$F_j = \frac{\int_{\lambda - w_j/2}^{\lambda + w_j/2} I_\lambda(0) d\lambda}{\int_0^\infty I_\lambda(0) d\lambda}$$

where $I_\lambda(0)$ is the irradiance at the sea surface, cf. equation (3.3).

Paulson and Simpson (1981) suggested a 9 stream model, n=9, using fractions F_j from Schmidt (1908), reproduced by Defant (1961). The attenuation lengths ζ_j are from various authors, dating from 1901 to 1933, compiled by Defant (1961).

3.1.6 278 bands

To extend the discretisation of SSI to more than 9 bands, attenuation lengths other than those of the Paulson and Simpson (1981) 9 band model must be found. The wavelength dependency of attenuation length in clear water has been investigated by several authors: Hale and Querry (1973), Buiteveld *et al.* (1994), Irvine and Pollack (1968), Kopelevich (1976), Morel and Prieur (1977), Pope and Fry (1997), Querry (1978), Quickenden and Irvine (1980), Segelstein (1981), Smith and Baker (1981), Sogandares and Fry (1997), Paulson and Simpson (1977), see Figure 3.3 to 3.7. The data for these figures was obtained from Scott Prahl's web site, Oregon Medical Laser Centre: http://omlc.ogi.edu/staff/prahl.html. There is remarkable agreement between

the authors for wavelengths greater than 500 nm. Large disparities are only found between 200 and 500 nm (see Figure 3.4). The uncertainty inherent in this wavelength region is less important for studies of strong diurnal warming in the open ocean, since the attenuation lengths are of the deeply penetrating wavelengths of the spectrum.

To capture most of the details of the SSI spectrum in both SSI fractions and attenuation lengths, a 10 nm band width (278 band) model was defined. SSI fractions were calculated for each data set location with the radiative transfer model MODTRAN. The attenuation lengths (see Figure 3.3 to 3.7) were interpolated from the data of Segelstein (1981).

This level of detail might be more than is required and an experiment to determine an optimum number of bands could be envisaged. Variable band widths could be defined with narrower bands in regions of the spectrum with fine scale variations of SSI fraction and attenuation length. This could be a topic for later research.

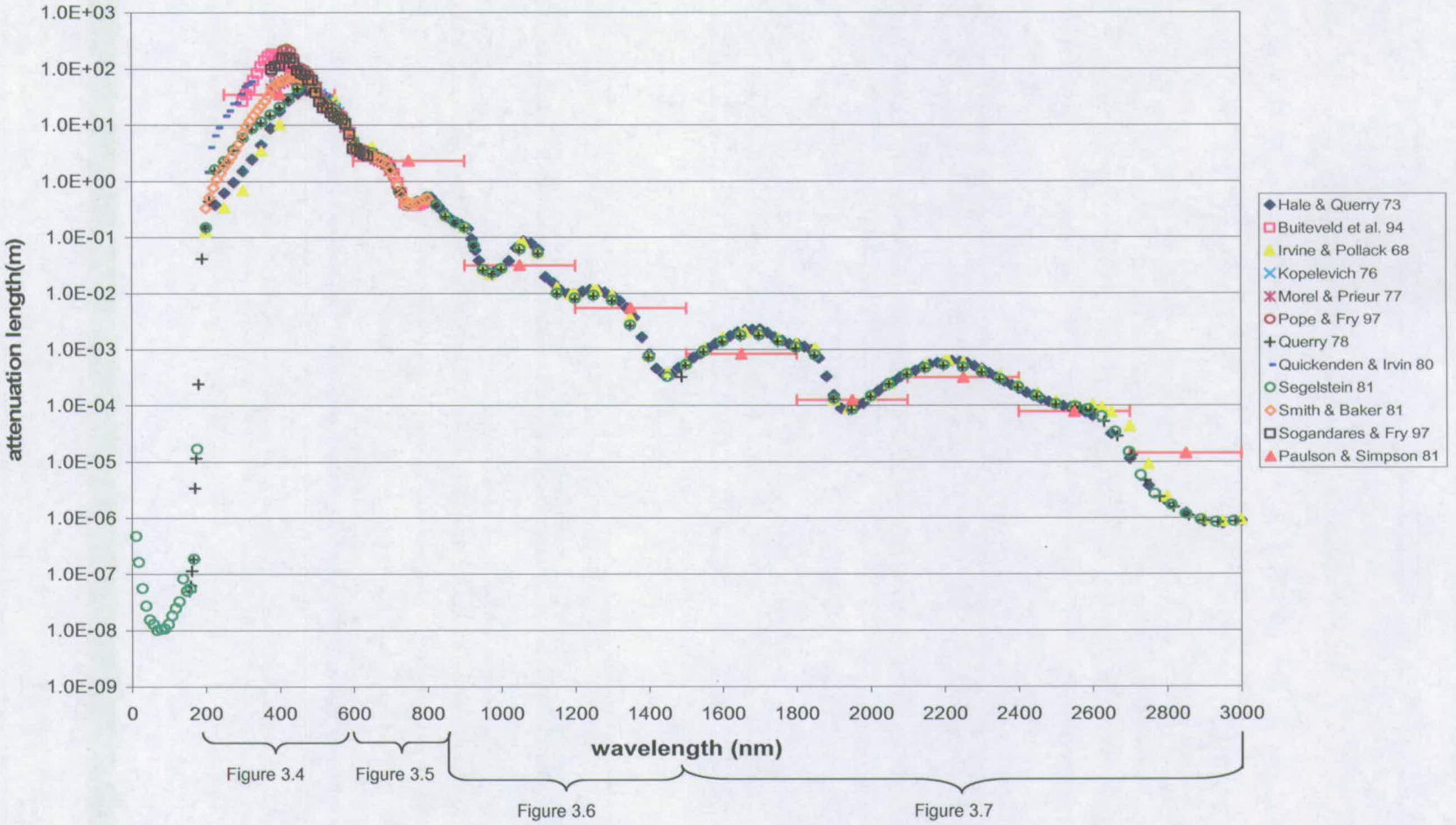

Figure 3.3 Attenuation lengths for full solar spectrum

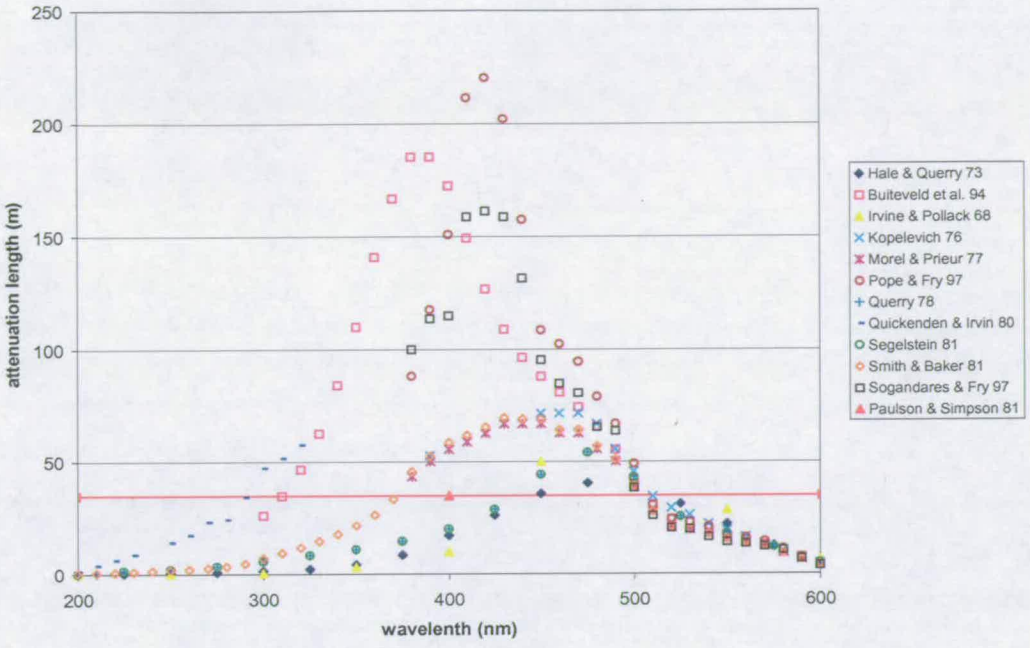

Figure 3.4 Attenuation lengths 200 nm to 600 nm

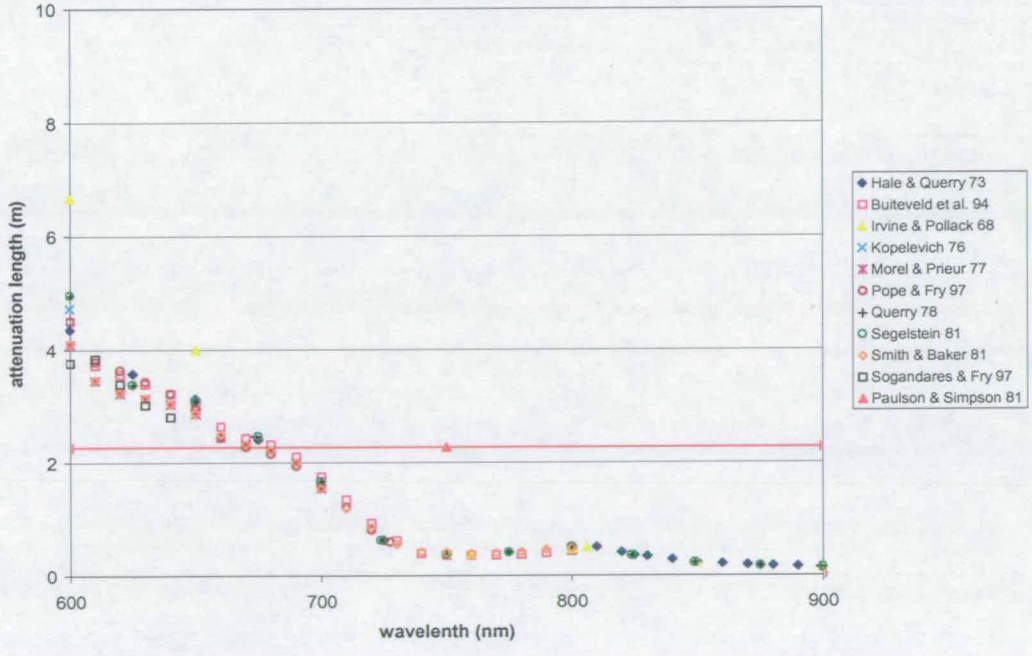

Figure 3.5 Attenuation lengths for wavelengths 600 nm to 900 nm (NB change in y axis scale)

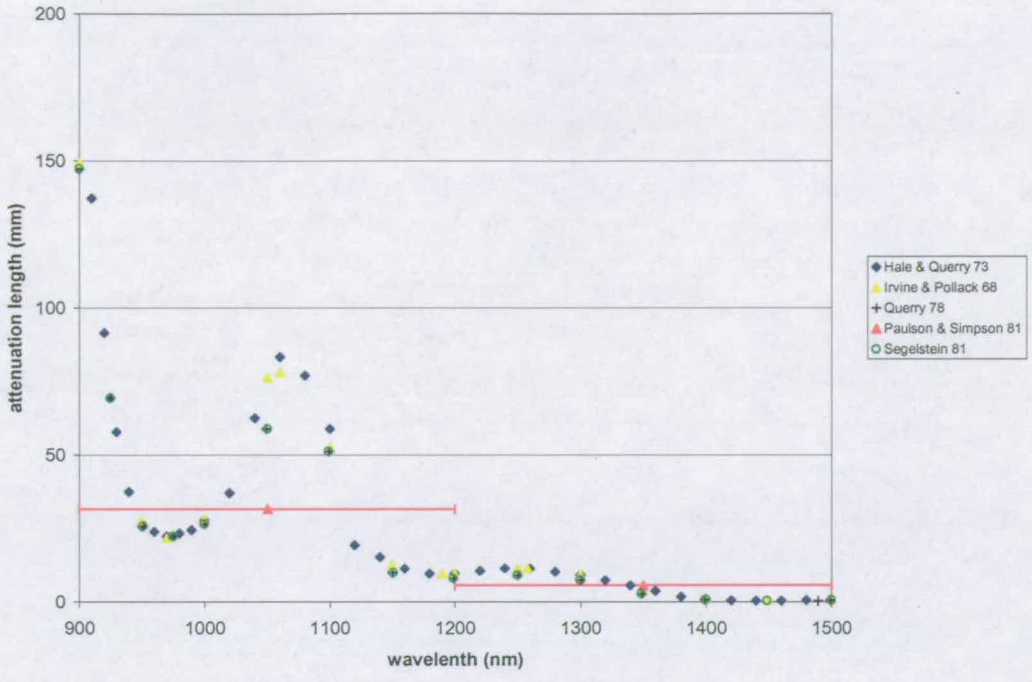

Figure 3.6 (Top) Attenuation lengths for wavelengths 900 nm to 1500 nm (NB change in y axis scale)

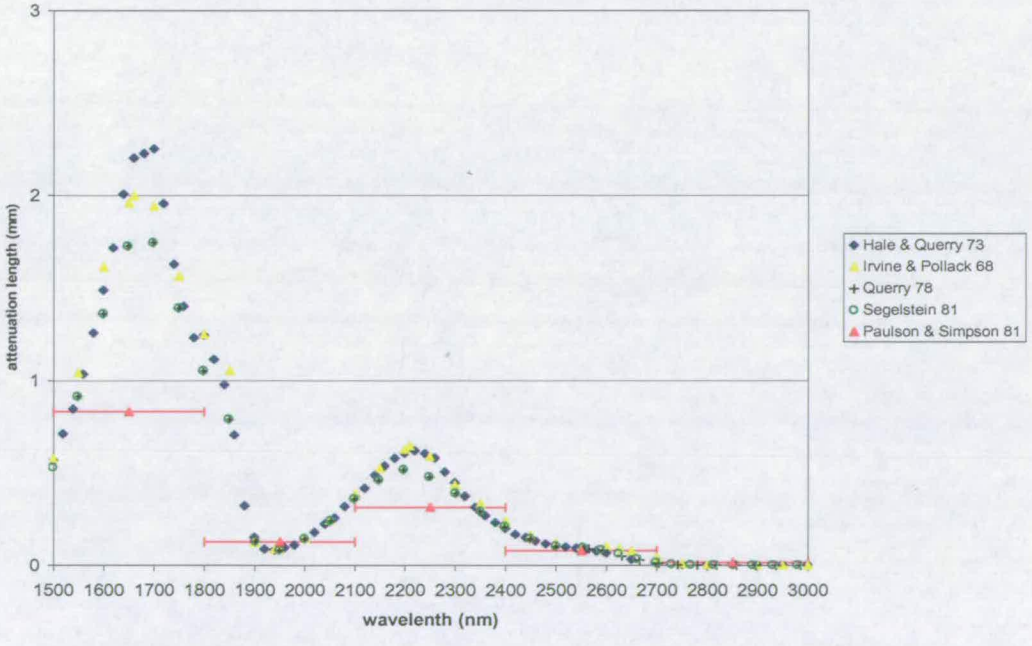

Figure 3.7 Attenuation lengths for wavelengths 1500 nm to 3000 nm (NB change in y axis scale)

3.1.7 Proportions of SSI and attenuation lengths comparisons

The proportions of SSI together with the mean attenuation lengths for each band are shown in Figure 3.8 for discretisations of 2 bands (Paulson and Simpson, 1977), 9 bands (Paulson and Simpson, 1981) and 278 bands (Section 3.1.6).

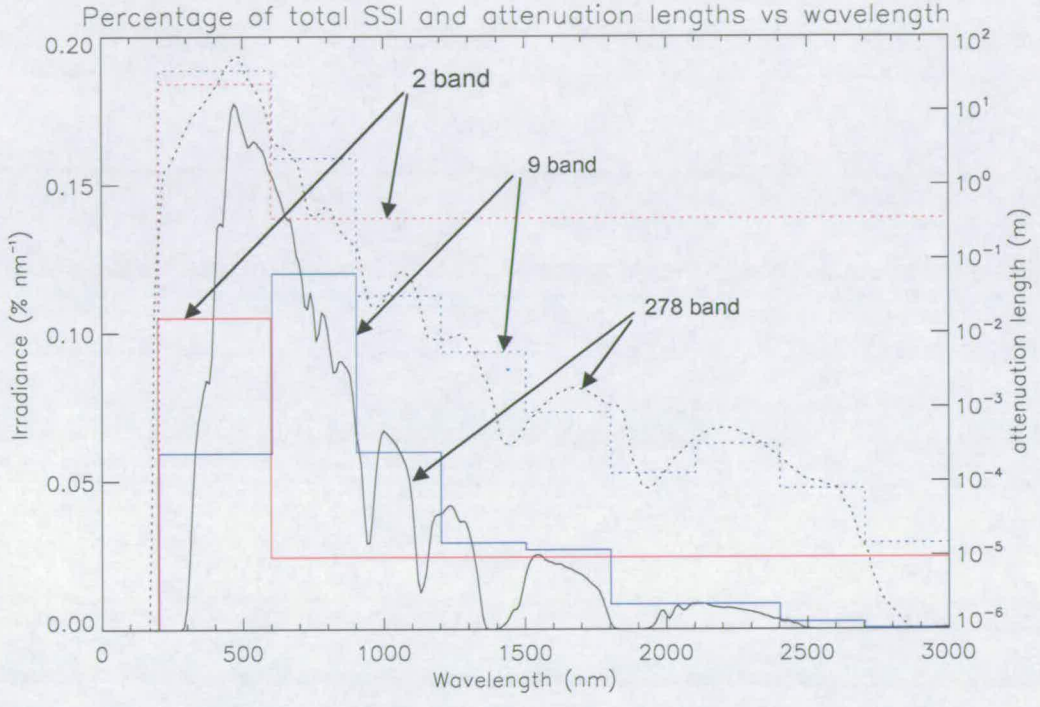

Figure 3.8 Percentage of total SSI and attenuation lengths for discretisations of 2, 9 and 278 bands. Solid lines represent SSI and the dashed lines are attenuation lengths.

Large dips in the SSI fraction curve occur at wavelengths strongly absorbed by water vapour in the atmosphere. It is interesting to note that the dips in the 278 band attenuation length curve correlate well to the dips in SSI fraction, these wavelengths also being strongly attenuated by sea water. Indeed, researchers using spectroscopy to study absorption of solar radiation by water vapour in the atmosphere shine light over a range of wavelengths through columns of liquid water to simulate the kilometres of water vapour traversed

by solar radiation before it reaches the Earth's surface, Physics Web May 2003 http://physicsweb.org/articles/world/16/5/7/2.

It is not just the resolution of the SSI fractions that differ between the models shown in Figure 3.8. When the fractions from the higher resolution models are integrated up to the lower resolution models, the integrated fractions also differ significantly. A clear example is the 1500 to 1800 nm band of the 9 stream model. This fraction of the Paulson and Simpson (1981) model is clearly higher than the fraction that results from integrating the SSI fractions of the 278 band model over this band width.

3.1.8 Model grid and SSI attenuation

When comparing the three models in Figure 3.8, it is informative to consider the model grid to which they will be applied, see Figure 3.9.

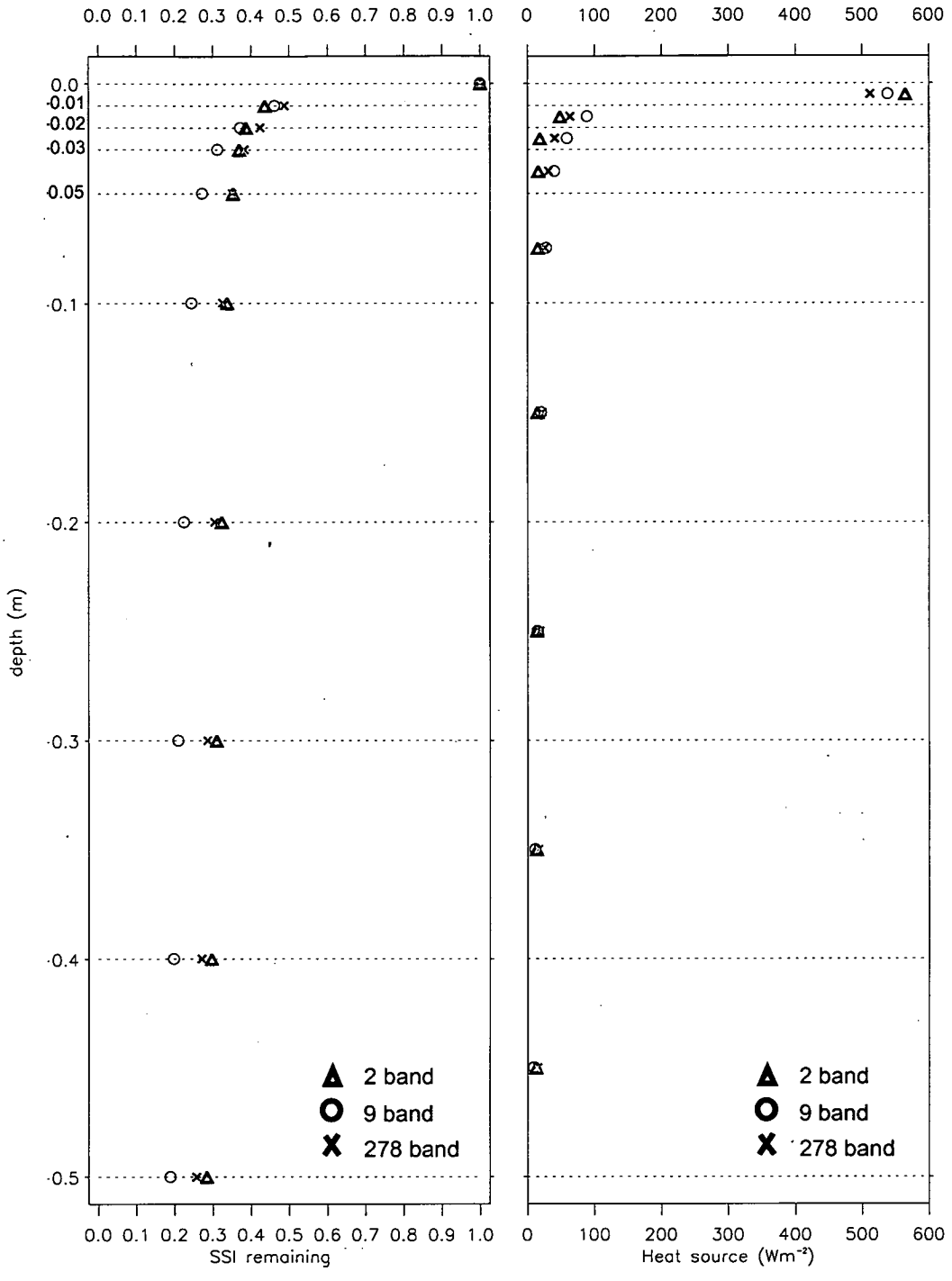

Figure 3.9 Solar heating shown to a depth of 0.5 metres. (Left) Fraction of SSI remaining at each level. (Right) Solar heating in each layer for a vertical SSI of 1000 W m^{-2}.

The horizontal dashed lines in Figure 3.9 represent the model levels (layer interfaces). At the surface, all the multi-band models are equivalent with no attenuation having occurred (SSI remaining = 1.0). As the solar radiation is attenuated with depth, the fraction of SSI remaining at each level diminishes. The figure on the left shows that at 10 mm depth, solar irradiance is most diminished in the 2 band model and least diminished in the 278 band model with the 9 band model in between. At 20 mm however, the 9 band model is the most attenuated and the 278 band model least attenuated. From 10 cm to the base of the model, the 9 band model remains most attenuated, and the 2 band model least attenuated. The figure on the right illustrates the simulated amount of heat delivered to each layer as the radiation is absorbed in the column. The 2 band model delivers more heat to the top layer than both the 9 band model and the 278 band model. However, the 9 band model delivers the most heat to the next deepest four layers and the 2 stream model the least heat to those layers.

Depth (m)	Mid layer depth (m)	Integrated heat (W m^{-2})		
		2 band	9 band	278 band
0.01	0.005	565	538	512
0.02	0.015	613	627	576
0.03	0.025	631	687	617
0.05	0.04	647	727	648
0.1	0.075	662	755	673
0.2	0.15	676	775	695
0.3	0.25	690	790	713
0.4	0.35	703	801	729
0.5	0.45	716	810	743
0.6	0.55	728	818	756
0.7	0.65	740	824	767
0.8	0.75	751	830	778
0.9	0.85	761	836	788
1.0	0.95	771	841	797

Table 3.2 integrated heat with depth for each model

The various heating rates in the top metre are perhaps best illustrated by examining the integrated heat with depth, see Table 3.2. The 9 band model delivers a total of 841 W m^{-2} to the top metre which is 70 W m^{-2} more than the 2 band model and 44 W m^{-2} more than the 278 band model. It will become clear in the next chapter that for conditions of low mixing and high incident radiation, the way in which radiation is distributed in the ocean model is not insignificant. The degree of layer heating affects stratification and therefore turbulent mixing.

It is clear from Figure 3.8 that the longer wavelengths (> 900 nm) of the 2 band model are not attenuated strongly enough. The bi-modal distribution may be acceptable for a coarse ocean model grid (layer depth O(1 m)) where the heat would be averaged across the coarse surface layers. However such a broad band approach would incorrectly distribute heat in the fine resolution grid (minimum layer depth O(10 mm), Figure 3.8.

The 9 band distribution in Figure 3.8 might at first appear an improvement on the bi-modal distribution but this model also misses variations on fine scales. Proportions of SSI are too high in bands that are attenuated at cm scales (important for SST at low wind speeds and high insolation). Too much heat might now be delivered to the top model layers leading to over-stratification, suppression of mixing and over-predicted SSTs. For example, 8.0 % of the solar radiation is assigned to band 5 in the Paulson and Simpson (1981) model, whereas only 5.5 % of SSI is calculated for this band using the radiative transfer model MODTRAN. When the SSI is high, e.g. 1000 W m^{-2}, the difference between the models for just this band is 25 W m^{-2}.

Wavelengths shorter than 1200 nm generally have attenuation lengths greater than O(1 cm) and at 1200 nm there remains, at 1 cm depth, at least 1/3 of the intensity of the spectral SSI. Therefore a degree of detail for wavelengths shorter than 1200 nm is justified. Wavelengths longer than 1800 nm generally

have attenuation lengths less than O(1 mm) and less than 1 % of the spectral SSI remains at 1 cm. The power in the region of the solar spectrum with wavelengths greater than 1800 nm is a small percentage of the total power so the energy below 1cm becomes negligible for wavelengths greater than 1800 nm. Therefore, for grids with minimum layer depth of 1cm, an average attenuation length is all that is required for wavelengths longer than 1800 nm.

3.1.9 Geometrical modifications

So far, only vertically entrant radiation has been considered. There are however two geometrical factors to be acknowledged. Firstly, solar radiation is partly diffused by passing through the Earth's atmosphere. In the ocean, diffused radiation is more strongly attenuated than direct radiation. Secondly, when the sun is not at zenith (Figure 3.10 a), the direct component strikes the ocean surface at an angle and is also refracted, see Figure 3.10 b. Therefore the direct entrant radiation I_0^{direct} makes an angle r with vertical and the attenuation length in the vertical direction is effectively $\zeta\cos(r)$, i.e. less than ζ.

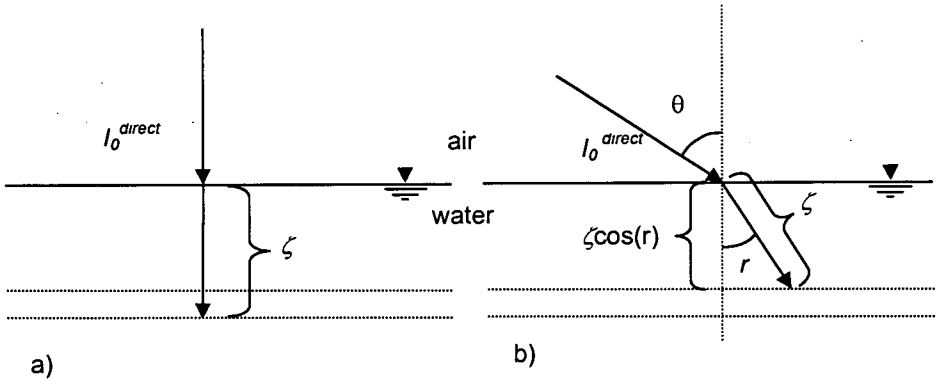

I_0^{direct} is the direct SSI incident at the surface. θ is the solar zenith angle.
r is the angle that the entrant radiation makes with zenith.
ζ is an attenuation length.

Figure 3.10 Geometry associated with attenuation of solar radiation in water.

Diffuse radiation enters the water in all directions and the attenuation lengths of diffuse light will be different to the direct beam attenuation lengths that were obtained by researchers using direct beams in their experiments. A 3/5 factor was applied to the direct beam attenuation lengths in accord with the diffuse approximation (Andrews, 2000). For isotropic radiation, this is a good approximation and is used here to avoid the unjustified level of complication involved in integrating the radiation stream over all incidence angles.

Geometrical aspects of attenuation such as solar zenith angle and the direction of entrant radiation after refraction have generally been ignored in the oceanographic literature. Jassby and Powell (1975) did consider these effects in a study of the diffusivity of a stratified lake. To my knowledge, this current study is the first research to account for these geometrical effects in an ocean turbulence model.

The Paulson and Simpson (1981) 9 band model was modified to include geometrical effects, (equations (3.9) and (3.10) with n =9).

$$I(z)^{direct} = \left(1-\alpha^{direct}\right) I_0{}^{direct} \sum_{i=1}^{n} F_i \exp\left(\frac{z}{\zeta_i \cos(r)}\right) \tag{3.9}$$

$$I(z)^{diffuse} = \left(1-\alpha^{diffuse}\right) I_0{}^{diffuse} \sum_{i=1}^{n} F_i \exp\left(\frac{z}{3/5\,\zeta_i}\right) \tag{3.10}$$

where r is the angle of direct refracted entrant radiation. The diffuse albedo $\alpha^{diffuse}$ varies between 0.05 and 0.10 for different wavelengths, Defant (1961). The direct albedo is 0.06.

The same Paulson and Simpson model but with SSI fractions derived using the radiative transfer model COART and the new 278 band model were also modified as per equations (3.9) and (3.10) with n=9 and 278 respectively.

Under clear-sky conditions, the diffuse radiation forms a small part of the total SSI and is comprised entirely of the deeper penetrating blue to green wavelengths. Diffuse SSI is therefore less significant for studies of strong diurnal warming under clear sky conditions. It is included for completeness and may prove useful for studying diurnal warming with partial cloud cover where the diffuse SSI is larger and includes longer wavelengths attenuated closer to the surface.

3.1.10 Short wave radiation summary

To model the ocean heating from short-wave radiation, solar radiation incident at the ocean surface is first divided into a number of discrete wavelength bands. The fractions of SSI in each band were obtained from a number of sources including the literature and two radiative transfer models, COART and MODTRAN.

The wavelength dependent attenuation lengths of the entrant solar radiation within the water column were obtained from the literature. For the 278 band model, attenuation lengths were interpolated from the Segelstein (1981) data (Figure 3.3 to 3.8) that essentially encompasses the solar spectrum and these were equivalent to nearly every other data set for wavelengths longer than 600 nm. Five options for the short wave radiation set were therefore defined as follows.

Option number	No. of bands	Source of SSI fraction	Source of attenuation length	Solar geometry included	Source of diffuse and direct
1	2	P&S (1977)	P&S (1981)	No	GOTM
2	9	P&S (1981)	P&S (1981)	Yes	GOTM
3	9	COART	P&S (1981)	Yes	GOTM
4	9	MODTRAN	P&S (1981)	Yes	GOTM
5	278	MODTRAN	Segelstein (1981)	Yes	MODTRAN

P&S = Paulson and Simpson.

3.2 Turbulent flux forcing

This Section is about calculating momentum flux, latent heat flux and sensible heat flux at the air-sea interface. These are known as the turbulent fluxes. The turbulence of the atmospheric boundary layer directly influences them but not the radiative fluxes, which are described in Sections 3.1 and 3.3.

The conservation equation for the ensemble mean of variable *x*, denoted as X, is

$$\frac{\partial X}{\partial t} + \nabla_h X \cdot U_h = -\frac{\partial\left(\overline{w'x'}\right)}{\partial z} + \overline{S_x} \qquad (3.11)$$

where the subscript *h* denotes the horizontal components and S_x here represents the source term, Fairall et al (2003). The quantity of interest is the vertical, "Reynolds" flux $\left(\overline{w'x'}\right)$. w' is the rapidly varying component of velocity in the vertical; x' is the rapidly varying property pertaining to the flux, e.g. the fluctuating velocity component in the direction of the wind or the fluctuating part of a scalar, such as temperature; *U* is the velocity of the mean flow.

To obtain the momentum flux, latent heat flux and sensible heat flux, *x* is set to the *u* and *v* wind components, the water vapour specific humidity *q*, and the potential temperature θ, respectively.

3.2.1 Methods of obtaining the turbulent fluxes

Direct method

There is only one direct method of obtaining the fluxes and that is the covariance or eddy correlation method. With this method, the Reynolds flux is determined by the mean product of the time or space series of *w'* and *x'*. Direct covariant measurements of *w'* and *x'* are not routine and require great care processing the time series with respect to the location of the measurement site (Kantha and Clayson, 2000). Over the sea, direct flux measurements require the use of sufficiently responsive sensors to sample

turbulent fluctuations of the required flux (Smith *et al.*, 1996). Additional complications include platform motion, flow distortion over the platform and contamination by sea spray and salt (Fairall *et al.* ,2003) and the heat island effect of the platform (Kantha and Clayson, 2000).

Indirect methods

There are several indirect methods of flux estimation that have been developed because of the paucity of direct measurements. So-called bulk formulae to estimate surface fluxes are widely used in numerical models. The fluxes are expressed in terms of mean quantities as follows,

$$\overline{w'x'} = c_x^{1/2} c_D^{1/2} U \Delta X = C_x U \Delta X \tag{3.12}$$

where c_x is the transfer coefficient for the variable x, c_D is the transfer coefficient for wind (D for 'drag') and C_x is the total transfer coefficient. ΔX is the difference between property X at a measurement height and a surface value of X.

Bulk formulae yield estimates of the surface fluxes only, whilst the correlation method is general (Fairall *et al.*, 2003). Bulk formulae are however the only practical way to establish the surface fluxes in numerical models (Smith *et al.*, 1996).

3.2.2 Vertical fluxes at the surface

Momentum flux

The vertical flux of momentum must be conserved across the air-sea interface. Momentum is transferred by shear stresses at the interface. Continuity of stresses across the interface gives:

$$\tau_a + \tau_{pr} = \tau_w + \tau_{wv} \tag{3.13}$$

where τ_a is the air-side wind stress, τ_w is the water-side shear stress, τ_{wv} is the momentum flux radiated out by wind-generated propagating surface waves and τ_{pr} is the momentum flux due to precipitation.

τ_w is the drag exerted by the ocean on the atmosphere. Through this term, momentum is directly transferred to the ocean currents. For a fully developed wave field, momentum flux generating the waves is immediately transferred to the ocean currents and τ_{wv} can be neglected. In the absence of precipitation, $\tau_w = \tau_a$.

The vertical flux of horizontal momentum at the surface is given by the bulk formulae for calculating the shear stress from wind measurements,

$$\tau = \rho C_D (U_a - U_s)^2 \tag{3.14}$$

where ρ is the air density, U_a is the mean wind speed at the measurement height, U_s is the component of velocity at the surface along the wind direction and C_D is a drag coefficient at the measurement height. The central problem is to determine the drag coefficient, C_D. This is far from straightforward since C_D depends on the wind speed and the stability of the atmosphere which in turn has a dependence on the surface stress.

A useful quantity known as the friction velocity u_* is related to the velocity difference (U_a-U_s) by the height dependent drag coefficient C_D,

$$u_* = \sqrt{C_D (U_a - U_s)^2} \tag{3.15}$$

Therefore, τ can be written as,

$$\tau = \rho u_*^2 \tag{3.16}$$

Heat fluxes

The bulk formulae for the latent (H_L) and sensible (H_S) heat fluxes are,

$$H_L = \rho L_E (U_a - U_s) C_E (q_s - q_a) \tag{3.17}$$

$$H_S = \rho c_p (U_a - U_s) C_H (T_s - T_a) \tag{3.18}$$

respectively where L_E is the latent heat of evaporation, c_p is the specific heat, C_E and C_H are transfer coefficients of heat and water vapour respectively. q is the specific humidity and T is the temperature. The subscripts a and s denote values for the atmosphere at the measurement height and immediately above the surface respectively.

Analogous to the friction velocity, friction quantities for humidity q_* and heat θ_* can be defined, so that the latent and sensible fluxes can be written as,

$$H_L = \rho L_E u_* q_* \tag{3.19}$$

$$H_S = \rho c_p u_* \theta_* \tag{3.20}$$

Again, the difficulty is in determining the transfer coefficients, C_E and C_H or equivalently the friction quantities.

The bulk exchange coefficients over the ocean are a function of height, wind speed at that height, air stratification and the surface wave field. Measurements of the surface wave field are not routine but over the open ocean it is assumed that the surface wave field is fully developed and the surface roughness can be deduced without the details of the wind-wave spectrum. Height dependence can be avoided by considering values at a standard reference height. Therefore most empirical formulae concentrate on the dependence of the bulk exchange coefficients on only the wind speed and stability of the atmosphere.

3.2.3 Surface roughness and the Charnock formula

The drag coefficient, that appears in all the bulk parameterisations for surface fluxes, see equation (3.12), is related to the surface roughness of the ocean. A

surface roughness length for momentum can be defined as the height where the logarithmic profile intersects the surface value. The 'neutral' transfer coefficient is related to the momentum roughness lengths z_0 by:

$$c_{DN}^{1/2} = \frac{\kappa}{\ln\left(\frac{z}{z_{0x}}\right)} \tag{3.21}$$

where N denotes that the coefficient applies to neutrally stable atmospheres. Realistic values for the momentum bulk transfer coefficient are, $1\text{x}10^{-3} \leq c_D \leq 2\text{x}10^{-3}$ (Toba, 2003).

Charnock's formula for the momentum roughness length can be expressed as,

$$z_0 = \frac{\alpha}{g} u_*^2 \tag{3.22}$$

where α is the Charnock "constant". α is also known as the non-dimensional roughness parameter (Charnock, 1955). Values for α in equation (3.22) of 0.010 to 0.035, have been determined by various authors (e.g. Garratt, 1992).

When α is expressed as a function of wave age, the data suggests this range might be wider (see Figure 3.11). The formula in Figure 3.11 is given by,

$$\frac{gz_0}{u_*^2} = \begin{cases} \left(\frac{u_*}{c_p}\right)^{-1} \exp\left[-0.14\left(\frac{u_*}{c_p}\right)^{-1}\right], & \frac{1}{35} < \frac{u_*}{c_p} < \frac{1}{0.35} \\ 0.008, & \frac{u_*}{c_p} \leq \frac{1}{35} \text{ (light winds over swell).} \end{cases} \tag{3.23}$$

where c_p is the phase speed of the surface waves (Toba, 2003)

This formula places α in the range $0.008 < \alpha < 0.08$.

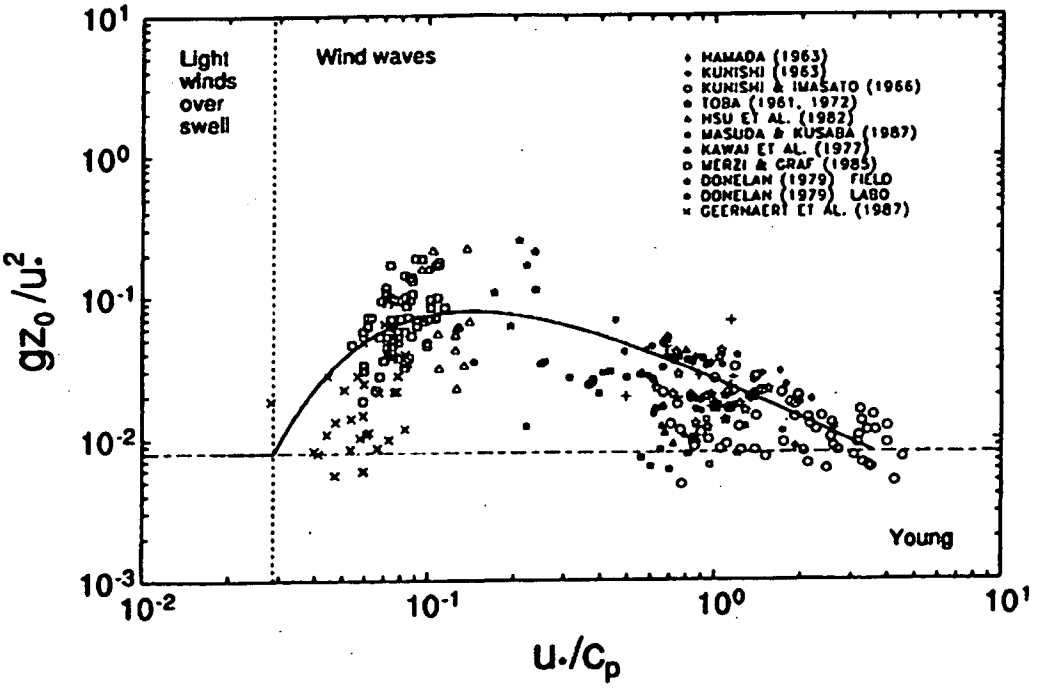

Figure 3.11 A formula for the non-dimensional roughness parameter gz_0/u_*^2 as a function of inverse wave age u_*/c_p together with a data set of observed values, following Toba (2003).

Charnock's formula underestimates the value of the momentum roughness length in vanishing windspeeds. Smith (1988) corrected for this by representing the roughness length as the sum of Charnock (equation (3.22)) and viscous terms by

$$z_0 = \frac{\alpha}{g}u_*^2 + \beta\frac{\nu}{u_*} \tag{3.24}$$

where $\nu = 1.4\times10^{-5}\,\mathrm{m^2 s^{-1}}$ is the viscosity of air and β=0.11 is often used.
The second term in equation (3.24) is negligible for wind speeds above 6 m s^{-1} (Smith *et al.*, 1996).

The scalar roughness scales for humidity z_{0E} and heat z_{0H} can differ significantly from the momentum roughness length z_0. The 'neutral' transfer

coefficients for humidity c_{EN} and heat c_{HN} are related to their respective roughness lengths z_{0E} and z_{0H}, by,

$$c_{EN}^{1/2}, c_{HN}^{1/2} = \frac{\kappa}{\mathrm{Pr}_t \ln\left(\frac{z}{z_{0E}, z_{0H}}\right)} \tag{3.25}$$

where Pr_t is the turbulent Prandtl number. The normal range for the scalar neutral transfer coefficients is $1\text{x}10^{-3} \leq c_{E,H} \leq 1.5\text{x}10^{-3}$ (Toba, 2003).

3.2.4 Monin Obukhov Similarity Theory (MOST)

It is difficult to describe the profiles of mean variables because of their dependence on initial and boundary conditions. However, the profiles often exhibit a common shape, allowing similarity expressions to be derived for the gradients of the mean variables (Stull, 1988). For any property X at a point z far away from the roughness elements and from the edge of the boundary layer (thickness δ), its gradient, $\partial X/\partial z$ is independent of both z_0 and δ. $\partial X/\partial z$ can be expressed as a function of height above the boundary z, the friction velocity u_*, the kinematic flux of the property Q_X and the buoyancy flux Q_b,

$$\frac{dX}{dz} \sim f(z, u_*, Q_X, Q_b) \tag{3.26}$$

In non dimensional form,

$$\phi_X = \frac{\kappa z}{X_*}\frac{\partial X}{\partial z} = \phi_X\left(\frac{z}{L}\right) = \phi_X(\zeta) \tag{3.27}$$

where,

$$X_* = \frac{Q_X}{u_*}, \tag{3.28}$$

the length scale L is given by,

$$L = \frac{u_*^3}{\kappa Q_b} \tag{3.29}$$

and

$$\zeta = \frac{z}{L} \tag{3.30}$$

is the Monin Obukhov similarity variable. The buoyancy flux can be written as,

$$Q_b = \frac{g\theta_{v*}}{T_v} \tag{3.31}$$

where θ is the potential temperature ($_*$ denotes friction quantity) and the subscript v denotes virtual quantities, e.g. T_v is the absolute virtual temperature,[3]

$$T_v = (1+0.61q)T \tag{3.32}$$

where q is the specific humidity. Thus the velocity, temperature and humidity profiles can be written in dimensionless form, following equation (3.27):

$$\phi_M(\zeta) = \frac{\kappa z}{u_*}\frac{\partial U}{\partial z} \tag{3.33}$$

$$\phi_H(\zeta) = \frac{\kappa z}{\theta_*}\frac{\partial T}{\partial z} \tag{3.34}$$

$$\phi_E(\zeta) = \frac{\kappa z}{q_*}\frac{\partial q}{\partial z} \tag{3.35}$$

For neutrally stable atmospheres, $\phi_{M,E,H}$ =1 and equations (3.33) to (3.35) can simply be integrated to obtain the logarithmic profiles of the mean properties,

$$\frac{U(z)-U_s}{u_*} = \frac{1}{\kappa}\left[\ln\frac{z}{z_0}\right] = \frac{1}{c_{DN}^{1/2}} \tag{3.36}$$

$$\frac{q(z)-q_s}{q_*} = \frac{\mathrm{Pr}_t}{\kappa}\left[\ln\frac{z}{z_{0E}}\right] = \frac{c_{DN}^{1/2}}{c_{EN}} \tag{3.37}$$

$$\frac{T(z)-T_s}{\theta_{*v}} = \frac{\mathrm{Pr}_t}{\kappa}\left[\ln\frac{z}{z_{0T}}\right] = \frac{c_{DN}^{1/2}}{c_{HN}} \tag{3.38}$$

In the case of non-stable atmospheres,

[3] The definition of **virtual temperature** (Tv) is the temperature to which a sample of dry air must be heated in order to have the same density as a sample of moist air at the same pressure.

$$\frac{U(z)-U_s}{u_*}=\frac{1}{\kappa}\left[\ln\left(\frac{z}{z_0}\right)-\psi_M(\zeta)\right] \tag{3.39}$$

$$\frac{q(z)-q_s}{q_*}=\frac{\mathrm{Pr}_t}{\kappa}\left[\ln\left(\frac{z}{z_{0E}}\right)-\psi_E(\zeta)\right] \tag{3.40}$$

$$\frac{T(z)-T_s}{\theta_{*v}}=\frac{\mathrm{Pr}_t}{\kappa}\left[\ln\left(\frac{z}{z_{0T}}\right)-\psi_H(\zeta)\right] \tag{3.41}$$

where,

$$\psi_{M,E,H}(\zeta)=\int_0^{\zeta}\left[1-\phi_{M,E,H}(\zeta')\right]\frac{d\zeta'}{\zeta'} \tag{3.42}$$

are the stability functions.

Equations (3.36) to (3.38) can be rearranged to find the friction values of the respective quantities u_*, q_*, θ_*. The main task is to evaluate the length scale, L (and hence ζ), which can be done by iteration.

Following Kantha and Clayson (2000), equations for the stability functions in terms of ζ are;

$$\psi_M(\zeta)=2\ln\left(\frac{1+x}{2}\right)+\ln\left(\frac{1+x^2}{2}\right)-2\tan^{-1}x+\frac{\pi}{2} \qquad (\zeta<0) \tag{3.43}$$

$$\psi_M(\zeta)=-\beta_1\zeta \qquad (\zeta>0) \tag{3.44}$$

for the velocity profile, where,

$$x=\frac{1}{\phi_M(\zeta)}=(1-\gamma_1\zeta)^{1/4} \tag{3.45}$$

and;

$$\psi_{H,E}(\zeta)=2\ln\left(\frac{1+y}{2}\right) \qquad (\zeta<0) \tag{3.46}$$

$$\psi_{H,E}(\zeta)=-\beta_2\zeta \qquad (\zeta>0) \tag{3.47}$$

for the scalar profiles, where,

$$y = \frac{1}{\phi_{H,E}(\zeta)} = (1 - \gamma_1 \zeta)^{1/2} \tag{3.48}$$

Various forms have been derived for these functions (e.g. Beljaars 1994, Large *et al.*, 1994) but the large scatter in the basic observations leaves uncertainty as to the most applicable (Kantha and Clayson, 2000).

3.2.5 Transfer coefficients

The neutral transfer coefficients are determined by only the corresponding roughness scales, Section 3.2.3. In non-neutral conditions, the transfer coefficients are also functions of stratification. From similarity theory (Section 3.2.4) the transfer coefficients can be written as:

$$C_D = \kappa^2 \left[\ln \frac{z}{z_0} - \psi_M(\zeta) \right]^{-2} \tag{3.49}$$

$$C_{H,E} = \kappa^2 \left[\ln \frac{z}{z_{0T}} - \psi_H(\zeta) \right]^{-1} \left[\ln \frac{z}{z_{0T,0E}} - \psi_{H,E}(\zeta) \right]^{-1} \tag{3.50}$$

Calculating the bulk exchange coefficients is equivalent to determining the roughness scales of each property *and* the stratification and vice versa.

3.2.6 Options

Five (MOST based) options were chosen for calculating turbulent fluxes.

Kondo (1975)

Kondo represented the neutral transfer coefficients in terms of approximate formulae as follows;

$$C_{DN10} = a_d + b_d U_{10}^{p_d} \tag{3.51}$$

$$C_{HN10} = a_h + b_h U_{10}^{p_h} + c_h (U_{10} - 8)^2 \tag{3.52}$$

$$C_{EN10} = a_e + b_e U_{10}^{p_e} + c_e (U_{10} - 8)^2 \tag{3.53}$$

The parameters a_d, a_h, a_e, b_d, b_h, b_e, c_h, c_e, p_d, p_h, p_e are tabulated for five bands of wind speed to cover the range 0.3 to 50 m s^{-1}.

The transfer coefficients are then derived from the neutral transfer coefficients by an approximate stability formula,

$$S = S_0 \frac{|S_0|}{|S_0| + 0.01} \tag{3.54}$$

where,

$$S_0 = \frac{(T_s - T_a)}{U^2 (1.0 + \log_{10}(10/z))^2} \tag{3.55}$$

For stable conditions (T_s-T_a <0),

$$\begin{aligned} &\frac{C_{D10}}{C_{DN10}} \approx \frac{C_{H10}}{C_{HN10}} \approx \frac{C_{E10}}{C_{EH10}} \\ &\approx 0.1 + 0.03S + 0.9\exp(4.8S), \quad \text{(for } -3.3 < S < 0\text{)} \\ &\approx 0, \quad \text{(for } S \leq -3.3\text{)} \end{aligned} \tag{3.56}$$

and for unstable conditions (T_s-T_a >0),

$$\begin{aligned} &\frac{C_{D10}}{C_{DN10}} \approx 1.0 + 0.47\sqrt{S} \\ &\frac{C_{H10}}{C_{HN10}} \approx \frac{C_{E10}}{C_{EH10}} \approx 1.0 + 0.63\sqrt{S} \end{aligned} \tag{3.57}$$

The Kondo formulae coded in GOTM require wind speed at 10 m height above the surface. Buoy anemometers are generally at a height of about 4

metres. Therefore it is necessary to infer the wind at 10 m from the wind at the measurement height. For the Kondo option, a logarithmic profile was assumed with roughness length from the Charnock formula.

Smith (1988)

Smith (1998) developed four tables to infer the wind at 10 m from wind measured at heights of 1, 2, 5 and 20 metres in stable or unstable atmospheres. Tabulated wind speeds at the measurement height span a range of 2 to 36 m s^{-1}. The stability range is -10 °C < T_s-T_a < 10 °C in 8 intervals.

ΔT (°C)	U_5 (m s^{-1})					
	2	4	8	16	24	36
-10	1.32	1.32	1.17	1.09	1.09	1.10
-5	1.32	1.32	1.12	1.09	1.09	1.10
-3	1.26	1.21	1.10	1.08	1.09	1.10
-1	1.26	1.11	1.07	1.08	1.09	1.10
0	1.06	1.06	1.06	1.08	1.09	1.10
1	1.03	1.04	1.06	1.07	1.09	1.10
3	1.03	1.04	1.05	1.07	1.08	1.10
5	1.02	1.03	1.05	1.07	1.08	1.10
10	1.02	1.03	1.04	1.07	1.08	1.10

Table 3.3 Conversion factors to apply to wind speed measured at 5 m anemometer height to obtain wind speed at 10 m.

From the tables (example Table 3.3) a conversion factor can be computed by interpolating between stability intervals and then between the two tables that bound the measurement height. The 10 m wind calculated in this way is then used in the Kondo (1975) formulae to compute the transfer coefficients as above.

Large and Pond (1981)

This method is an application of similarity theory using a bulk estimate of the stability parameter $\zeta = z/L$.

The bulk estimate of $\zeta = z/L$ is,

$$\frac{z}{L} = -\kappa C_T C_D^{-3/2} Ri(\Delta T) \tag{3.58}$$

where C_D is a neutral value ~ 1.25×10^{-3} and C_T is ~ 1.0×10^{-3} for unstable conditions and ~ 0.86×10^{-3} in stable conditions. Ri is a bulk Richardson number approximated by,

$$Ri(\Delta T) = -\frac{gz\Delta T}{(U_z)^2 T_0}\left(1 + T_0^2 \frac{\Delta Q}{\Delta T} 1.72 \times 10^{-6}\right) \tag{3.59}$$

ΔT is the air-sea temperature difference and T_0 is the temperature of air at the surface, estimated by,

$$T_0 \approx T_a + T_a^2 q_a \left(1.72 \times 10^{-6}\right) \tag{3.60}$$

The wind at 10 m height is found from,

$$U_{10} = U_z + \left[\frac{u_*}{\kappa}\right]\left[\ln\left(\frac{z}{10}\right) - \psi_m\left(\frac{z}{L}\right) + \psi_m\left(\frac{10}{L}\right)\right] \tag{3.61}$$

where the stability functions are calculated using the equations (3.43) to (3.48).

AM96 – Abdella and d'Allessio (2003)

This method is an application of similarity theory using iteration to solve the equations for the stability parameter, $\zeta = z/L$. There is also a modification to Charnock's formula, which underestimates the value of the momentum roughness in the free convection limit (Abdella and d'Allessio, 2003). Abdella and d'Allessio propose;

$$z_0 = \frac{\alpha}{g}\left(u_*^2 + \gamma w_*^2\right) \tag{3.62}$$

The two contributions then are from mechanically generated turbulence (wind driven) and thermally generated (heat-induced) turbulence. $\gamma \sim 0.15$ is found to be a reliable estimate (Abdella and d'Allessio, 2003).

The algorithm is called AM96 and is used in the GCM of the Canadian Centre for Climate Modelling. Although some iteration is required, a first estimate of the stability parameter is made from a Bulk Richardson number to reduce the number of required iterations.

COARE 3.0 (Fairall *et al.*, 2003)

COARE 3.0 is found by the authors to be accurate to within 5% for wind speeds U where $0 \leq U \leq 10$ m s^{-1} and 10% for $10 \leq U \leq 20$ m s^{-1} (Fairall, 2003). Twenty years earlier, bulk flux schemes were considered to be uncertain by about 30%. A large amount of data was used to improve the performance of COARE 3.0 over previous versions of the algorithm and increase it's validity over a wider geographical area.

The algorithm uses MOST to estimate the bulk exchange coefficients (see Section 3.2.4). The number of iterations used to derive the stability parameter was reduced using a bulk Richardson number formula as a first estimate. The momentum roughness length includes the smooth flow limit following Smith (1988), equation (3.24).

Recall from Section 3.2.1 that the fluxes are expressed in terms of mean quantities c.f. equation (3.12)

$$\overline{w'x'} = c_x^{1/2} c_D^{1/2} U \Delta X = C_x U \Delta X \tag{3.63}$$

If it is gusty and the wind significantly varies (non-monotonically) between observations, then the fluxes might be under-predicted. In COARE 3.0, there is a gustiness component u_g in the wind speed U to account for sub-grid scale variability (i.e. between observations)

$$U = \left(u^2 + v^2 + u_g^2\right)^{1/2} \tag{3.64}$$

where u and v are the mean vectors of eastward and northward wind speed.

The COARE algorithm also incorporates parameterisations that represent the cool skin (see chapter 1) and the diurnal warm layer above the depth at which SST is specified.

3.2.7 Implementing turbulent flux options in GOTM

There are two ways of implementing the surface turbulent heat and momentum fluxes into the current version of GOTM. They are either pre-calculated and read in from files or calculated within GOTM from standard meteorological data, also supplied from files.

In the public domain version of GOTM the bulk formulae of Kondo (1975) are used to calculate the latent heat, sensible heat and the surface shear stress. These formulae and most other bulk formulae require: sea surface temperature (SST); air temperature; humidity; and air pressure (each at 2 m height) and also the wind velocity at 10 m height in the Northwards and Eastwards directions. The GOTM web site states that since the Kondo (1975) bulk formulae are fairly old, they should soon be replaced by newer versions, such as those suggested by Fairall *et al.* (1996). This has not yet been done and therefore by incorporating a number of options for determining the turbulent fluxes in option-set 4, I have improved the utility of the GOTM air-sea module.

3.3 Downwelling longwave radiation

The net longwave radiation consists of upwelling and downwelling components. Longwave radiation is attenuated very rapidly in water and therefore, it can be assumed that all the downwelling longwave radiation is absorbed in the top few μm of the ocean (see Section 3.1) and all upwelling

longwave radiation leaves from the top few micrometres. Longwave radiation can therefore be treated as a net quantity in the heat budget.

$$Q_L^{\uparrow\downarrow} = Q_L^{\uparrow} - Q_L^{\downarrow} \tag{3.65}$$

where ↑ implies upwelling and ↓ implies downwelling and ↑↓ implies a net quantity. The upwelling component depends on the sea temperature and on the emissivity of sea water and is therefore easy to parameterise.

$$Q_L^{\uparrow} = \varepsilon_L \sigma T^4 \tag{3.66}$$

where ε_L is the longwave emissivity of sea water, σ is the Stefan-Boltzman constant and T is the skin SST.

Downwelling longwave radiation from the atmosphere is more complex and depends on profiles of air temperature and humidity and cloud amount, cloud type and height and also fog.

Brunt (1932) developed a formula linking net longwave radiation to meteorological parameters of clear skies.
For clear skies,

$$Q_L^{\downarrow} = \varepsilon_L \sigma T_a^4 \left(a + b\sqrt{e}\right) \tag{3.67}$$

where a and b are empirically derived coefficients and e is the near surface vapour pressure, T_a is the air temperature. This was later developed, by many authors, for use over water and a cloud fraction included (Zapadka and Wozniak, 2000),

$$Q_L^{\downarrow} = \varepsilon_L \sigma T_a^4 \left(a + b\sqrt{q_h}\right)\left(1 + cN\right) \tag{3.68}$$

where N is a cloud fraction from 0 to 1. Some authors use N^2 rather than N in the cloud correction term (Fung *et al.*,1984).

The parameterisations chosen for this test are based on the Brunt type formula (3.68).

Formulae that are in the public version of GOTM include Clark *et al.* (1974) and Hastenrath and Lamb (1978) [see Burchard *et al.*, GOTM manual, 1999]. Clark *et al.* (1974), set a=0.39 and b=0.05. Zapadka and Wozniak (2000) report that this formula systematically underestimates $Q_L^{\uparrow\downarrow}$ by 13.3 W m^{-2}, and that Hastenrath and Lamb (1978) systematically underestimates $Q_L^{\uparrow\downarrow}$ by 16.3 W m^{-2}. Clark *et al.* (1974) was chosen for the experiment, since it was reported as less biased.

Grant and Hignett (1998) use the specific humidity q_{air} in their Brunt type formula

$$Q_L^{\downarrow} = \varepsilon_L \sigma T^4 \left(a + b\sqrt{q_{air}}\right) \tag{3.69}$$

with a=0.24 and b=4.33 giving an estimate of downwelling long-wave flux comparable to their measurements in the TOGA-COARE (tropical) area.

The two options for downwelling longwave radiation are,
Clark et al. (1974).
Grant and Hignett (1998).

3.3.1 Longwave radiation and cloud fraction.

Thus far, the data sets used to determine the best settings of the model were all for relatively clear-sky conditions. To use data that includes periods with some cloud, the downwelling longwave-radiation (DLR) for cloudy conditions must be calculated. Few automated buoys are equipped with pyrgeometers (instruments for direct measurements of DLR). There are DLR parameterisations in the literature that account for cloud fraction. However, cloud amount observations are not available from fully automated buoys. An approximation of cloud amount can be calculated using broadband shortwave measurements of SSI.

The formula of Reed (1977) is an estimate of SSI for a given cloud fraction (*cloud*)

$$SSI = SSI_{clear}\left(1 - 0.62cloud + 0.0019\beta\right)\left(1 - A\right) \qquad \text{[0.2 < cloud]} \qquad (3.70)$$

$$SSI = SSI_{clear}\left(1 - A\right) \qquad \text{[cloud} \leq 0.2\text{]} \qquad (3.71)$$

where *SSI* is surface solar irradiance, β is the solar noon altitude in degrees and *A* the ocean albedo. This formula has been almost exclusively used in the oceanographic community (Kizu, 1998). The clear sky SSI (SSI_{clear}) can be obtained from an astronomical algorithm and in GOTM, the algorithm follows Rosati and Miyakoda (1988).

To estimate cloud from SSI, (3.70) can be rearranged to obtain,

$$\begin{aligned} &cloud = \xi \text{ for } \xi > 0.2 \\ &cloud = 0 \text{ for } \xi \leq 0.2 \end{aligned} \qquad \text{where } \xi = 1.62\left[1 + 0.0019\beta - \frac{SSI}{SSI_{clear}\left(1 - A\right)}\right] \qquad (3.72)$$

With this method, a cloud-fraction estimate is only obtained for the daytime. With no other information, nighttime cloud is set to zero. DLR might be underestimated if in reality there is cloud at night but cloud is not present in the forcing meteorology. With persistent low wind conditions, this omission could lead to a drift in the SST.

The Brunt-type formula of Grant and Hignet is then used to calculate net longwave-radiation.

$$Q_L^{\uparrow\downarrow} = \left[\varepsilon_L \sigma T^4 - \varepsilon_L \sigma T_a^4 \left(a + b\sqrt{q_{air}}\right)\right]\left(1 - 0.8cloud\right) \qquad (3.73)$$

T_a is the air temperature, T the sea surface temperature, a=0.24 and b=4.33 and q_{air} is the specific humidity. ε_L is the longwave emissivity of sea water and σ is the Stefan-Boltzman constant.

The cloud estimation (from broadband SSI) procedure has not been validated and is included here only as a possible solution in the absence of cloud data or DLR observations available from instrumented moorings.

3.4 Turbulence mixing scheme

In chapter 2, three model classes for simulating vertical mixing in the ocean column were examined. The turbulence closure type models in GOTM were chosen for this research. These are the MY type and the k-ε models.

Burchard *et al.* (1998) compared the k-ε model with the MY second moment closure model in both oceanographic and open channel contexts. Of relevance to this research, in the context of both neutrally-stratified and stably-stratified flows, they find that the k-ε and MY models perform similarly with respect to the mixed layer depth and the profiles of tke, length scale and eddy diffusivity. However, their performance at SST prediction under conditions of strong diurnal warming was not established.

It is difficult to separate the test of ocean model skill from that of the accuracy of forcing parameterisation. SST is usually the only available validation data. The k-ε and MY one-dimensional turbulence closure models are included in the matrix of option-sets to statistically assess their performance when combined with the large number of forcing options now available. Moreover, further differences between the models may become apparent with the addition of more detailed parameterisations of SSI distribution in the water column.

The basic equations for the MY and k-ε models are given in chapter 2, Section 2.6.3.

3.5 Ocean-leaving flux forcing

Sea surface temperatures are usually measured at a depth of the order of 1 metre. The radiative, latent and sensible heat exchanges across the ocean atmosphere interface however, all depend on the skin sea surface temperature SSST (Clayson and Curry, 1996). In conditions of low wind and strong solar heating, differences of several degrees can occur between the skin and 1 metre depth for several hours of the afternoon (local time), i.e. surface stratification. If there is no SSST measurement, the temperature at 1 metre could be used but there will be an associated error in the calculated fluxes when a strongly stratified ocean layer is present. Note that the COARE 3.0 algorithm has a parameterisation for the warm layer that could reduce this error, depending on the skill of the parameterisation. Alternatively, the fluxes could be calculated simultaneously with the ocean model from the modelled skin temperature.

Using the modelled SSST is not without potential problems however. Of particular concern are the estimations of latent and sensible heat fluxes using bulk formulae. For example, suppose that the specific humidity at the surface is calculated at the modelled SST and the specific humidity at the air temperature measurement height is calculated from the measured air temperature.

The bulk formula for Latent heat flux is

$$H_L = \rho L_E (U_a - U_s) C_{Eh} (q_s - q_a) \tag{3.74}$$

H_L is usually from ocean to atmosphere. Any underestimation of SST then decreases the difference between q_s and q_a and thereby decreases H_L and conversely, any overestimation of SST increases H_L. Therefore, there is a stabilising (negative) feedback. The model could correctly predict SSTs by a combination of incorrect fluxes and incorrect mixing compensating each other which is undesirable.

3.6 Summary

The solar radiation distribution enhancements to the model were summarised in Section 3.1.10. Five options (based on MOST) for calculating turbulent fluxes (including momentum flux) were described. Two options for determining net-longwave radiation were also given and a possible method for including cloud from SSI measurements was also proposed. Also described were options to calculate fluxes directly from observed SST (where appropriate) or interactively with modelled SST.

All of the model options have been described and all of the possible combinations of these options will be tested in the next chapter.

Chapter 4 Testing combinations of options

In chapter 3, options for specifying fluxes were described, together with options to model the mixing of heat in the ocean. The model is now set up in turn with each possible combination of these options. In this chapter, three sets of meteorological and oceanographic data are used to assess performance of all the possible combinations. The option sets, defined in Chapter 3, are summarised in Table 4.1. These options, give a possible 200 combinations (2x5x2x5x2 = 200).

Each data set includes sufficient meteorological variables to either specify or calculate the various fluxes to force the model. Also present are subsurface temperatures with temporal resolution of 15 minutes. These are the observed data with which to compare the modelled temperatures and also provide the first temperature profile with which to initialise the model.

The charts in this chapter would be difficult to read with full combination-descriptions labelling the x-axis. Therefore a code has been used as a label. The code for each combination is given by the numbers in the first column of Table 4.1. For example, code 21252 is a model-run using: the Kappa-epsilon model; the 2 stream solar radiation distribution; Grant and Hignett's (1998) Brunt-type formula for longwave radiation; the COARE 3.0 flux algorithm and modelled SST in all formulae requiring SST to calculate fluxes.

Summary statistics will be used to quickly distil the large volume of results down to a few preferred combinations. I use the Root Mean Square of the difference between modelled and observed properties. Some more detailed analysis will be conducted to ascertain possible reasons for some options' skill over others.

Code	Option sets with possible options
	1. Turbulence mixing scheme
1	Mellor - Yamada type, with Kantha & Clayson stability functions (1994)
2	Kappa - Epsilon type
	2. Short wave radiation parameterisation
1	2 stream model, P & S (1977)
2	9 stream model, P & S (1981), with full geometry
3	9 stream model. Attenuation lengths from P & S (1981) with proportional coefficients from COART,
4	9 stream. Attenuation lengths from P & S (1981) with proportional coefficients from MODTRAN
5	278 stream – MODTRAN. Attenuation coefficients - Segelstein (1981)
	3. Long wave radiation parameterisation
1	Clark formula (1974)
2	Brunt type formula with Grant and Hignett coefficients (1998)
	4. Non – radiative flux calculation from meteorology, including wind stress. Wind measurement is converted to 10 m anemometric height where necessary
1	Kondo (1975) with neutral atmosphere assumption for wind measurement
2	Kondo (1975) with Smith (1988) tables to convert wind to 10 m value.
3	Large and Pond (1981)
4	AM96 method - Abdella and d'Allesio (1996)
5	Fairall et al. (2003), COARE 3.0
	5. Heat flux forcing
1	Precalculated (from meteorological measurements using observed SST)
2	Semi coupled fluxes (using modelled SST)

Table 4.1 Options in each option set, giving 200 combinations.

A note on equifinality

Equifinality is a condition in which different initial conditions lead to similar outcomes. It is possible that an option that incorrectly models heat or mixing in one option set is compensated by options that incorrectly model heat or mixing, in the opposite sense, in other option sets. Interpreting the results in the light of other considerations, i.e. physical consistency, contextual knowledge about the background and merits of different options, the detailed analysis presented here will identify such combinations and they can be eliminated.

4.1 Data Sets

The model is set up with each combination in turn and forced using the meteorology from each of three data sets. The modelled SSTs are then compared with observed SSTs from the corresponding data set. The data sets chosen for this test are given in Table 4.2 with locations and dates.

Data Set	Location	Date
Arabian sea	15N 61E	22/05/1995 to 01/06/1995
COARE	2S156E	28/11/1992 to 08/12/1992
LOTUS	34N70W	13/07/1982 to 23/07/1982

Table 4.2. Data sets with locations and times. COARE is the Coupled Ocean Atmosphere Response Experiment. LOTUS is the LOng Term Upper-ocean Study

The Arabian Sea data set is a year-long record of meteorological and ocean temperature data from a discus buoy deployed for two six-month periods, back to back. The days defined by the dates in Table 4.2 are characterised by several apparently cloud-free days with strong insolation and low wind speed. These are ideal conditions for significant diurnal amplitudes of SST. The observed SSTs and subsurface temperatures also suggest that the data are subject to little, or insignificant, effects from advection. If advection is present,

the horizontal variability occurs over sufficiently large horizontal scales to not affect the temperature profiles at the buoy location. This is good for testing the physics of the one-dimensional model without resorting to ad-hoc measures to compensate for advection effects such as temperature profile 'restoring' methods or assimilation of body source heat. Such techniques will likely affect stratification in the model. The forcing data have a high temporal resolution of 7.5 minutes.

For the Coupled Ocean Atmosphere Response Experiment (COARE) data set, a three metre discus buoy was deployed on 21st October, 1992 and remained moored until 4th March, 1993. It was outfitted with sufficient meteorological sensors to estimate the bulk fluxes of momentum, heat and moisture and air temperature. Sea temperature, conductivity, and velocity sensors were also deployed on the buoy. The measurements spanned the upper 260 m of the water column. Temperature was measured from 0.4 m to 260 m depth with vertical resolution that varied from less than 0.5 m (in the upper 2 m) to 16 m (between 132 and 260 m depth). The time resolution is 7.5 minutes.

The Long Term Upper-ocean Study (LOTUS) data are older than the COARE and Arabian Sea data and less detailed but are also characterised by large diurnal amplitudes of SST. This data set was used by Abdella and d'Allesio to test and validate their flux model, AM96. It was therefore appropriate to include the LOTUS data set in this test since AM96 is one of the options in Table 4.1. The time resolution is 15 minutes. The depths of observed temperature data are given for the three data sets in Table 4.3 and Figure 4.1. Good resolution of the near surface is present in the Arabian Sea and COARE data sets. The LOTUS data have less resolution at the surface but are still a valid test for the model with a temperature sensor at 0.6 m.

Depth of temperature sensors (m)		
ARABIAN	COARE	LOTUS
0.17	0.45	0.6
0.43	0.55	5.0
0.92	1.10	10
1.41	1.58	15
1.80	2.0	20
1.91	2.5	25
2.4	7.0	35
3.5	7.5	50
4.5	9.8	65
5.0	11	75
10	14	100
15	15	
20	18	
25	19	
30	22	
35	25	
40	26	
45	30	
50	34	
55	42	
60	48	
65	55	
80	70	
90	78	
100	86	
	94	
	102	

Table 4.3 Depths of observed temperature data for three data sets.

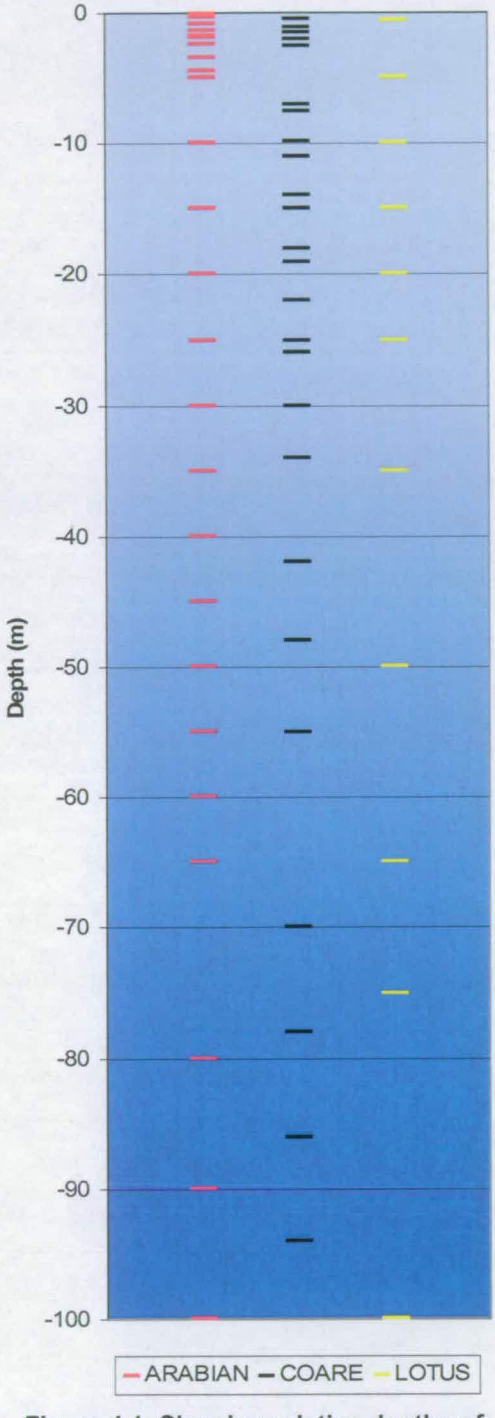

Figure 4.1 Showing relative depths of observed temperature for each data set.

4.2 Definitions of properties for testing model skill

In this chapter, I measure the skill of the model with any given combination of options by how well it can predict the degree of stratification, diurnal amplitude and the actual SST at each output time-step (see Table 4.4). Figure 4.2 is a plot of the modelled and observed SSTs at 0.17 m and 5 m from the Arabian Sea simulation.

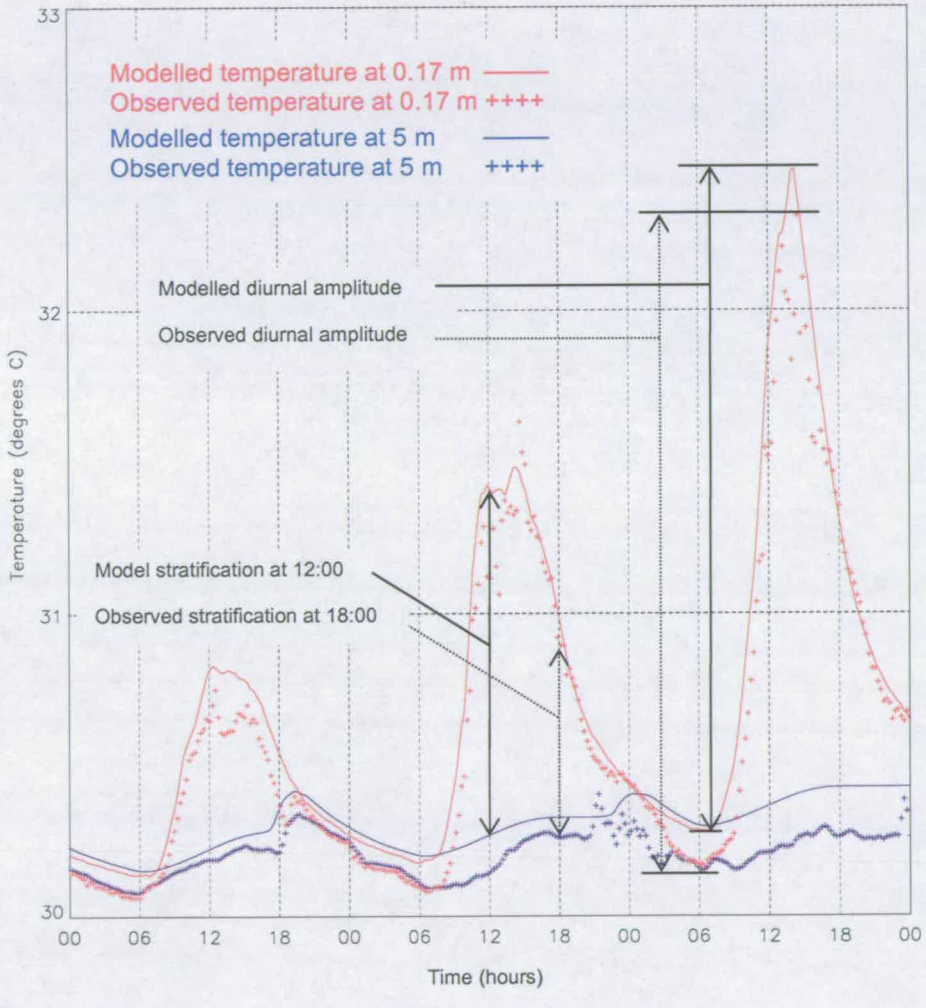

Figure 4.2 Plot showing modelled and observed SST at several time steps, and defining diurnal amplitude, and stratification. This is a 3 day sample from the Arabian Sea data 29/05/1995 to 31/05/1995. See Table 4.4 for definitions of diurnal amplitude and stratification.

The 5 m foundation temperature is arbitrary but most of the diurnal warming occurred above this depth for all three data sets.

The last three days of the 10 day simulation are shown because they exhibit the largest diurnal amplitudes and stratification. Modelled and observed stratification are shown at different times (for clarity) in Figure 4.2 but in the analysis, the modelled stratification is compared with the observed stratification at the same output time-step. Diurnal amplitudes are not necessarily defined by extrema that occur at the same time in the model and the observations, although in Figure 4.2, they are fairly close. Modelled and observed SST are compared at the same output times, i.e. every 15 minutes.

Diurnal amplitude and SST at several depths near the surface are examined and stratification in the top five metres calculated from the shallowest sensor and the sensor at five metres (where available). If there is no sensor at five metres, the five metre temperature is interpolated from the sensors that bound this depth. These terms, illustrated in Figure 4.2, were determined for this test following the methods given in Table 4.4.

Properties	Definitions in this test
SST	Modelled and observed Sea Surface Temperature at sensor depths to 5 m.
Diurnal amplitude	The maximum daytime temperature minus the minimum night-time temperature of the previous night.
Stratification	The temperature at the top sensor minus the temperature at the 5 m sensor.

Table 4.4 Properties to assess model performance and how they were obtained.

Observed temperatures at five metres and below in the LOTUS and COARE data sets are subject to fluctuations of a period consistent with internal waves.

The period for internal waves in realistic stratification is typically of the order hours but can be 30 minutes or less in regions of high stratification (Lighthill, 1978), see Figure 4.3. The model does not include the physics of internal waves, only parameterisations for mixing in the case of breaking internal waves. Variations on diurnal scales are of interest here and so the 5 m observed temperatures were smoothed when calculating observed stratification, using a median smoother with a 24 hour smoothing window. For calculating the RMS of residuals for stratification, this smoother was applied to the 5 m observed temperature for all three data sets, for consistency. The temporal resolution of the measure of stratification is the same as the output time-step i.e. 15 minutes.

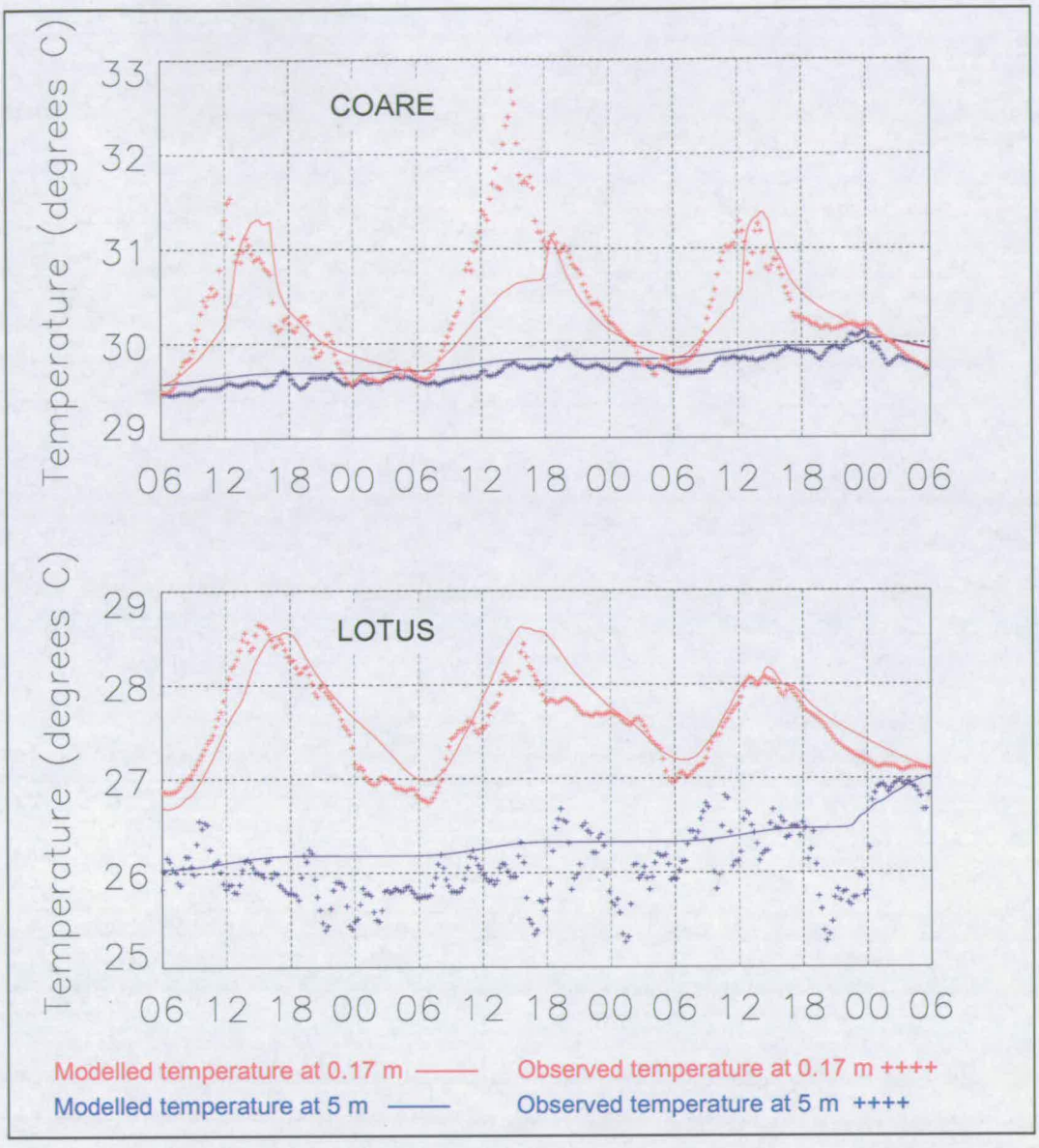

Figure 4.3 Plots showing modelled and observed SST at several time steps for 3 days of the COARE data (top) and the LOTUS data (bottom).

4.3 Root mean square of residuals

The large number of combinations to analyse suggests the need for summary statistics to assess each combination's performance. There are 200 combinations to examine over three data sets. I use the root mean square,

RMS, of the difference between the modelled values and the observed values as a first test. For temperature, the units of all RMS difference values quoted hereafter are °C. The differences between the modelled values and the observed values are called the residuals. These values might be temperature at a specified depth, diurnal amplitude at a specified depth or stratification, i.e. the properties described in Table 4.4.

The root mean square of the residuals, *R(x)* is given by,

$$R(x) = \sqrt{\frac{1}{N}\sum_i \left(x_i^{modelled} - x_i^{observed}\right)^2} \tag{4.75}$$

where *N* is the number of values in the analysis, e.g. output time-steps or number of days of a run in the case of diurnal amplitude. The property being analysed (i.e. temperature) at each time interval, *i*, is x_i.

4.4 Approach to selecting the best combinations

It is useful to start with pair-wise comparisons within option-sets with only two options. Pair-wise comparisons within an option set means that for all possible combinations in the other option-sets, the two options are compared on their merit alone, i.e. all else is equal. If there is an obvious advantage to one of the options, this should be readily seen on a pair-wise comparison chart. The RMS residuals of properties of the pairs can also be sorted and the lowest 10 values compared. In this way, the number of combinations to analyse can be reduced quickly.

4.5 Option-set 1, turbulence closure model

The first option-set in Table 4.1 is the turbulence mixing scheme with just two options. Starting with this set then, I compare the Mellor-Yamada (MY) type model to the kappa-epsilon (k-e) model. The Mellor Yamada model here is the Kantha and Clayson (1994) improved version, see Section 3.4 in chapter 3. Hereafter, this model is referred to as, 'MY type (K&C, 1994)'.

In Figure 4.4 and all pair-wise comparison charts in this chapter, an asterisk is used as a 'wild-card' in the code in the x-axis. The asterisk replaces the numbers corresponding to the options in the option-set being compared, thereby halving the number of x-axis labels required on each chart. The red bars are pair-wise compared to the blue bars.

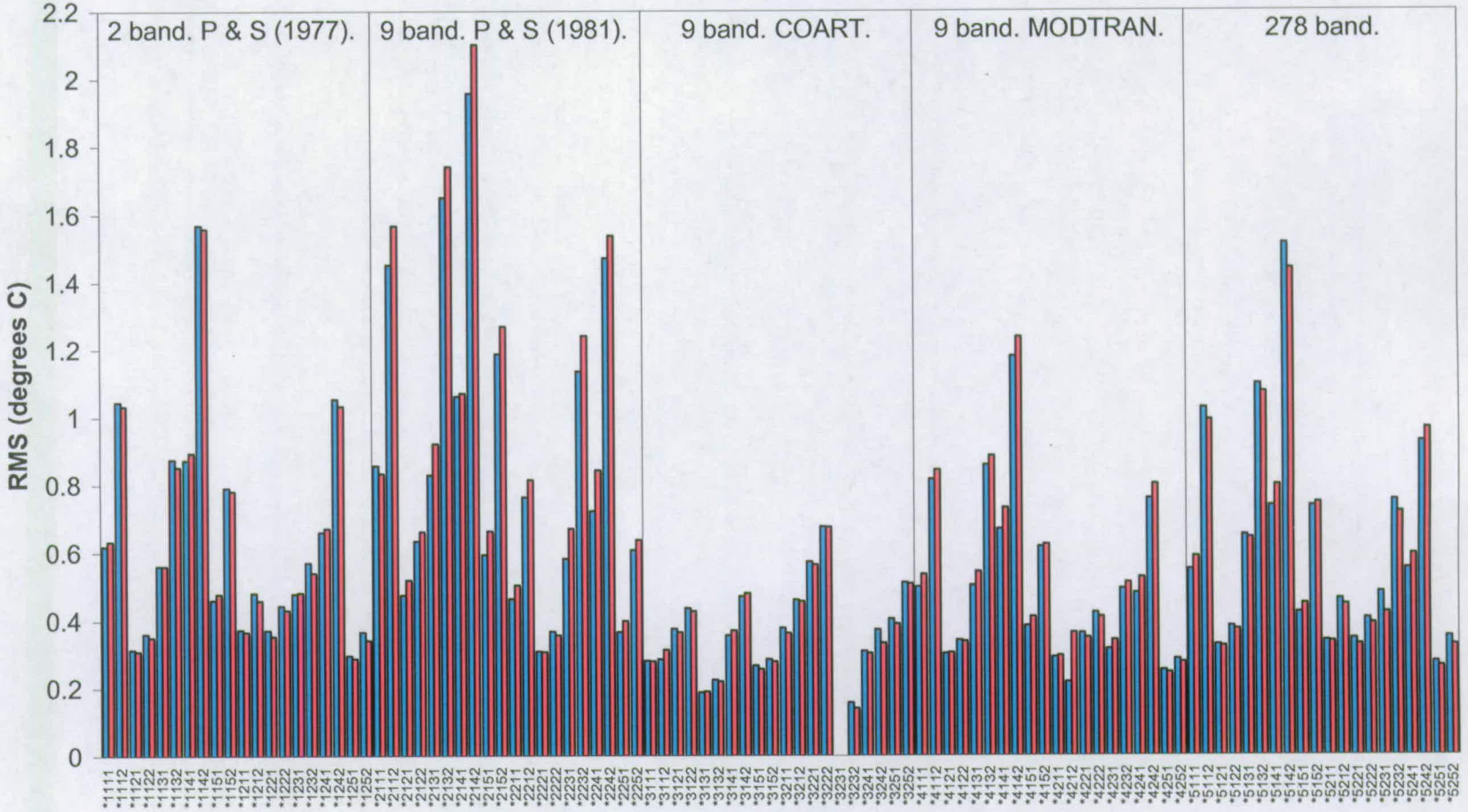

Figure 4.4 Averaged across the three data sets, these are the RMS of residuals of temperature at the top sensor for all option-set combinations. The x-axis labels are codes (defined in Table 4.1) for the combinations. The asterisk replaces the first number of the code as a 'wild-card'. Blue bars represent a '1' and red bars a '2'. It is not essential to refer to the codes. The comparison to make here is between M-Y (blue) and k-e (red) options, regardless of the combinations of the other option-sets

Diurnal variations in temperature generally decrease with depth. It is more difficult to model diurnal variation of temperature close to the surface of the ocean than at several metres depth. A good test of model skill then is to examine the residuals for the shallowest sensor depths. A quick look at the RMS of the residuals of SST for the shallowest temperature sensor reveals that similar values are obtained for each of the turbulence closure models.

RMS of temperature residuals for the shallowest sensor for each combination, averaged across the three data sets, are shown in Figure 4.4. The five radiation distributions are also labelled but analysis of option-sets other than the turbulence model option is not intended at this stage. In this chart, most of the combinations that include the MY type model (blue bars) give lower RMS residuals of SST than corresponding combinations that include the k-e type model (red bars). This might suggest that the MY type model performs better than the k-e type in predicting SST at the shallowest sensor. However, for the lowest RMS values, kappa-epsilon performs slightly better overall. This is shown by the statistical analysis below.

The combination(s) with low RMS will be selected as the way to run GOTM. For each property, defined in Table 4.4, the mean of the ten best performing combinations (lowest RMS of residuals) was calculated and appears in Table 4.5 for both the Mellor-Yamada type and Kappa-epsilon models. Although the performance advantage is small, it is clear in that, when the RMS of residuals are low, the kappa-epsilon model performs better than Mellor-Yamada for all data sets and all properties given in Table 4.5.

RMS of property °C	RMS of residuals by data set					
	COARE		Lotus		Arabian Sea	
	MY	KE	MY	KE	MY	KE
SST at all times, top sensor	0.315	0.309	0.314	0.300	0.169	0.161
SST at all times, mean depth to 5 m	0.217	0.216	0.327	0.319	0.149	0.146
Diurnal amplitude, top sensor	0.555	0.506	0.266	0.199	0.263	0.236
Diurnal amplitude, mean depth to 5 m	0.410	0.388	0.528	0.502	0.251	0.243
Stratification	0.319	0.313	0.312	0.298	0.243	0.241

Table 4.5 Comparison of the mean of the lowest 10 RMS of residuals of various properties for each of the turbulence mixing options: MY type and k-e.

Eliminating the Mellor-Yamada option immediately reduces the number of combinations by half. The Mellor-Yamada closure model is excluded from further analysis with confidence that the kappa-epsilon model will perform no worse than Mellor-Yamada for low RMS combinations and possibly slightly better.

Burchard et al (1998) also found that the Mellor-Yamada and kappa epsilon models performed in a similar way to each other in their experiments on mixed and stratified water columns. They conclude that the choice of stability functions have a stronger influence than the choice of length scale related equation (MY and k-e are length scale related equations, see chapter 2). However, their performance testing properties and their test case data sets differ from those presented here, thereby warranting the inclusion of these choices in this sensitivity test.

4.6 Option set 3, Longwave radiation

In chapter 3, various ways of determining the net longwave-radiation were described. The two options are the Clark (1974) formula (the GOTM air-sea module default) and the Brunt type formula with Grant and Hignett (1998) coefficients, hereafter referred to as Brunt type (G&H, 1998).

Figure 4.5 shows a pair-wise comparison of option-set 3 with the RMS of SST residuals for each combination at the depth of the top sensor for each data set. A first look at this data reveals that for most of the remaining combinations, the Brunt type (G&H, 1998) formula performs better than the Clark (1974) formula. The pair-wise combinations are sorted in descending order of RMS of residuals of top sensor SST for combinations with the Brunt type (G&H, 1998) formula.

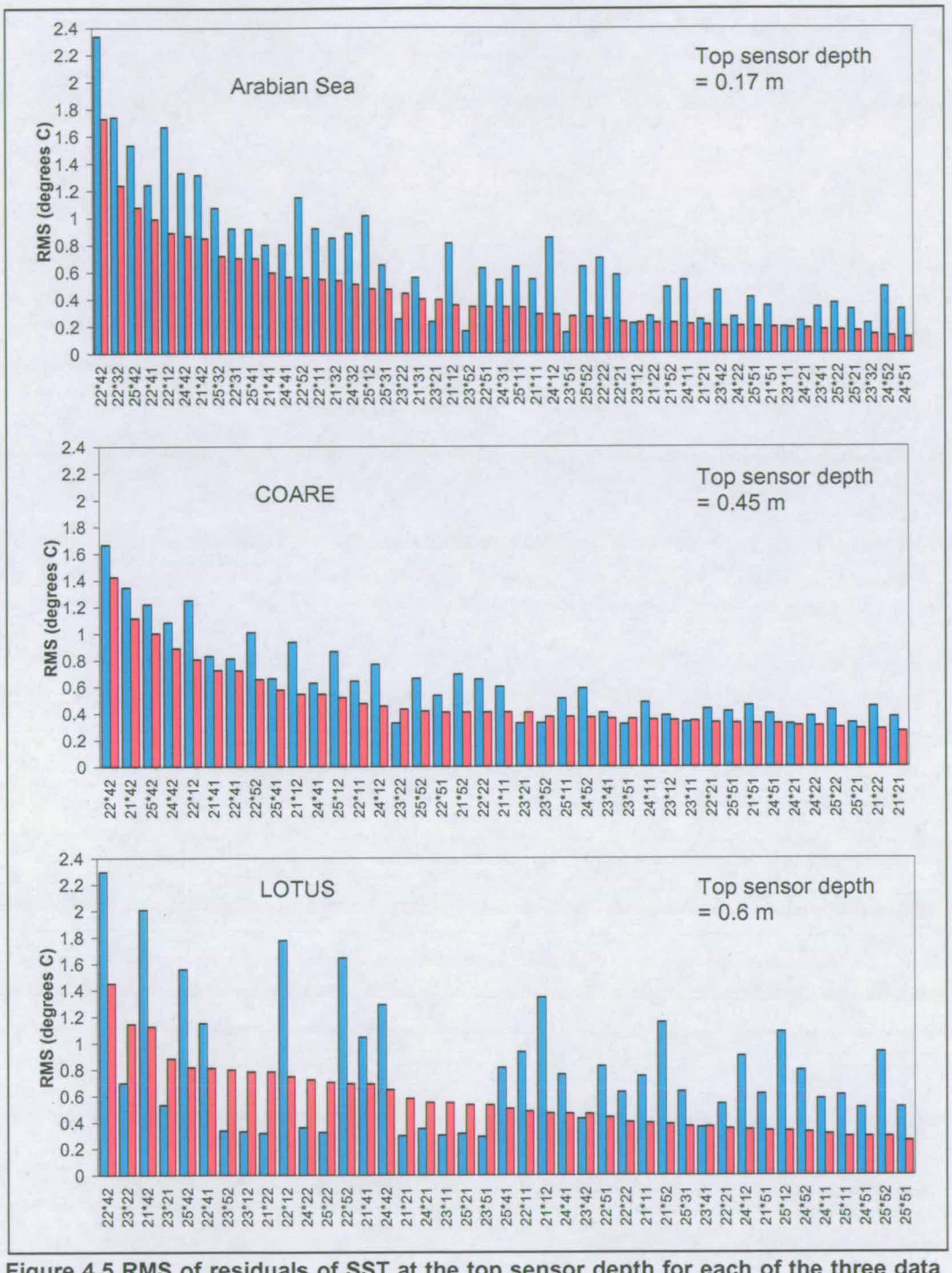

Figure 4.5 RMS of residuals of SST at the top sensor depth for each of the three data sets. For DLR calculations (the 3rd option-set) the blue bars indicate that the Clark (1974) formula was used and the red bars that the Brunt type formula of Grant and Hignett (1998) was used. Combinations are only shown that include the KE turbulence model from the 1st option-set, the MY option having already been eliminated.

4.6.1 A note on model stability for some combinations

Note that the combinations labelled on the x-axes of the charts in Figure 4.5 are not necessarily in the same order on each chart, i.e. the order differs between data sets. There are more combinations on the Arabian Sea chart. This is because not all combinations when run in the model proved stable enough to continue to the end of the tenth day. The stability issue of some combinations varied with each data set and the combinations were retained because it was not known whether the problem was related to some erroneous data, a coding error or something more fundamental. Therefore, combinations that are not stable with one dataset but stable with another are still shown on the chart of the stable dataset.

4.6.2 Lowest 10 RMS of residuals of various properties

For each property, defined in Table 4.4, the mean of the ten best performing combinations (lowest RMS of residuals) was calculated and appears in Table 4.6 for both the Clark (1974) and Brunt type (G&H, 1988) formulae. Although the performance advantage is small, it is clear that when the RMS of residuals are low, the Brunt type formula performs better than Clark (1974) for all data sets and all properties given in Table 4.6 (except for the property labelled: 'diurnal amplitude, mean depth to 5m' for the COARE data set).

RMS of property °C	RMS of residuals by data set					
	COARE		Lotus		Arabian Sea	
	Clark (1974)	Brunt (G&H, 1998)	Clark (1974)	Brunt (G&H, 1998)	Clark (1974)	Brunt (G&H, 1998)
SST at all times, top sensor	0.345	0.307	0.326	0.317	0.222	0.168
SST at all times, mean depth to 5 m	0.259	0.215	0.352	0.322	0.259	0.214
Diurnal amplitude, top sensor	0.563	0.562	0.256	0.210	0.265	0.244
Diurnal amplitude, mean depth to 5 m	0.396	0.405	0.513	0.507	0.251	0.250
Stratification	0.351	0.317	0.323	0.314	0.282	0.241

Table 4.6 Comparison of the mean of the lowest 10 RMS of residuals of various properties for each of the longwave radiation options: Clark (1974) and Brunt type (G&H, 1998).

4.6.3 Detailed observations

The charts show that in general and with all else being equal, the top-sensor SSTs are more accurately modelled using the Brunt type (G&H, 1998) formula in option-set 3. There are some exceptions to this general observation. For the Arabian Sea data set and the COARE data set, the Clark (1974) formula is sometimes (but not always) better when the COART option in option-set 2 is also selected. For the LOTUS data set, the Clark formula is better in *all* combinations when the COART option in option-set 2 is also selected.

The forms of the two longwave radiation parameterisations compared here are described in Section 3.3. The net-longwave radiation is not a body source of heat, it is a flux that enters or leaves at the surface. It is therefore expected to affect temperatures near the surface and it is appropriate to examine the relative effect of each parameterisation on the temperature at the shallowest sensor depth for each data set.

With the LOTUS data set, some combinations that incorporate the Clark (1974) formula perform better than Brunt type (G&H, 1998) when the Kondo (1975) and Smith (1988) option (code 2) is also selected in option-set 4. Smith's wind-measurement-height conversion-tables (1988) were used in conjunction with the Kondo (1975) flux parameterisations to improve estimates of momentum flux in non-neutrally stratified atmospheric conditions. However, the parameterisations were derived independently of each other and their combination may not be the most physically based solution. The Kondo (1975) / Smith (1988) option gives rise to the greatest momentum flux and therefore the most mixing. Modelled SSTs that are too high could be mitigated then by more mixing with this option, cf. 'equifinality'. Too much mixing in the model would adversely affect prediction of SST at other depths and therefore adversely affect stratification.

Figure 4.6 shows a pair-wise comparison of the mean modelled temperatures of the shallowest sensor for each ten day run for each data set.

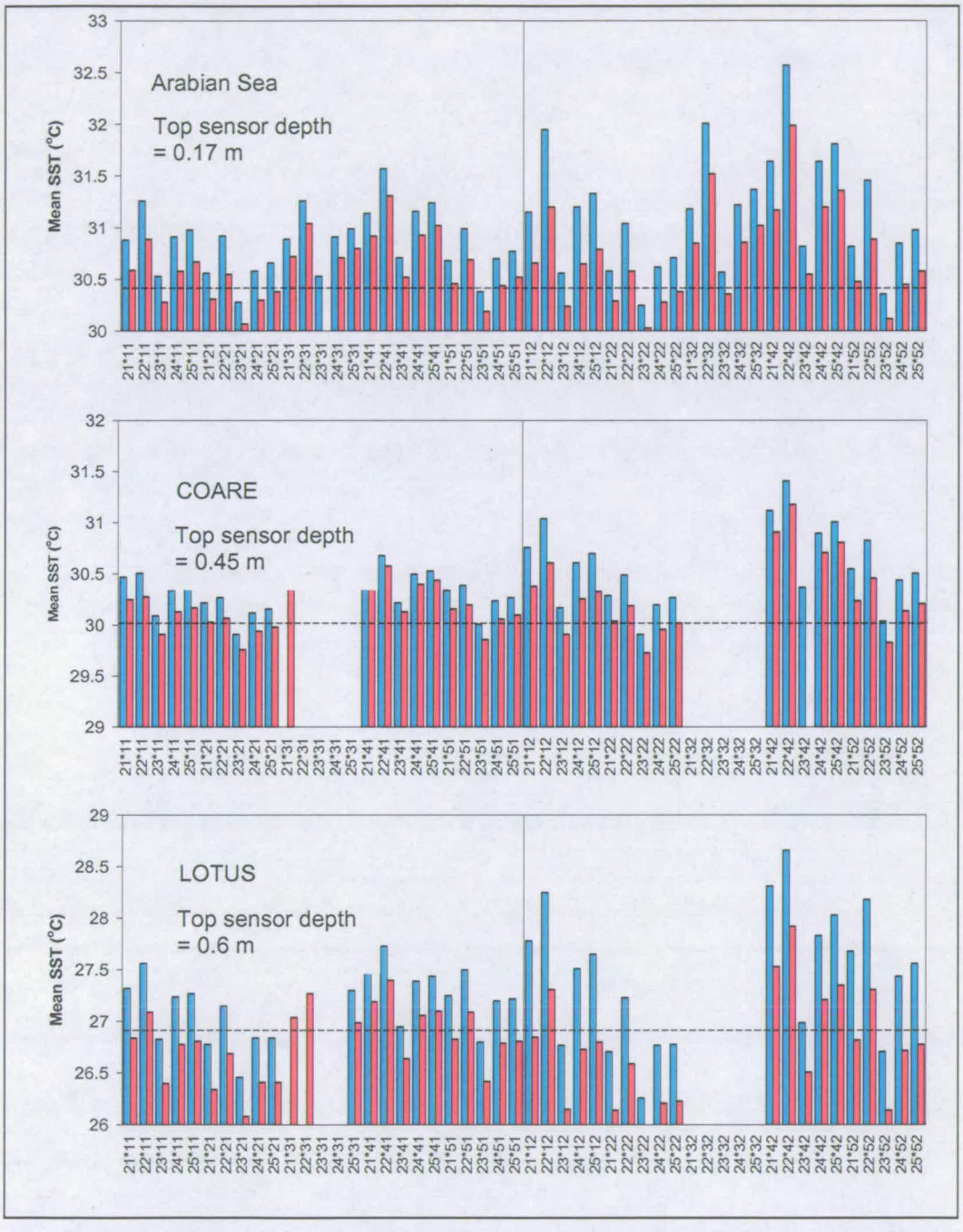

Figure 4.6 Comparison of mean modelled SST to mean observed SST for each 10 day model run. The observed mean SSTs are shown for each data set by the dashed lines. The blue bars = the Clark (1974) formula and the red bars = the Brunt type formula of Grant and Hignett (1998).

For many combinations, the mean of modelled SSTs differs from the observed mean SST. This could mean that the modelled SSTs drift away from the observed SSTs over the 10 day period of the model simulation. Another possibility is that modelled diurnal amplitudes of SST differ from observed diurnal amplitudes.

From the charts in Figure 4.6 it is clear that all combinations incorporating the Clark (1974) parameterisation produce higher mean modelled SSTs than equivalent combinations that incorporate the Brunt type (G&H 1998) formula.

For most of the combinations that include the COART option from option-set 2 and/or the Kondo (1975) / Smith (1988) option from option-set 4, the mean modelled SST is lower than the mean observed SST.

All else being equal, the Clark (1974) formula predicts more downwelling longwave radiation and therefore less net longwave radiation leaving the ocean than the Brunt type (G&H 1998) formula. This compensates for heat differences arising as a consequence of choices in option-sets 2 and 4. In option-set 2, the COART radiation distribution models the deposition of heat such that the near surface receives less energy than it would with any of the other distributions. The Kondo / Smith option results in greater mixing in the model through higher momentum flux than that modelled by any of the other options in option-set 4.

There is some variation of the degree of mixing between combinations. Having eliminated the MY model from option-set 1, the degree of mixing is now dependent only on the choice of option-set 4. The degree of mixing can influence overall drift of SST in the model. The deep water column of the ocean acts as a large sink for heat. Therefore, as heat absorbed near the surface during the day is mixed downwards, the SST is partly 'restored'

towards a value consistent with the initial heat content. The initial heat content is the same for observations and model.

4.7 Option-set 5: Pre-calculated fluxes versus interactively calculated fluxes

With this option-set, the ocean leaving fluxes are either pre-calculated, using the observed SST from the shallowest sensor for each data set, or interactively calculated, using the modelled SST at the air-sea interface. There are advantages and disadvantages to either approach.

The ocean-leaving fluxes are dependent on SST at the air-sea interface but observed SST is not usually measured exactly at the interface (the shallowest LOTUS temperature sensor is at 0.6 m). Any significant stratification present near the surface implies that the interface temperature will differ from the shallowest sensor depth and the ocean-leaving fluxes will likely be underestimated by the model under conditions of strong sea-surface warming.

Interactively modelled ocean-leaving fluxes are calculated with modelled SST from the shallowest model layer 0.005 m – essentially the interface, (not including the cool skin effect at this stage). When the shallowest sensor SST and the surface stratification are well predicted, this method will likely give more accurate ocean-leaving fluxes and is more physically correct. However, caution is warranted because the stabilising feedback of this method, as described in chapter 3, could mask otherwise poor combinations of options from other option-sets.

The SST dependent parameterisations used to calculate the ocean-leaving fluxes at each time-step are given in the 4th option-set, see Table 4.1 and Chapter 3.

Model combinations with pre-calculated fluxes (using observed SST) are compared to their pair-wise counterparts with interactively calculated fluxes (using modelled SST). By comparison of RMS of residuals, Figure 4.7 to Figure 4.10 illustrate the comparative skill in modelling SST and diurnal amplitude at the shallowest sensor and stratification and SST to 5 m.

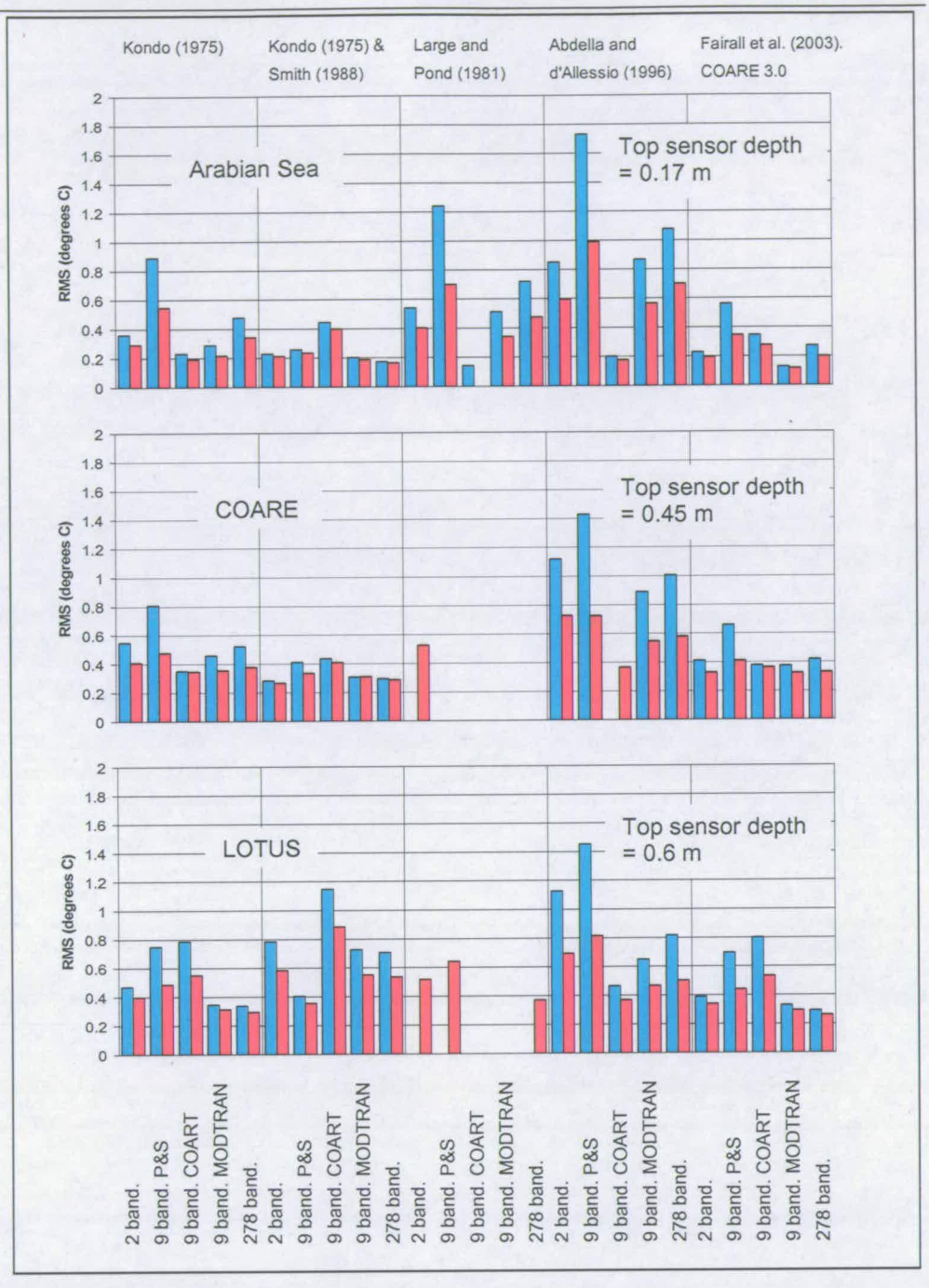

Figure 4.7 RMS of residuals of SST at the top sensor depth for each of the three data sets. For non-solar heat-flux calculations (the 5th option-set) the blue bars indicate that observed SST was used and the red bars that modelled SST was used. The options of the 2nd option-set are labelled below the charts. The options of the 4th option-set are labelled above the charts. Combinations are only shown that include the *k*-ε turbulence model from the 1st option-set and the Brunt type parameterisation of DLR from the 3rd option-set, the other options having been eliminated.

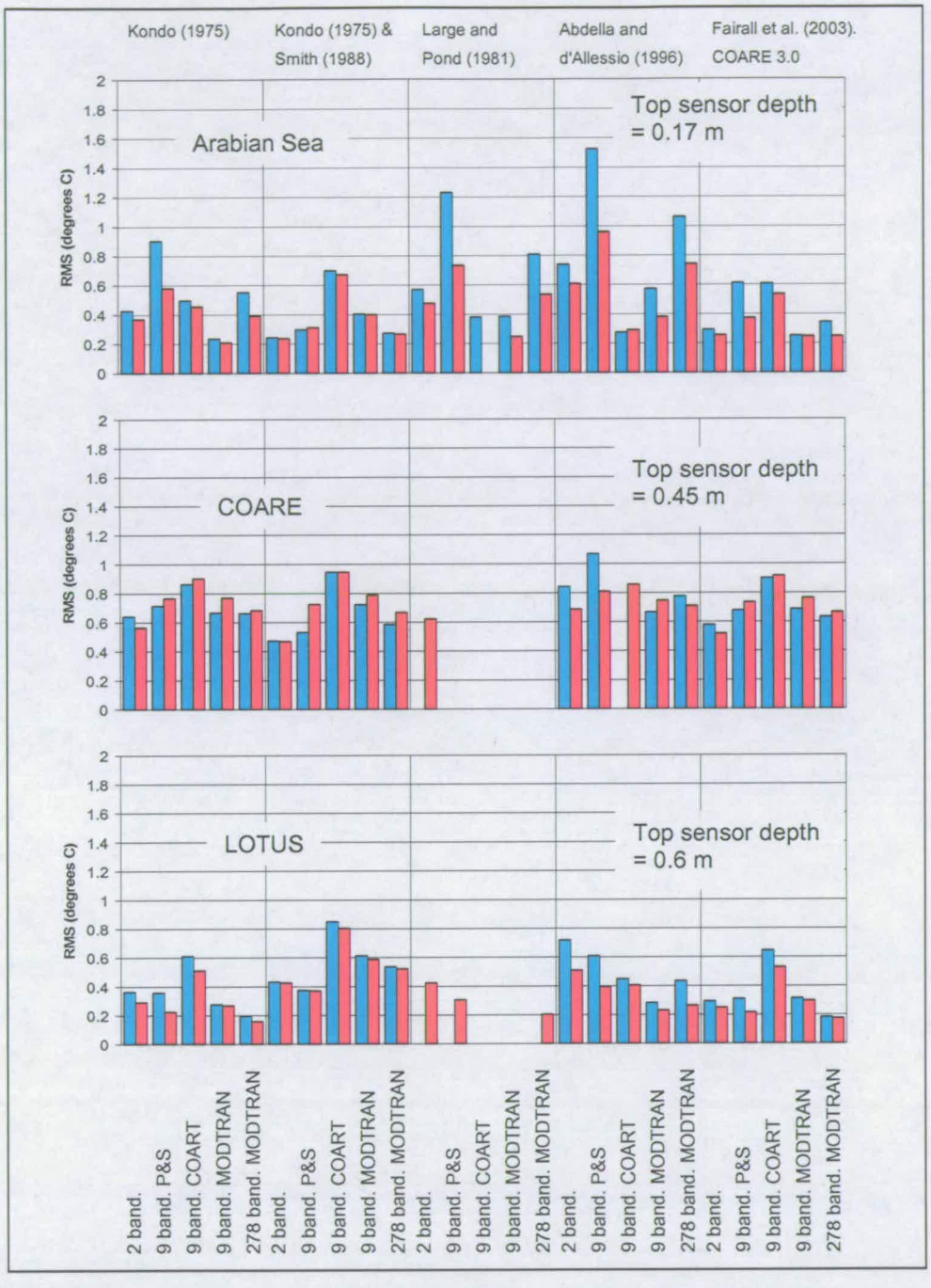

Figure 4.8 RMS of residuals of diurnal amplitude of SST at the top sensor depth for each of the data sets. For non-solar heat-flux calculations (the 5th option-set) the blue bars indicate that observed SST was used and the red bars that modelled SST was used. The options of the 2nd option-set are labelled below the charts and the options of the 4th option-set are labelled above. Combinations are only shown that include the KE turbulence model from the 1st option-set and the Brunt type parameterisation of DLR from the 3rd option-set, the other options having been eliminated.

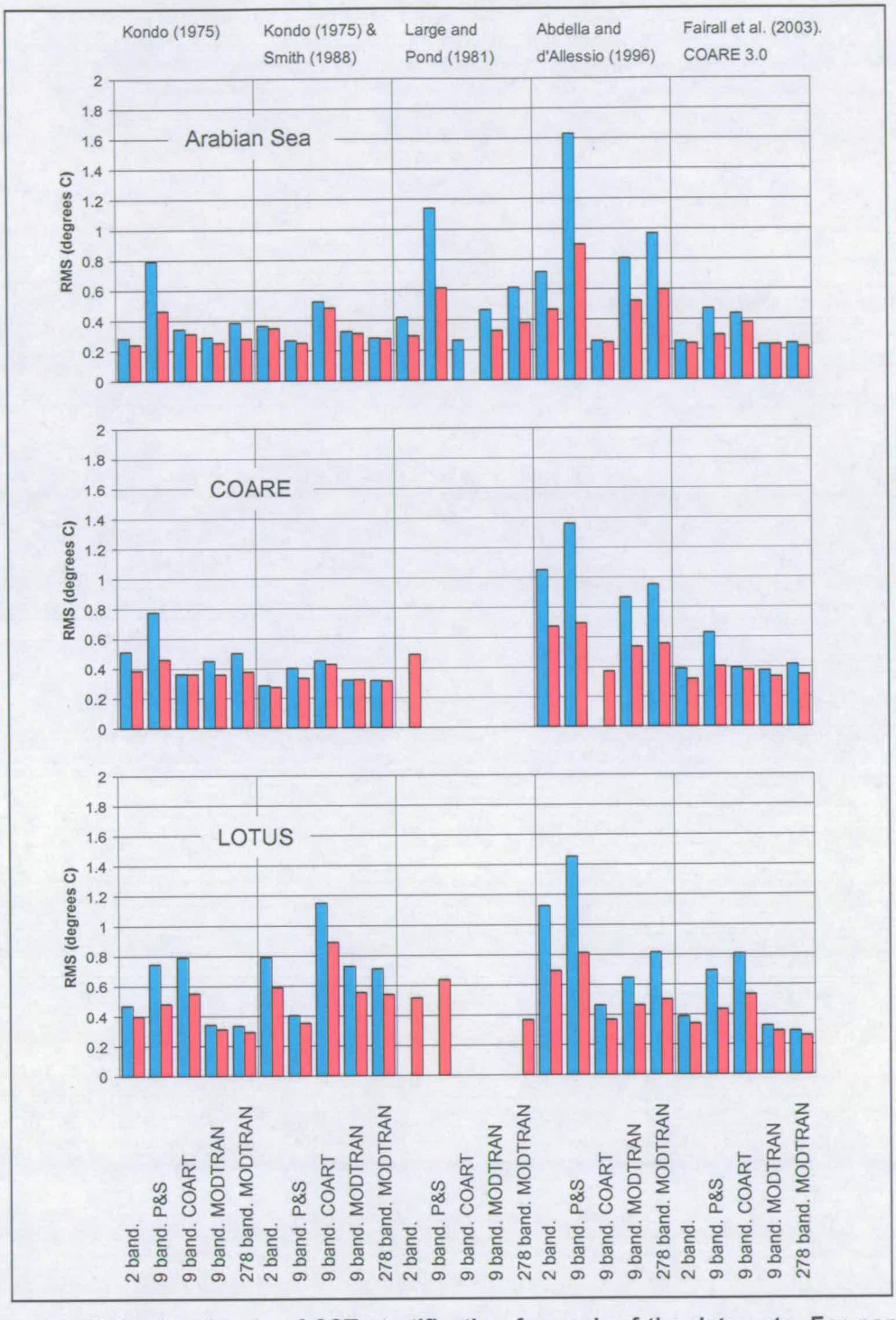

Figure 4.9 RMS of residuals of SST stratification for each of the data sets. For non-solar heat-flux calculations (the 5th option-set) the blue bars indicate that observed SST was used and the red bars that modelled SST was used. The options of the 2nd option-set are labelled below the charts and the options of the 4th option-set are labelled above. Combinations are only shown that include the KE turbulence model from the 1st option-set and the Brunt type parameterisation of DLR from the 3rd option-set, the other options having been eliminated.

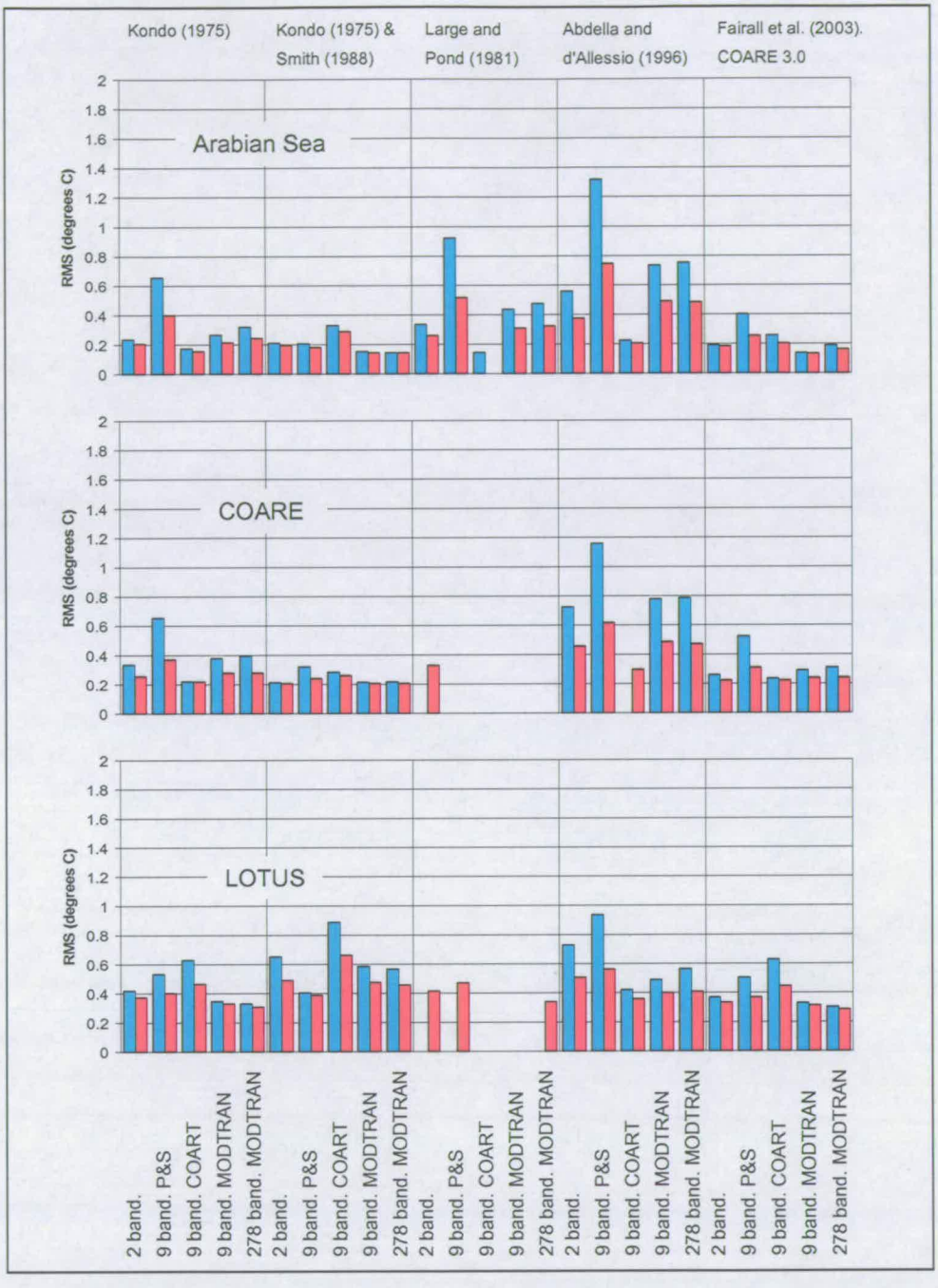

Figure 4.10 Mean of the RMS of residuals of SST at each sensor depth to 5 m for each of the data sets. For non-solar heat-flux calculations (the 5th option-set) the blue bars indicate that observed SST was used and the red bars that modelled SST was used. The options of the 2nd option-set are labelled below the charts and the options of the 4th option-set are labelled above. Combinations are only shown that include the *k-ε* turbulence model from the 1st option-set and the Brunt type parameterisation of DLR from the 3rd option-set, the other options having been eliminated.

4.7.1 Analysis by RMS of residuals comparison.

As noted in the previous Section, some combinations are missing from the charts and this is examined in the next Section. Setting aside those combinations that are not paired, i.e. red or blue missing in the charts of Figure 4.5, I continue with the analysis of this option set with the remaining combinations.

RMS residuals of SST at the shallowest temperature sensor (Figure 4.7) are lower for the option with interactive fluxes (i.e. fluxes calculated from modelled interface SSTs). This is true for all remaining combinations and all three data sets.

For runs with the Arabian Sea and LOTUS data sets, there are no combinations with pre-calculated fluxes that give lower RMS residuals for diurnal amplitude (Figure 4.8) than corresponding combinations with interactively calculated fluxes. For runs with the COARE data set, the diurnal amplitude results are less conclusive.

The RMS of the residuals of stratification (Figure 4.9) indicate that for all of the data sets, stratification is predicted better by combinations with interactively calculated fluxes than all corresponding combinations with pre-calculated fluxes. The same is true for the mean of the RMS of residuals of SST at each sensor depth to 5 m (Figure 4.10).

4.8 Option set 4 Non – radiative flux calculation from meteorology, including wind stress

Now that many combinations have been eliminated, it is clear that the Large and Pond (1981) option from option-set 4 is failing for many of the combinations that are run with the COARE and LOTUS data sets. It does

work, however, for most of the combinations that are run with the Arabian Sea data. With the COART option for solar-radiation distribution (option-set 2) and pre-calculated fluxes, the SST at 0.17 m is well modelled. Had this been the only analysis, it might have been concluded that this was the way to run GOTM. However, the extent and detail of the analysis carried out here shows that this option lacks stability at other locations and less skill at modelling diurnal amplitude and stratification than some other combinations. This illustrates the importance of
this extensive sensitivity study. Large and Pond (1981) is eliminated here then because combinations including this option do not have model stability at all locations (at least when implemented in GOTM).

The options of this option-set are grouped together and labelled at the top of Figure 4.7 to Figure 4.10. From Figure 4.7 (RMS residuals of SST at shallowest sensor) the Abdella and d'Allessio option fairs worst overall when all of the data sets are considered. With the COART option for solar-radiation distribution (option-set 2), Abdella and d'Allessio is competitive with some of the best combinations (especially within this group (i.e. when COART selected)). This is true also of diurnal amplitude, stratification and temperature to 5m. Some insight can be gained by examining how COART performs within each option of this option-set. For Kondo (1975), Kondo (1975) and Smith (1988) and the Fairall et al. (2003) options, COART is one of the worst options of option-set 2, when predicting diurnal amplitude. Combinations that incorporate this option are also poor at stratification prediction and SST predicting performance is variable across data sets. Another problem is that when fluxes are precalculated, any combination incorporating both COART and Abdella and d'Allessio (2003) fails to complete for runs on the COARE data set. It can either be concluded that combinations incorporating Abdella and d'Allessio (2003) and the COART option are the best performers and the best way to run GOTM and that all the other non-radiative flux calculation parameterisations perform less well or that COART is compensating for the

poorer performance of Abdella and d'Allessio (2003), cf. equifinality. The latter is more likely .

Of the remaining three options in this option-set, the Fairall *et al.* (2003), COARE 3.0 option delivers the most consistency for skill at predicting all of the properties described in Table 4.4, across all three data sets, see Table 4.7. Recall that the COARE 3.0 option is coded in option set 4 by the number 5. In Table 4.7, the codes with the lowest RMS of residuals are tabulated for the four properties described in Table 4.4. The frequencies of each option in option set 4 occurring in Table 4.7 for each property are tabulated in Table 4.8. COARE 3.0 occurs more frequently than any other option for all 4 properties. Therefore, the COARE 3.0 algorithm will be chosen for calculating non-radiative fluxes from meteorological parameters.

Property	Arabian		COARE		LOTUS	
	Code	RMS (°C)	Code	RMS (°C)	Code	RMS (°C)
SST at top sensor depth	24252	0.12	21222	0.27	25252	0.26
	25222	0.17	25222	0.29	24252	0.30
	23242	0.18	24252	0.32	25212	0.30
	24222	0.19	21252	0.33	24212	0.32
	23212	0.19	25252	0.33	21252	0.34
Diurnal amplitude at top sensor depth	24212	0.21	21222	0.47	25212	0.16
	21222	0.24	21252	0.52	25252	0.17
	25252	0.25	21212	0.56	25232	0.20
	24252	0.25	21232	0.62	22252	0.22
	24232	0.25	25252	0.67	22212	0.23
Stratification	25252	0.22	21222	0.27	25252	0.26
	24252	0.23	25222	0.29	24252	0.29
	21252	0.24	24252	0.33	25212	0.29
	21212	0.24	21252	0.33	24212	0.31
	23242	0.25	25252	0.33	21252	0.34
SST at mean depth to 5 m.	24252	0.13	21222	0.21	25252	0.29
	25222	0.14	25222	0.21	25212	0.31
	24222	0.14	23212	0.22	24252	0.31
	23212	0.15	21252	0.22	24212	0.33
	25252	0.16	23252	0.22	21252	0.34

Table 4.7 Lowest five RMS of residuals of four properties (with combination codes).

Code (Option set 4):	1	2	3	4	5
Property					
SST at top sensor depth	3	4	0	1	7
Diurnal amplitude at top sensor depth	4	2	3	0	6
Stratification	3	2	0	1	9
SST at mean depth to 5 m.	4	4	0	0	7
Total	14	12	3	2	29

Table 4. 8 Frequency of options from option set 4 occurring in Table 4.7.

4.9 Option-set 2 - Short wave radiation parameterisation

For the remaining combinations, refer to the fifth column in Figure 4.7 to Figure 4.10, under the heading Fairall et al. (2003), COARE 3.0. In Figure 4.7, 'SST at the top sensor', the 9 band MODTRAN and 278 band MODTRAN options are better overall. The 9 band MODTRAN and 278 band MODTRAN options are also better in Figure 4.9, 'stratification', and Figure 4.10, 'mean of the RMS of residuals of SST at each sensor depth to 5 m'. Only in Figure 4.8, 'diurnal amplitude' is there a better option (2 band) and only for the COARE data set. These results are tabulated in Table 4.9. The 9 band MODTRAN option (code number 4) occurs 4 times as the best option (lowest RMS residual) and the 278 band option occurs 6 times as the best option see Table 4.9.

The 278 band option was optimised in the model so that calculation of the SSI distribution in the water column is only required at the times when new SSI observations are available (i.e. the SSI forcing data resolution). At each model timestep between SSI observations, the distribution of the SSI is linearly interpolated. However, a 9 band parameterisation is probably sufficient for most users of GOTM. The band proportion coefficients are clearly a very important consideration.

Property	Arabian		COARE		LOTUS	
	Code	RMS (°C)	Code	RMS (°C)	Code	RMS (°C)
SST at top sensor depth	24251	0.12	24251	0.32	25251	0.26
	25251	0.20	25251	0.33	24251	0.29
	21251	0.20	21251	0.33	21251	0.34
	23251	0.28	23251	0.36	22251	0.44
	22251	0.35	22251	0.41	23251	0.53
Diurnal amplitude at top sensor depth	25251	0.25	21251	0.52	25251	0.17
	24251	0.25	25251	0.67	22251	0.22
	21251	0.26	22251	0.73	21251	0.25
	22251	0.37	24251	0.76	24251	0.30
	23251	0.54	23251	0.92	23251	0.53
Stratification	25251	0.22	24251	0.33	25251	0.26
	24251	0.23	21251	0.33	24251	0.29
	21251	0.24	25251	0.33	21251	0.34
	22251	0.30	23251	0.37	22251	0.44
	23251	0.38	22251	0.41	23251	0.53
SST at mean depth to 5 m.	24251	0.13	21251	0.22	25251	0.29
	25251	0.16	23251	0.22	24251	0.31
	21251	0.19	24251	0.24	21251	0.34
	23251	0.20	25251	0.24	22251	0.37
	22251	0.26	22251	0.31	23251	0.45

Table 4.9 RMS of residuals for option-set 2 of four properties (with combination codes).

In this option set, the improvement in the RMS of residuals of modelled SST with new SSI fractions over the 9 band P&S (1981) SSI fractions, is as much as 0.2 K for top sensor SST and diurnal amplitude and 0.1 K improvement for stratification (with all else being equal), see the fifth column in Figure 4.7 to Figure 4.10 and Table 4.9.

4.10 Time series comparisons of original and improved models

Figure 4.11 to Figure 4.13 show the time series of SST at the top sensor and at 5 m for the 10 day runs of each data set. The first (top) plot in each figure is the combination with the best air-sea and radiation distribution options available in GOTM, before new options were added to allow the 200 combinations described in chapters 3 and 4. The second (bottom) plot in each figure is the best combination available in the modified model according to the analysis presented in this chapter.

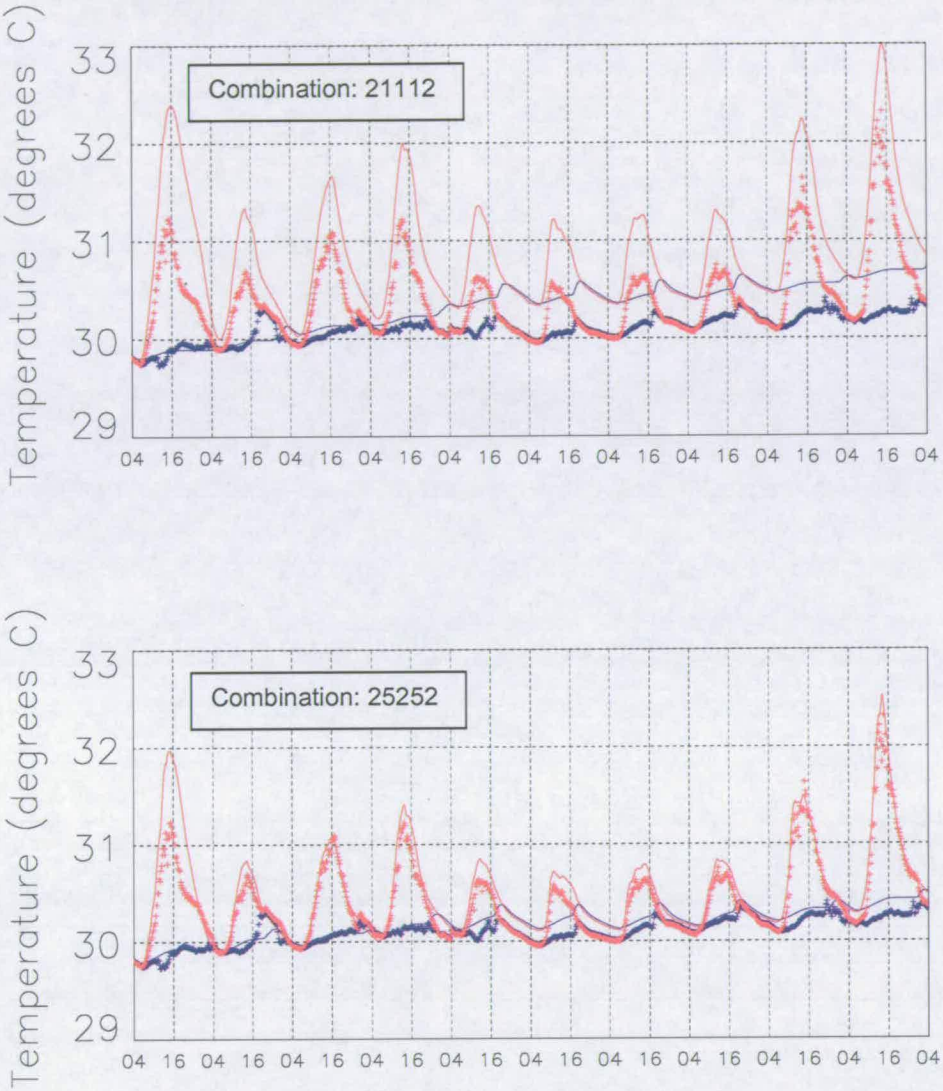

Figure 4.11 Arabian Sea 10 day model run. Comparison of modelled SST at top sensor (0.17 m) and at 5 m using original (public domain version) options (top) and best of the combinations of added and original options (bottom).

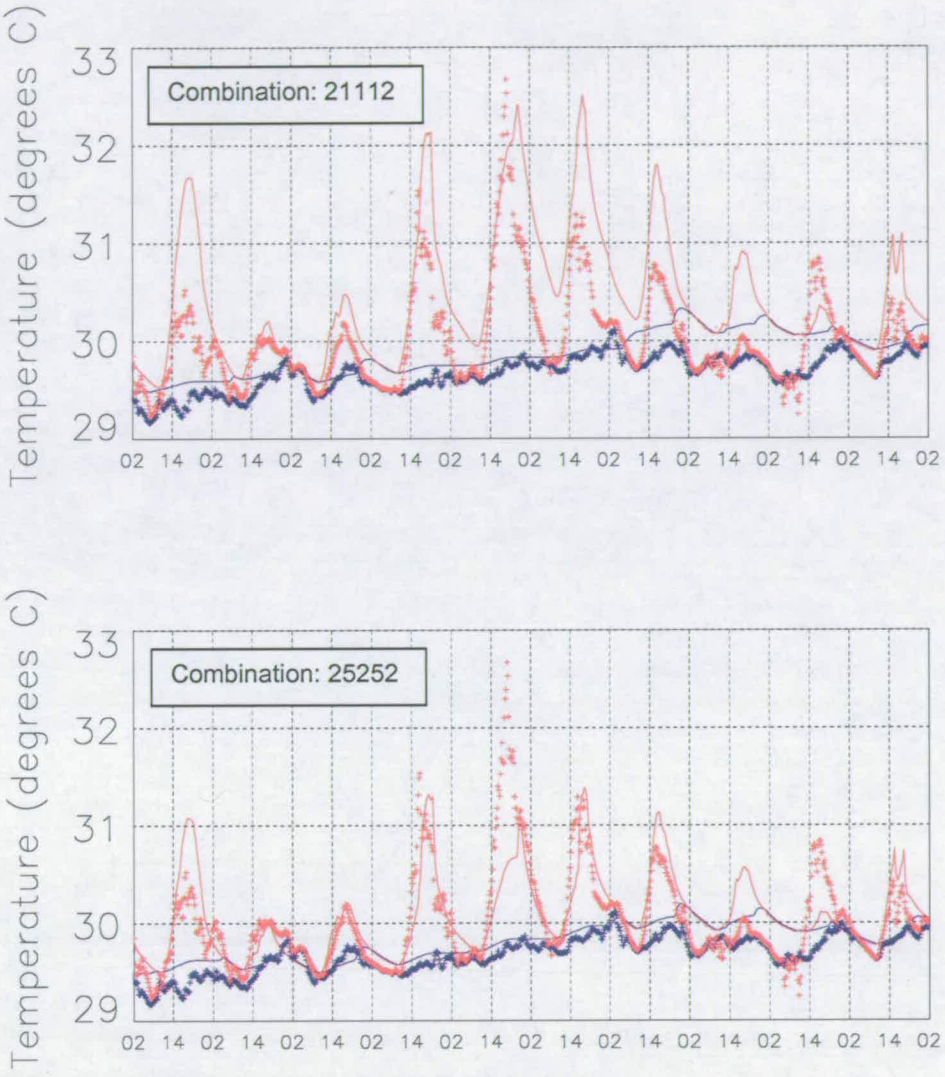

Figure 4.12 COARE 10 day model run. Comparison of modelled SST at top sensor (0.45 m) and at 5 m using original (public domain version) options (top) and best of the combinations of added and original options (bottom).

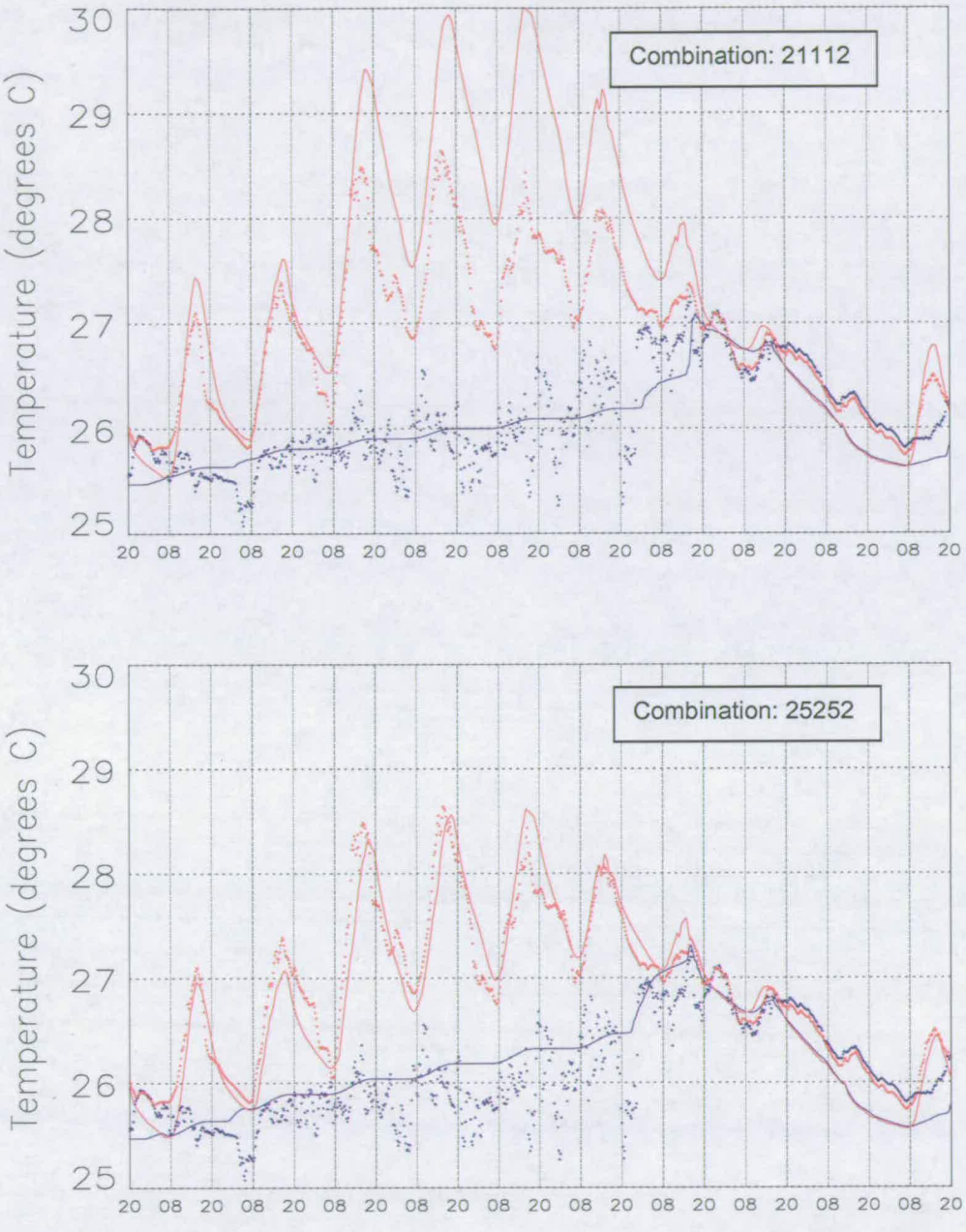

Figure 4.13 LOTUS 10 day model run. Comparison of modelled SST at top sensor (0.6 m) and at 5 m using original (public domain version) options (top) and best of the combinations of added and original options (bottom).

In Figure 4.11 to Figure 4.13, the improvement in top sensor SST prediction is clear for all data sets. With the original model configuration, the SST at the shallowest sensor was incorrectly modelled by more than a degree on days with large diurnal amplitudes. With the new model configuration, shallowest sensor SSTs are modelled to within a few tenths of a degree for most of the days simulated. Improvements in diurnal amplitude prediction and surface stratification can also be seen. The plots from each data set are described in a little more detail below.

Arabian Sea

For each day of the original model simulation, the daily maximum SST at the shallowest sensor (0.17 m) exceeds the observed SST at this depth by at least ½ a degree. The 5 m SST is well modelled for the first four days and then drifts from the observed temperature at 5 m. The diurnal amplitude of the 0.17 m SST is over predicted by about 1/3 to 1/2 of a degree for most of the days. Too much stratification occurs with the original model. This is most likely explained by a combination of incorrect solar distribution and incorrect shear stress.

The new model, apart from the first day, predicts 5 m and 0.17 m SST within a few tenths of a degree for most of the simulation period. This would suggest better definition of solar radiation distribution and prescription of wind induced shear.

COARE

For this data set the original model also over estimates shallowest sensor SST (0.45 m) for most of the days of the simulation. The observed 5 m SST exhibits variations with period of about 6 hours that could be attributed to internal waves. The amplitude of the variations is quite small in this data set. Neither the new or original models can simulate variations caused by internal waves but the 5 m trend is reasonably well predicted by both new and original

models. The diurnal amplitude of the 0.45 m SST and surface stratification is better predicted by the new model for most of the simulation period.

LOTUS

For this data set the original model also over estimates shallowest sensor SST (0.45 m), diurnal amplitude and stratification for most of the days of the simulation. Internal wave activity is also observed in the 5 m SST observations with amplitudes that sometimes exceed one degree with period of about 6 hours. The 0.45 m SST, diurnal amplitude and surface stratification are well predicted by the new model for the first 7 days of the simulation period.

4.10.1 Statistical comparisons of original and improved models.

In Table 4.10, the RMS of residuals of the three key properties of diurnal variation of SST are given. The two best combinations show better performance for all properties and all data sets except for diurnal amplitude in the COARE data set.

Property	Code	Arabian	COARE	LOTUS	Mean over 3 data sets
SST at top sensor depth	21112	0.55	0.60	0.75	0.63
	24252	0.12	0.32	0.30	0.25
	25252	0.20	0.33	0.26	0.26
Diurnal amplitude at top sensor depth	21112	0.51	0.61	0.42	0.51
	24252	0.25	0.75	0.30	0.43
	25252	0.25	0.67	0.17	0.36
Stratification	21112	0.44	0.60	0.75	0.60
	24252	0.22	0.32	0.29	0.28
	25252	0.24	0.33	0.26	0.28

Table 4.10 Comparison, by RMS of residuals (°C) of three properties, of original (public domain version) and best two combinations of the enhanced model.

The main problem for the new model with the COARE data set appears to be on day 5. With this day removed from the statistical calculations, the diurnal amplitude RMS residuals at top sensor depth are: 0.60 for 21112, 0.61 for 24252 and 0.49 for 25252.

4.11 Validation data sets

The best model setup has been found by carrying out many simulations with three data sets. This best setup of the enhanced model is now independently validated with two independent data sets. These data sets are independent in time from the data sets used to calibrate the model but the locations are the same as the calibration data sets.

The two data sets are: the Arabian Sea (15^{O} N 61^{O} E, 19^{th} February 1995 to 1st March 1995) and COARE (2^{O} S 156^{O} E, 7^{th} January 1993 to 17^{th} January 1993).

Figure 4.14 and Figure 4.15 show the time series of SST at the top sensor and at 5 m for the simulations with the validation data set. The first (top) plot in each figure is the combination with the best air-sea and radiation distribution options available in GOTM, before new options were added to allow the 200 combinations described in chapters 3 and 4. The second (bottom) plot in each figure is the best combination available in the modified model according to the analysis presented in this chapter.

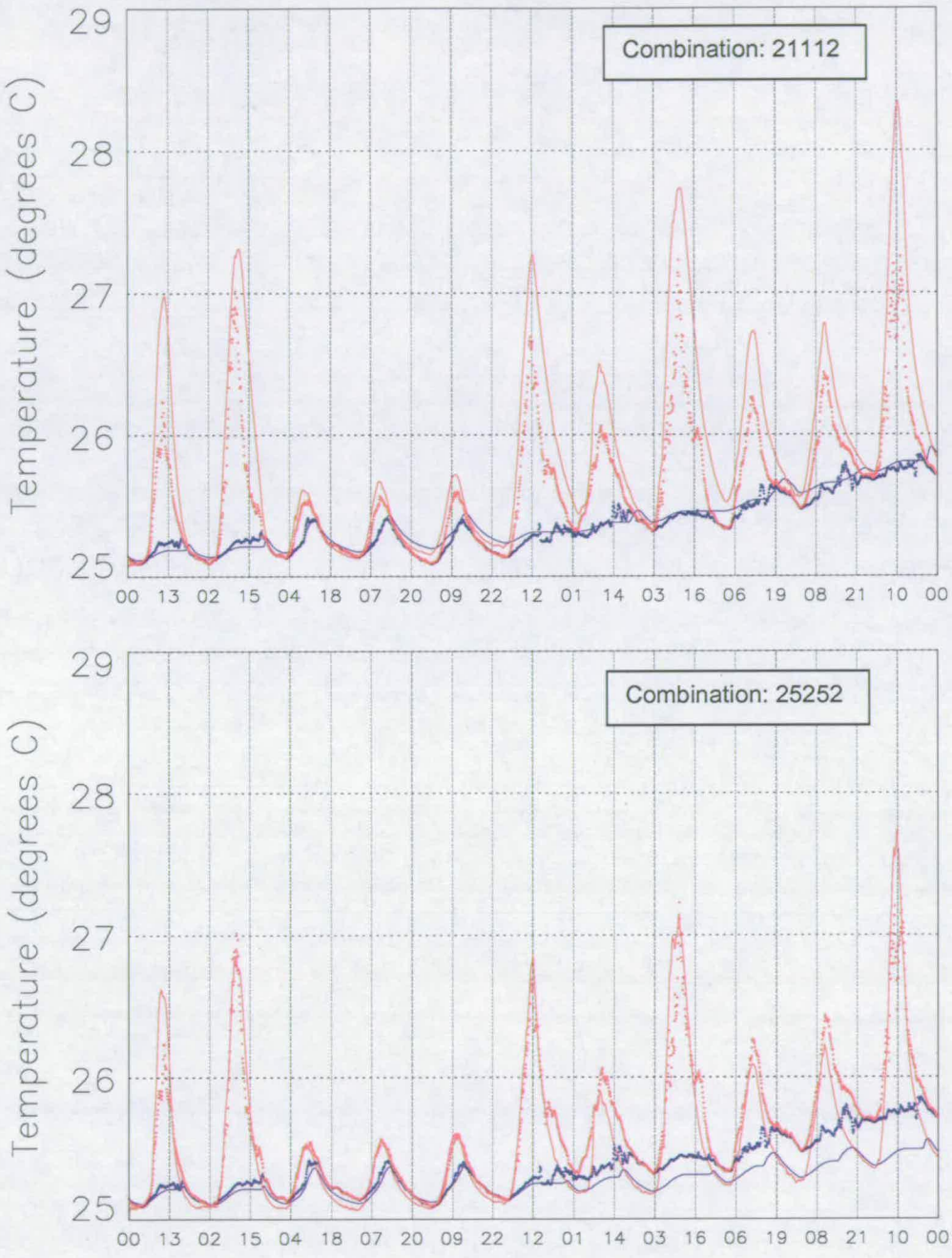

Figure 4.14 Arabian Sea 11 day model validation. Comparison of modelled SST at top sensor (0.17 m) and at 5 m using original (public domain version) options (top) and best of the combinations of added and original options (bottom).

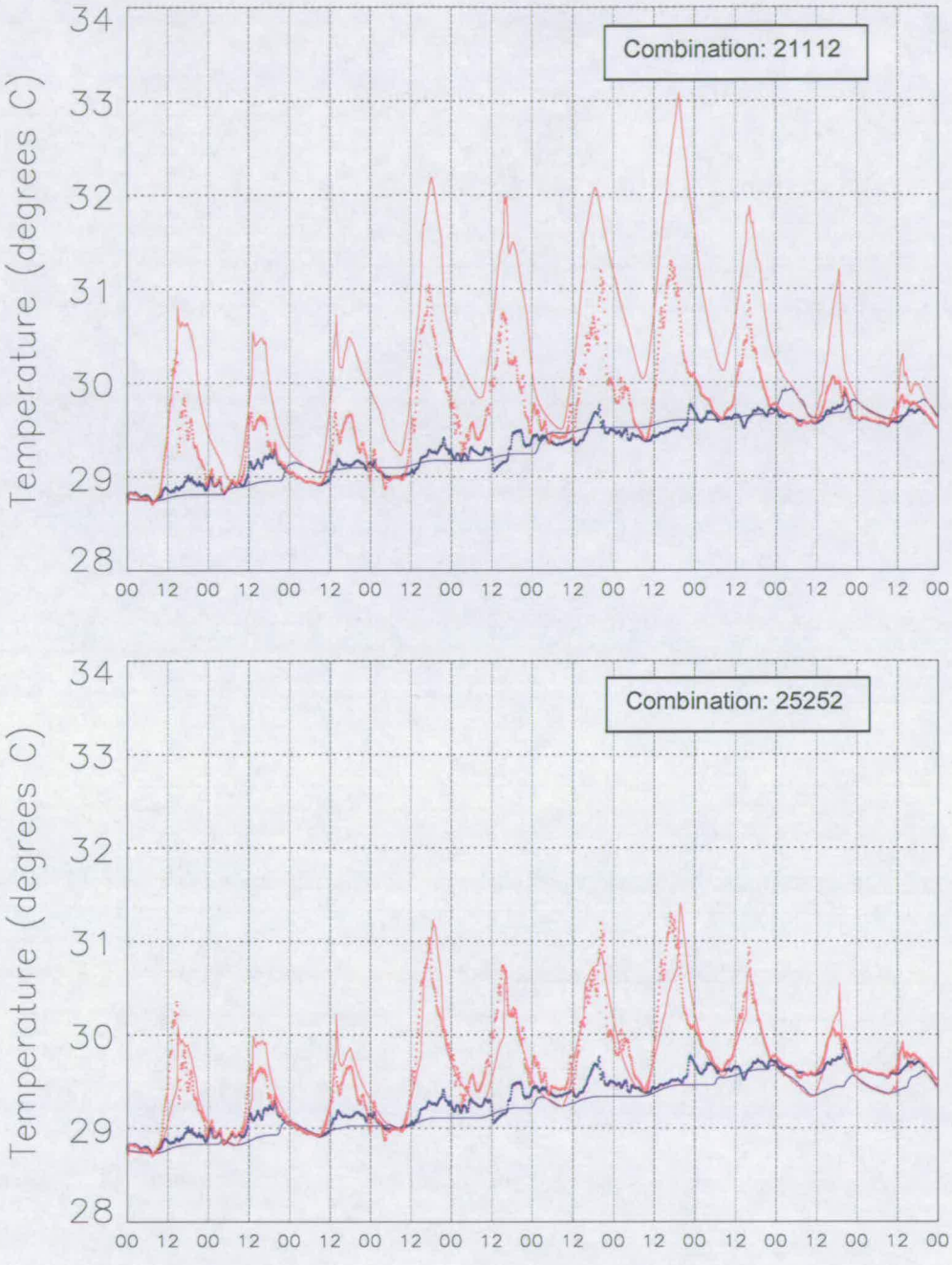

Figure 4.15 COARE 10 day model validation. Comparison of modelled SST at top sensor (0.45 m) and at 5 m using original (public domain version) options (top) and best of the combinations of added and original options (bottom).

Figure 4.14 and Figure 4.15 show that the enhanced model predicts top sensor SST significantly better than the original model for these two validation data sets. Diurnal amplitude at the top sensor and stratification between 5 m and the top sensor are also evidently improved. These assertions from the figures are verified by the RMS statistics given in Table 4.11.

Property	Code	Arabian	COARE
SST at top sensor depth	21112	0.39	0.76
	25252	0.19	0.24
Diurnal amplitude at top sensor depth	21112	0.46	0.77
	25252	0.20	0.33
Stratification	21112	0.38	0.77
	25252	0.20	0.27

Table 4.11 Validation data set comparison, by RMS of residuals (°C) of three properties, of original (public domain version) and the best combination of the enhanced model.

From Figure 4.14, the original model simulates the drift of the 5m temperatures in the Arabian Sea data-set a little better than the new model. However, the shape of the diurnal cycle of temperature is not as well simulated by the original model. The results in Table 4.11 show that the diurnal amplitudes and stratification are better simulated overall by the new model.

4.12 Summary

An extensive sensitivity test of 200 combinations of options (for calculating fluxes and distribution of SSI in the water column) has been carried out. It has been shown that with the best combination of enhancements made to the model, a significant improvement in model skill, with respect to diurnal warming of SSTs, can be made, compared to the original model.

Chapter 5 Model response to meteorological forcing

This chapter is concerned with the model sensitivity to the quality of meteorological forcing data. The sensitivity to the time-resolution of surface solar irradiance (SSI) and to the time-resolution of wind speed and other 'non-solar' meteorological data is explored.

Various subsets of observed meteorological data for a particular location could be obtained from different sources. For example, SSI could be derived from satellite data whilst wind speed, air temperature and humidity may be obtained from e.g. an instrumented mooring or numerical weather prediction data.

The motivation for this study is to find out whether sources of data (alternative to in-situ and with greater spatial coverage) can be used to force the model and still obtain predictions of diurnal variability response suitable for the purpose of extending the modelling of SSTs to the global ocean.

Since alternatives to in-situ data are usually lower resolution than in-situ data, it is important to know how the temporal resolution of the available data will affect the modelled SST. Specifically, how coarse can the time resolution be whilst maintaining the required model skill? The answer might be different for the different forcing-data subsets. Diurnal variability of SST is most sensitive to SSI and wind speed and the model sensitivity to the resolutions of these is investigated here.

When there is an absence of observed, high-resolution data to force the model, it may be possible to make use of numerical weather prediction fields. The European Centre for Medium Range Weather Forecasting (ECMWF) produces modelled meteorological data with 6-hourly resolution for the entire

globe. The effect on model skill of substituting buoy data with ECMWF data for the buoy location is explored.

To investigate how the model skill is affected by the temporal resolution of the forcing data, sensitivity tests are carried out with high-resolution data that are progressively degraded by averaging up to give lower temporal resolutions. The results are analysed in two parts. Part A compares the modelled SSTs using increasingly degraded resolution of forcing data to the modelled SSTs using the highest-resolution forcing data. Part B compares the modelled SSTs using increasingly degraded forcing-data resolution to the observed SST.

5.1 Sensitivity test of model skill to the resolution of forcing data

In this test, the time resolutions of SSI and wind-speed dependent data are varied independently of each other. As well as the direct affect of wind speed on wind stress, it is appropriate also to vary the time resolutions of other 'non-solar' meteorological data. The non-solar heat fluxes (NSHF), apart from net longwave radiation, are directly dependent on the wind speed (The resolution of the net longwave radiation is dependent on the time resolution of SST). Therefore, the resolution of the wind speed determines the resolution of the NSHF (apart from the radiative component). Wind speed varies more rapidly than air temperature and humidity and therefore NSHF are most sensitive to variations in wind speed. From here on, time resolution of wind speed and other 'non-solar' meteorological data (air-temperature, humidity, pressure) will be referred to as time resolution of wind speed only.

Two data sets were chosen for this test: the Arabian sea (15^{O} N 61^{O} E, 19th February 1995 to 1st March 1995) and COARE (2^{O} S 156^{O} E; 7th January 1993 to 17th January 1993). These data sets are at the same locations as the data sets used to calibrate the model in Chapter 4 but the dates and times are different. For these tests it is useful to have the high vertical resolution available at these locations, which the third location, LOTUS, does not have.

To produce data with the required resolutions, the 7.5 minute data were averaged up to obtain data with the following resolutions (in minutes) for both SSI and wind speed: 7.5, 15, 30, 60, 120, 180, 360. The effect of this averaging can be seen in Figure 5.1 (b), (c) and (d) in the step appearance of the forcing data. The forcing data in Figure 5.1 are examples of combinations of SSI and wind-speed resolution: (a) 7.5 minute SSI, 7.5 minute wind speed, (b) 7.5 minute SSI, 180 minute wind speed, (c) 180 minute SSI, 7.5 minute wind speed, (d) 360 minute SSI, 360 minute wind speed.

The model was run with each data set (Arabian sea and COARE) with all possible combinations of the resolutions of SSI and wind speed (and associated meteorology). These are input resolutions. The model time-step is 30 seconds and the model results are recorded at 7.5 minute resolution in the output file. This gives a total of 7*7 = 49 combinations. The modelled SST of four of these combinations are shown in Figure 5.1 and 5.2. Each sub-figure (a,b,c and d) of Figures 5.1 and 5.2 is comprised of three plots: the SSI and the Non-Solar Heat Fluxes (NSHF); the wind speed; the modelled SST (solid lines) and observed SST (dashed lines) at 5 m and the top sensor (0.17 m for Arabian Sea and 0.45 m for COARE).

In Figure 5.1 and 5.2 it can be seen that the model forced by the high resolution data (a) predicts SST with more skill than when forced by the 360 minute resolution SSI and wind speed data (d). However, it is less obvious how skilful the model is for resolutions between the extremes, i.e. (b) and (c). It is necessary then to examine the metrics of each combination. The metrics examined are: RMS of residuals of SST at the top sensor, diurnal amplitude of SST and thermal stratification. The metrics for the Arabian Sea are plotted in Figure 5.3 and those for COARE are plotted in Figure 5.4.

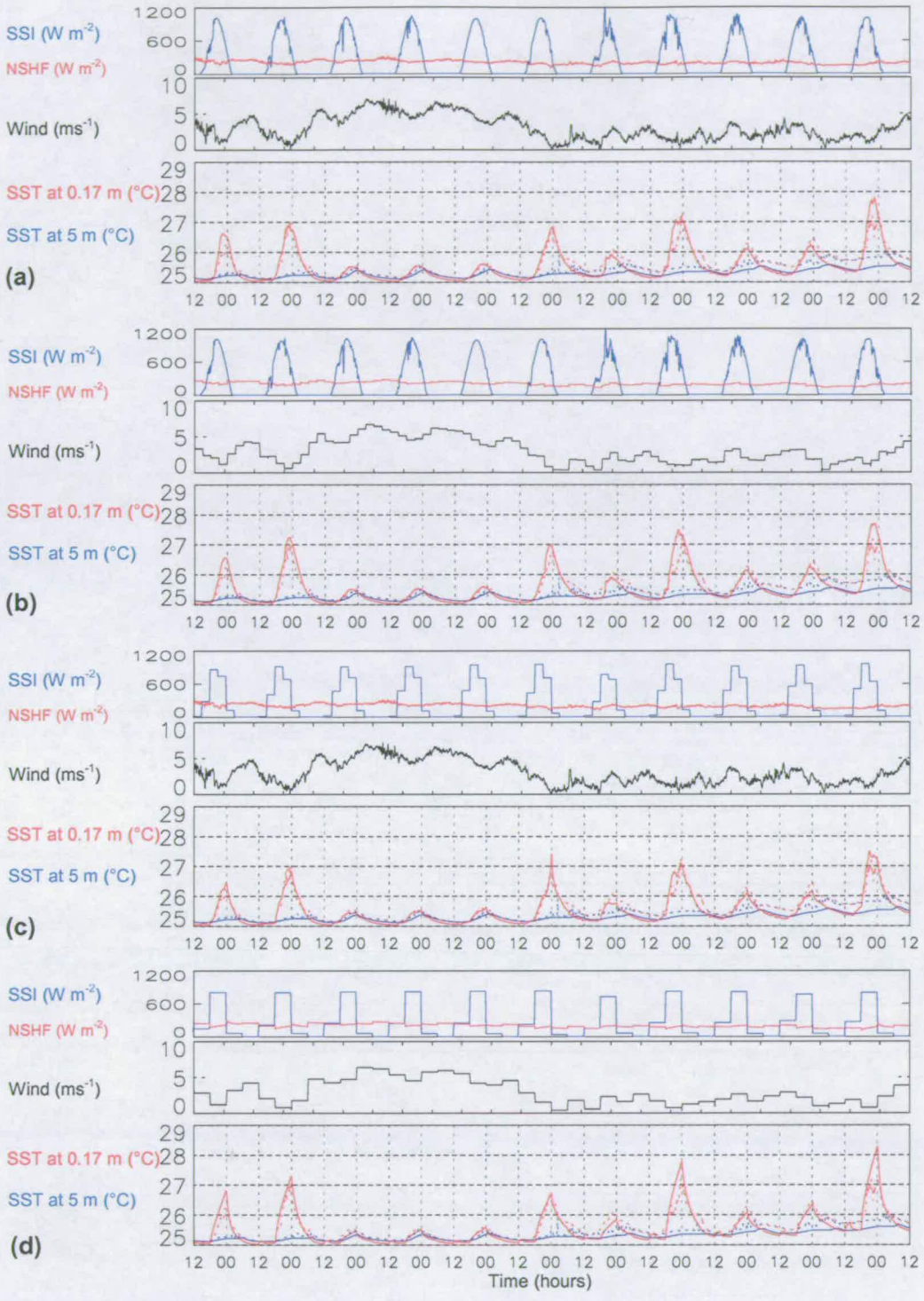

Figure 5.1 Effect of degrading the resolution of the forcing data on modelled SST. (a) original resolution 7.5 minute SSI, 7.5 minute wind speed; (b) 7.5 minute SSI, 180 minute wind speed; (c) 180 minute SSI, 7.5 minute wind speed; (d) 360 minute SSI, 360 minute wind speed. The dashed lines are observed SST. Arabian sea, 19/02/1995 to 01/03/1995.

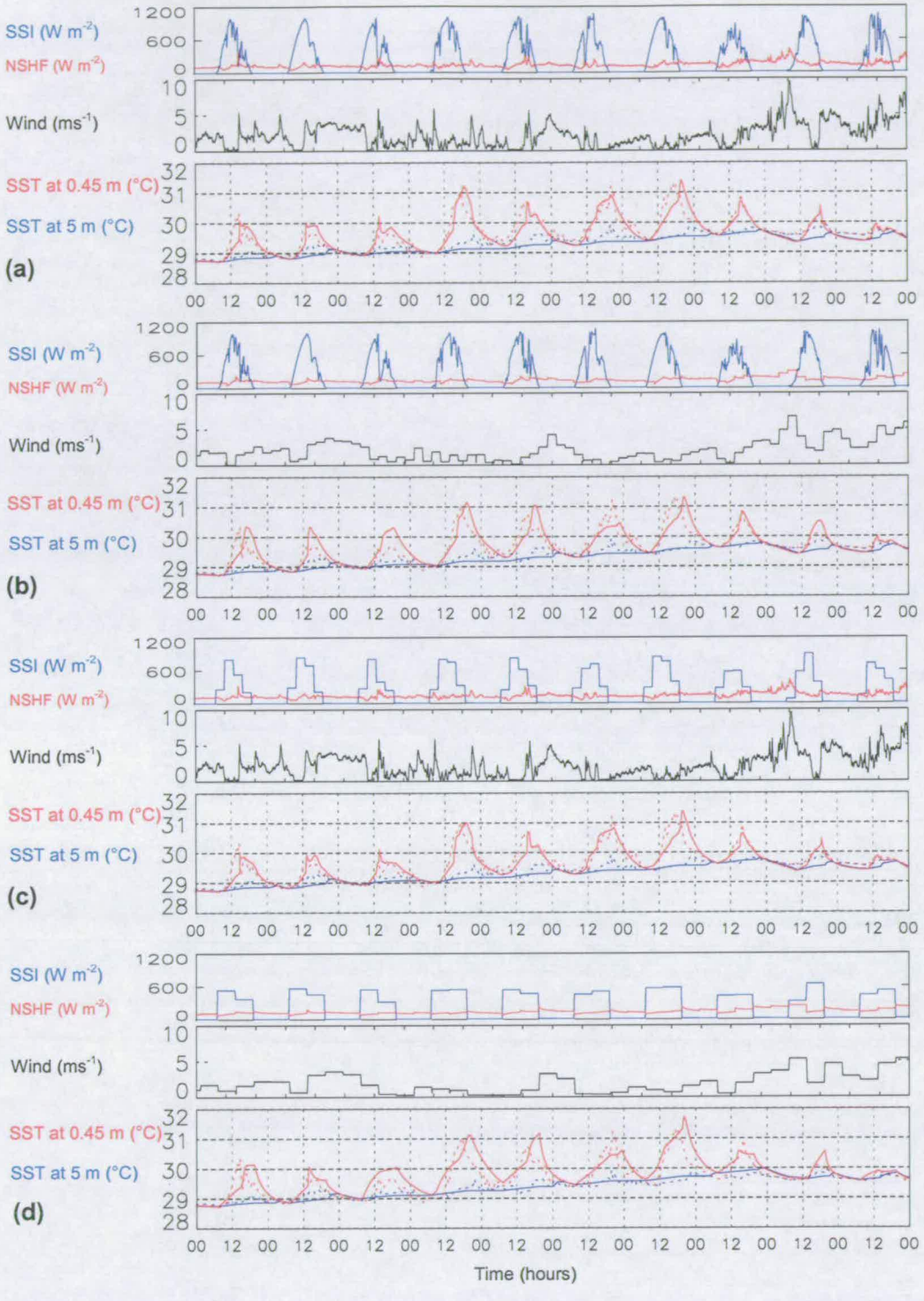

Figure 5.2 Effect of degrading the resolution of the forcing data on modelled SST. (a) original resolution 7.5 minute SSI, 7.5 minute wind speed; (b) 7.5 minute SSI, 180 minute wind speed; (c) 180 minute SSI, 7.5 minute wind speed; (d) 360 minute SSI, 360 minute wind speed. The dashed lines are observed SST. COARE 07/01/1993 to 17/01/1993.

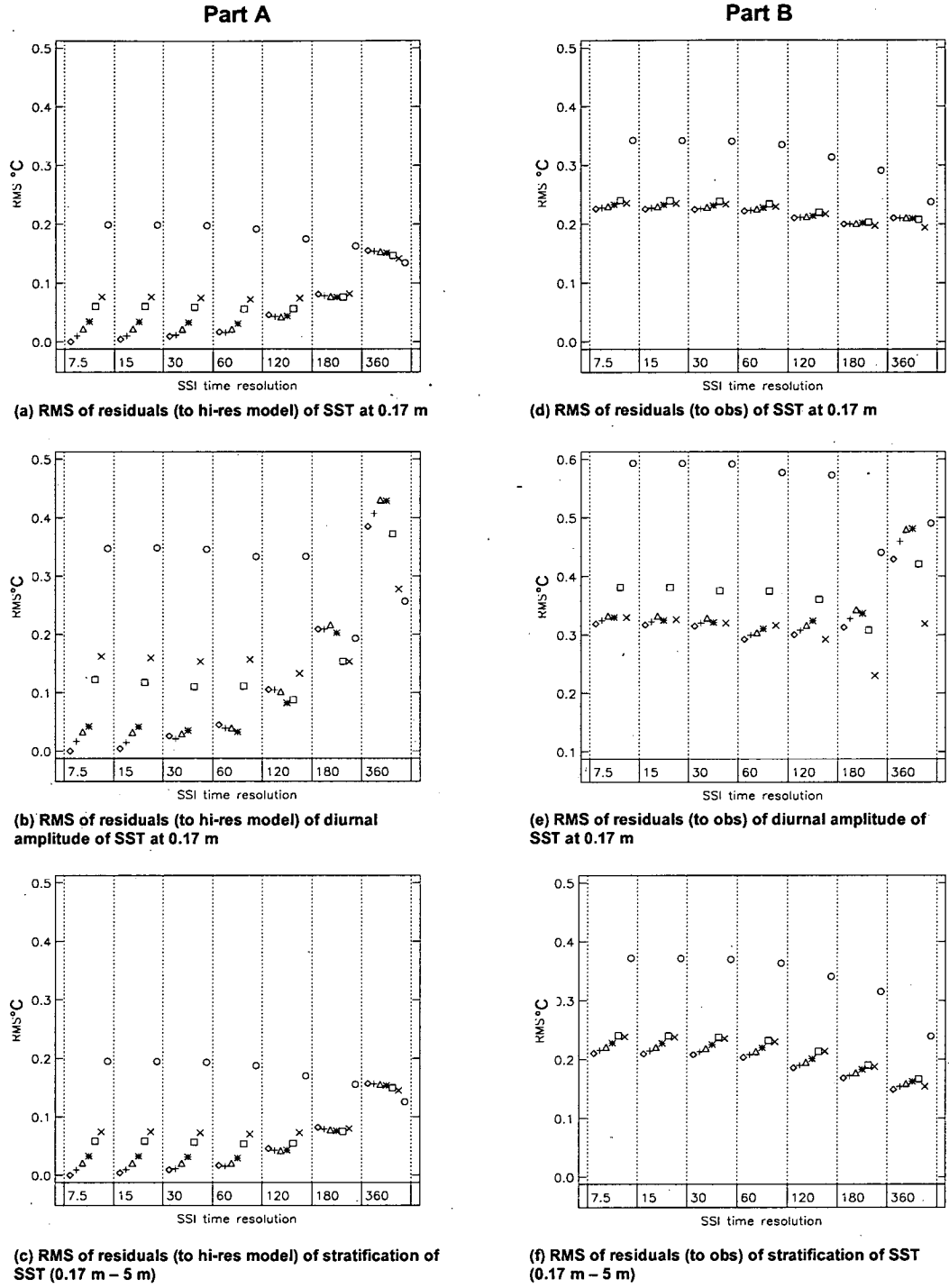

(a) RMS of residuals (to hi-res model) of SST at 0.17 m

(d) RMS of residuals (to obs) of SST at 0.17 m

(b) RMS of residuals (to hi-res model) of diurnal amplitude of SST at 0.17 m

(e) RMS of residuals (to obs) of diurnal amplitude of SST at 0.17 m

(c) RMS of residuals (to hi-res model) of stratification of SST (0.17 m – 5 m)

(f) RMS of residuals (to obs) of stratification of SST (0.17 m – 5 m)

Wind resolution key (minutes): ◇ 7.5, + 15, Δ 30, ✳ 60, □ 120, × 180, O 360.

Figure 5.3 RMS of residuals for all combinations of resolution. Part A: residuals are between modelled SST of given resolution and modelled SST with highest resolution forcing data. Part B: residuals are between modelled SST of given resolution and observed SST. Arabian sea, 19/02/1995 to 01/03/1995.

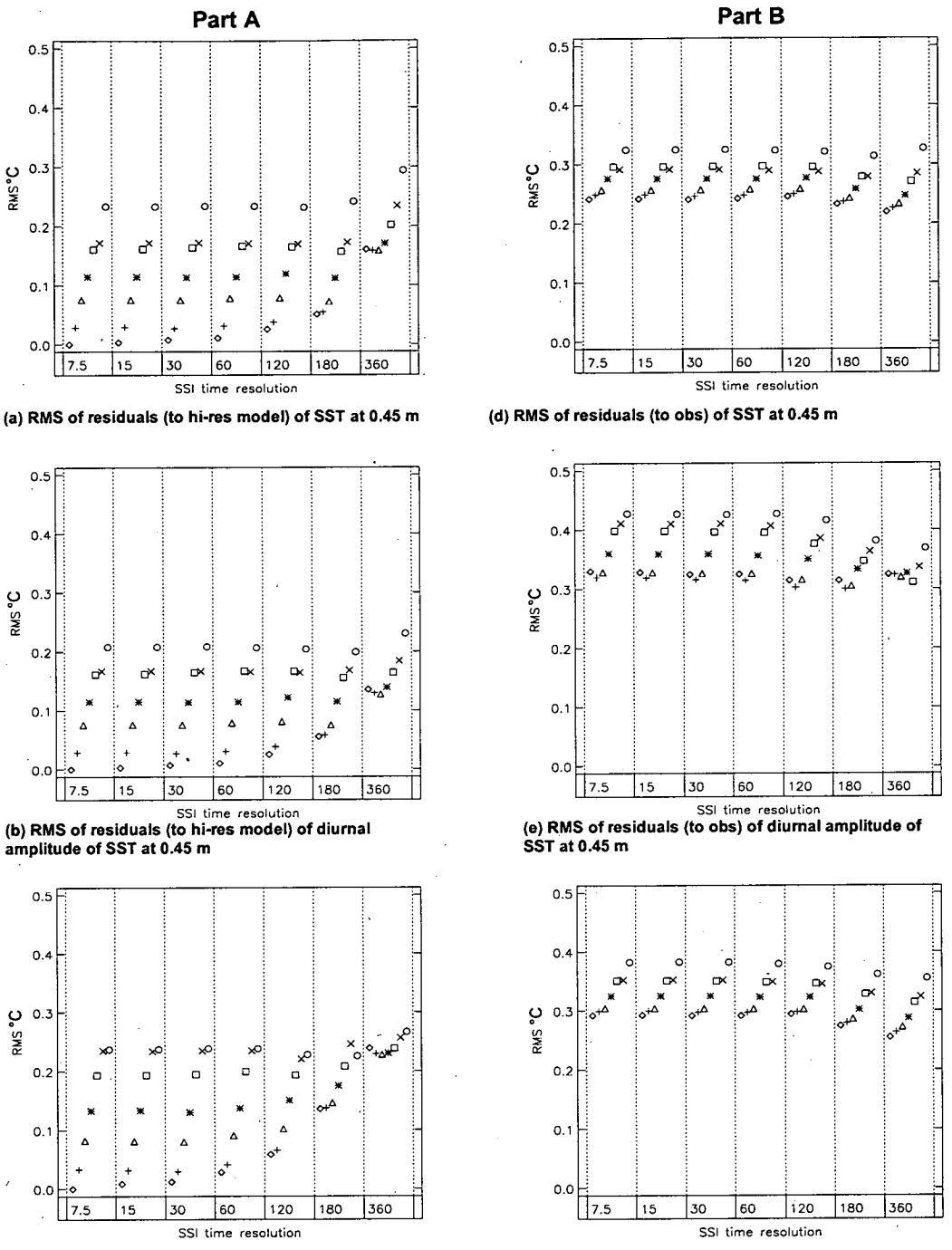

(a) RMS of residuals (to hi-res model) of SST at 0.45 m

(d) RMS of residuals (to obs) of SST at 0.45 m

(b) RMS of residuals (to hi-res model) of diurnal amplitude of SST at 0.45 m

(e) RMS of residuals (to obs) of diurnal amplitude of SST at 0.45 m

(c) RMS of residuals (to hi-res model) of stratification of SST (0.45 m – 5 m)

(f) RMS of residuals (to obs) of stratification of SST (0.45 m – 5 m)

Wind resolution key (minutes): ◇ 7.5, + 15, Δ 30, ✳ 60, □ 120, × 180, O 360.

Figure 5.4 RMS of residuals for all combinations of resolution. Part A: residuals are between modelled SST of given resolution and modelled SST with highest resolution forcing data. Part B: residuals are between modelled SST of given resolution and observed SST. COARE 07/01/1993 to 17/01/1993.

"Part A" comparisons

In Figure 5.3 and 5.4 (a), (b) and (c), the residuals are between the model run with a given data resolution and the model run with the high-resolution 7.5 minute SSI and 7.5 minute wind-speed data. Thus the first points on Figure 5.3 (a), (b) and (c) show a RMS of residuals of zero. These runs were carried out to explore the effect of varying the resolutions of SSI and wind speed, without concern about other sources of error (between model and observations). The model run with the highest resolution is assumed the 'truth' and the model runs with other combinations of data resolution are compared to the assumed truth.

The skill at near surface SST prediction deteriorates more rapidly with worsening wind-speed resolution than with worsening SSI resolution. In Figures 5.3 and 5.4, diamonds represent the metrics of model runs with wind speed resolution of 7.5 minutes. In Figure 5.3 (a) the RMS, following diamonds, increases from 0.0, for SSI at 7.5 minute resolution to 0.16 for SSI at 360 minute resolution. However, with the SSI resolution kept constant at 7.5 minutes, following symbols in the 7.5 minute SSI 'bin', the RMS increases from 0.0 to 2.0. For the COARE data, Figure 5.4 (a), the RMS, following diamonds, increases from 0.0, for SSI at 7.5 minute resolution to 0.16 for SSI at 360 minute resolution. With the SSI resolution kept constant at 7.5 minutes, following symbols in the 7.5 minute SSI 'bin', the RMS increases from 0.0 to 2.5.

For the Arabian Sea data set, RMS metrics generally increase with decreasing wind-speed resolution for resolutions of SSI down to 120 minutes. For the COARE data, RMS metrics increase with decreasing wind-speed resolution except for SSI resolution of 360 minutes, where the RMS metrics decrease until the wind-speed resolution is degraded to 30 minutes. RMS metrics then increase with further degradation of the wind-speed resolution.

"Part B" comparisons

In Figures 5.3 and 5.4 (d), (e) and (f), the RMS of residuals are between the model run with a given data resolution and the high resolution observations.

For SST prediction, the results obtained are similar to part A but with higher RMS values. In general the RMS metrics are more affected by worsening wind-speed resolution than SSI resolution and for some of the metrics, i.e. stratification in the Arabian Sea data set, the RMS of residuals generally improves with worsening SSI which is a surprising result but this could be a case of equifinality.

Note that the details of higher frequency fluctuations in SST are lost with low wind-speed resolutions (e.g. 3 hourly). This is not the case with solar radiation resolution of 3 hours. In Figure 5.2, on days 3, 5 and 8, the sub-diurnal frequencies of SST remain between (a) and (c) but not between (a) and (b).

Part A and Part B taken together, the conclusions are that the RMS metrics are not so affected by worsening SSI resolution as they are by worsening wind-speed resolution. The RMS metrics worsen progressively with degradations in the time resolution of wind speed, with significant worsening of the metrics when time resolution is greater than of order half an hour (at least for "part A"). SSI time resolution, in contrast, must be degraded to of order 2 hours before significant worsening of the metrics is observed. Although the model skill was shown to be sensitive to only small degradations of wind speed resolution, the diurnal cycle can be modelled using 3 hourly wind and meteorology with useful agreement to the observations. When comparing the metrics of modelled SST to observed SST, for the Arabian Sea data set, there was very little loss in performance in comparison to the high-resolution 7.5 minute data.

5.2 Alternatives to *in situ* data: ECMWF meteorological data and calculated SSI.

The European Centre for Medium Range Weather Forecasts (ECMWF) produces modelled meteorological data with 6-hourly resolution on a global grid with spatial resolution of 1.125^{O} (latitude and longitude). This is the 'operational' data and is available from 1st March 1994 to the present date. The ECMWF also produce re-analysis data (1957 to August 2002) with latitudinal resolution of 1.125^{O} but with a reduced longitudinal resolution such that the number of grid points in a meridian circle reduces with increasing latitude.

The advantages of reanalysis over operational data are that it offers several years of fields from an unchanging system and that the fields can be more easily obtained. The disadvantage is that by the time the complete reanalysis record is available, the system used is lower resolution and uses older less developed physical parameterisations than the operational systems (Report of the working group on air-sea fluxes 2000).

Figure 5.5 to Figure 5.8 compare the in-situ high resolution (7.5 minutes) wind speed from the Arabian Sea and COARE moorings to the 6 hourly ECMWF ERA 40 wind speed for those locations. The simulations using the 6 hourly ECMWF ERA 40 meteorology are compared with the simulations using the high resolution data in Figure 5.11 and Figure 5.12.

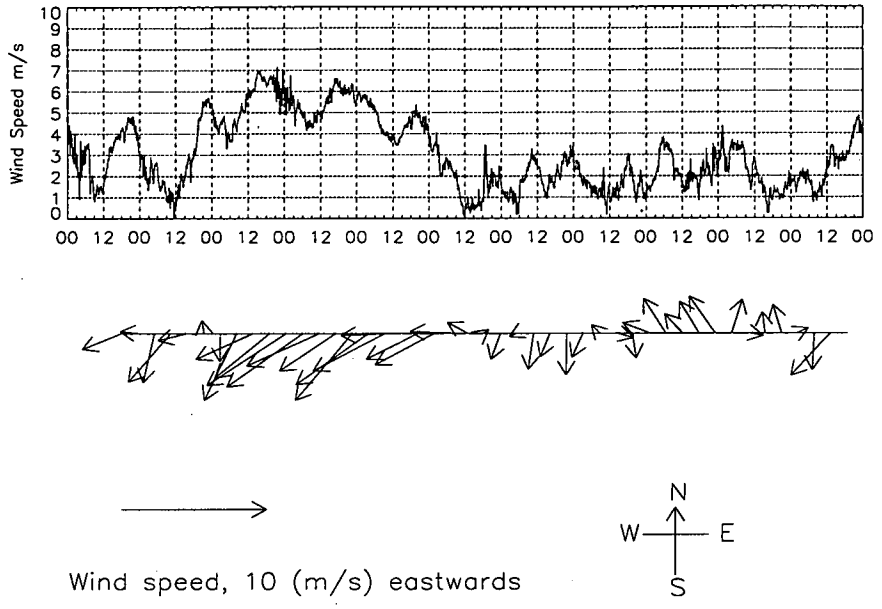

Figure 5.5 High resolution (7.5 minute) wind speed from in-situ buoy at 15N 61 E in the Arabian Sea. The blue lines are the average wind direction at 6 hourly intervals.

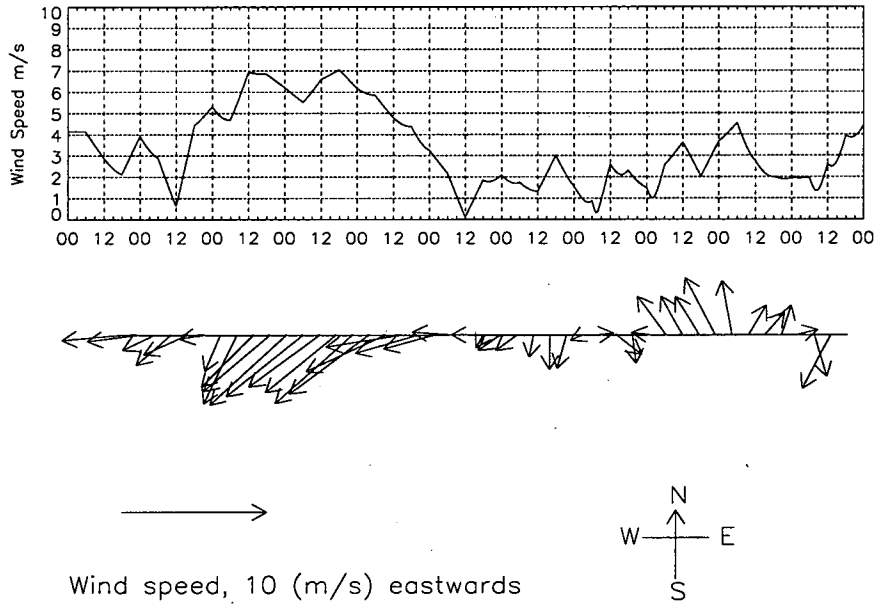

Figure 5.6 ECMWF ERA40 wind speed from at 15N 61 E in the Arabian Sea. The blue lines are the average wind direction at 6 hourly intervals.

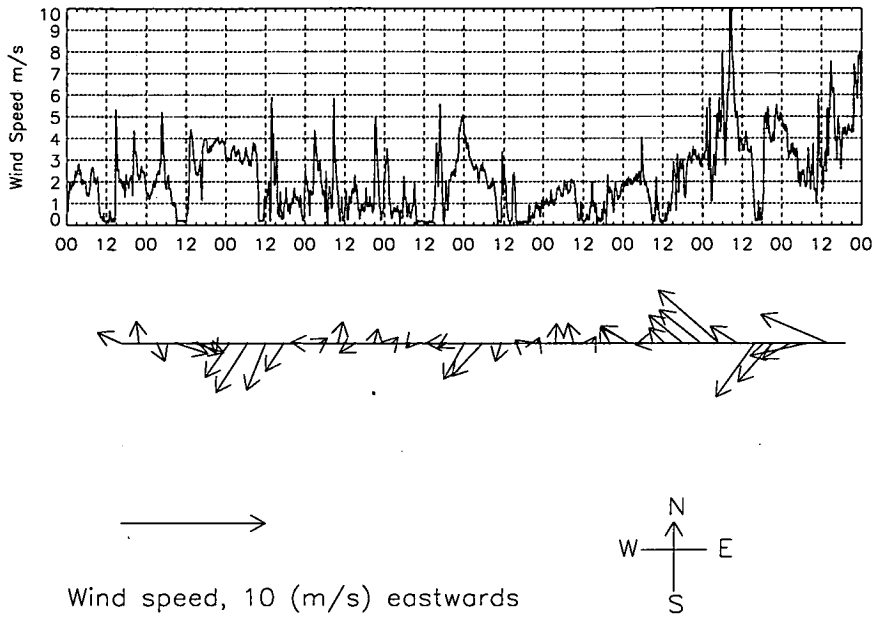

Figure 5.7 High resolution (7.5 minute) wind speed from in-situ buoy at 2S 156E in the Pacific (COARE 07/01/1993 to 17/01/1993). The blue lines are the average wind direction at 6 hourly intervals.

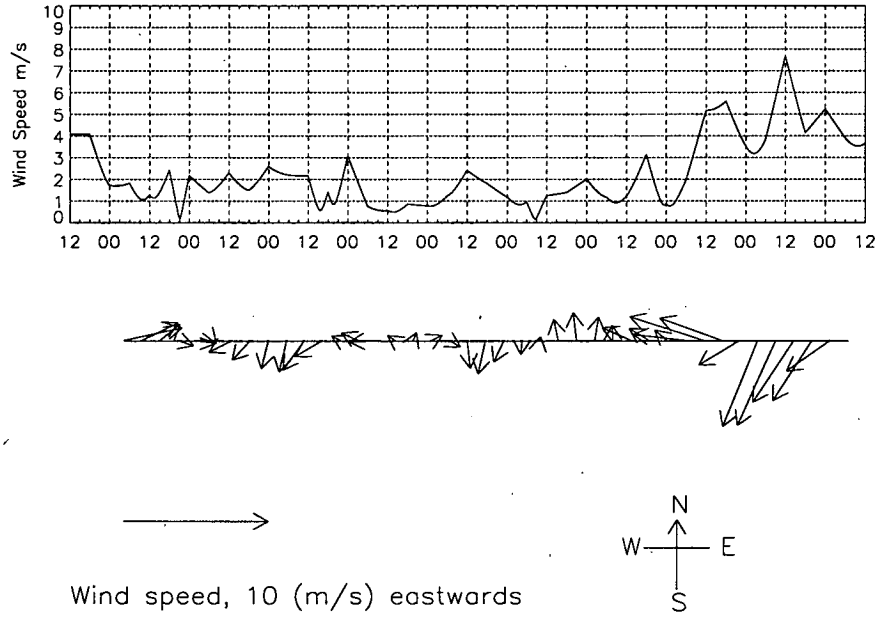

Figure 5.8 ECMWF ERA40 wind speed from at 2S 156E in the Pacific (COARE 07/01/1993 to 17/01/1993). The blue lines are the average wind direction at 6 hourly intervals.

For the Arabian Sea, the RMS of residuals between the high-res buoy wind speed and the ERA 40 wind speed is 0.91 m s^{-1} (over the 11 day period). For the COARE data, the RMS of residuals (ERA 40 vs. buoy) of wind speed is 1.46 m s^{-1}. Figure 5.9 and Figure 5.10 show the direct comparisons between the high-resolution in-situ wind speeds and the corresponding collocated ERA 40 reanalysis wind speeds. The COARE wind speeds have larger amplitude high frequency variations than the Arabian Sea winds and this partly explains the poorer RMS residual value for the COARE data.

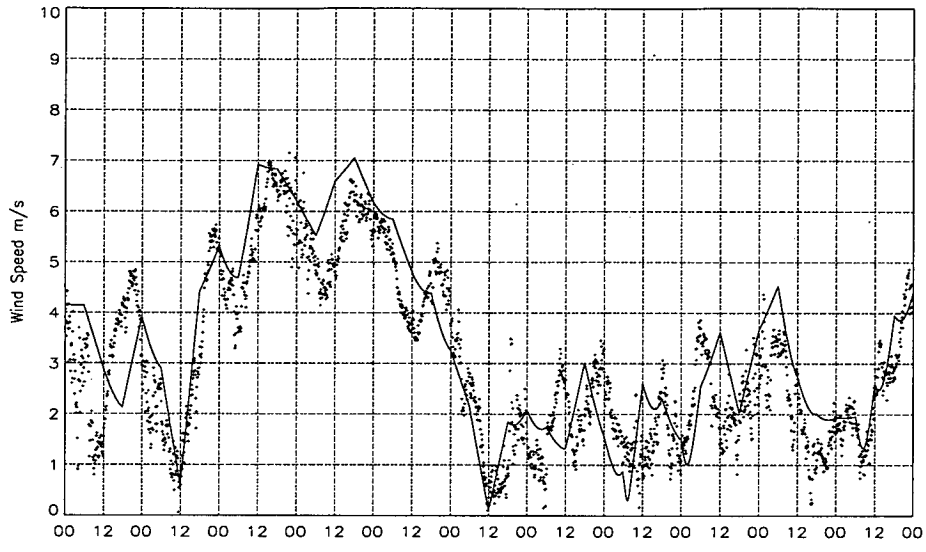

Figure 5.9 Wind speed from ECMWF ERA 40 reanalysis at the buoy location (solid line) compared with high resolution (7.5 minute) in-situ wind speed data at the buoy (dots). Arabian Sea: 15 N 61 E, 19/02/1995 to 01/03/1995

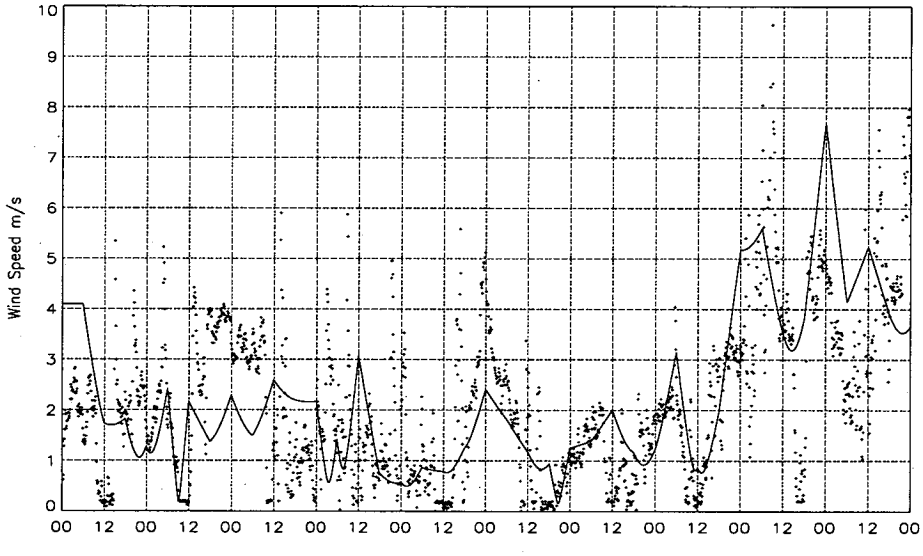

Figure 5.10 Wind speed from ECMWF ERA 40 reanalysis at the buoy location (solid line) compared with high resolution (7.5 minute) in-situ wind speed data at the buoy (dots). COARE: 2 S 156 E, 19/02/1995 to 01/03/1995

Figure 5.11 and Figure 5.12 show the time series of SST at the top sensor and at 5 m for the Arabian Sea and COARE data sets respectively. The first (top) plot in each figure is the model forced with high-resolution data. The second (middle) plot in each figure is the model forced with ECMWF data. The third (bottom) plot in each figure is the model forced with 6 hourly data generated from the high resolution buoy data.

The RMS of residuals (model vs. observed data) from forcing with ECMWF ERA 40 data compared to forcing with high-resolution data and the 6 hourly averages of the high-resolution winds ("hi-res") are given in Table 5.1.

Property	RMS of residuals (°C). Arabian Sea			RMS of residuals (°C). COARE		
	Type of forcing data			Type of forcing data		
	Hi-res	6-hourly	ECMWF	Hi-res	6-hourly	ECMWF
SST at top sensor depth	0.19	0.34	0.28	0.24	0.33	0.43
Diurnal amplitude at top sensor depth	0.20	0.59	0.55	0.33	0.43	0.53
Stratification	0.20	0.37	0.22	0.27	0.38	0.27

Table 5.1 Comparison, by RMS of residuals (°C) of three properties of SST modelled using three different types of forcing data .

The SSTs modelled using ECMWF ERA 40 reanalysis fields as forcing compare favourably to those modelled using the 6-hourly fields derived from the in-situ data. For the Arabian Sea, the RMS of residuals of all properties in Table 5.2 are (surprisingly) less when using ECMWF ERA 40 forcing fields than when using forcing from six-hourly in-situ data. In the case of COARE, the RMS values are instead mostly better with the six-hourly in-situ data, as one would expect. Taken together, these results suggest that when the forcing-data resolution is low (6-hourly), the model skill in using reanalysis is

fairly comparable to that using in-situ data. Figure 5.11 and Figure 5.12 show that the shape and timing of the diurnal cycle at the top sensor in each of the data sets are also modelled at least as well with ECMWF data as with the 6-hourly data.

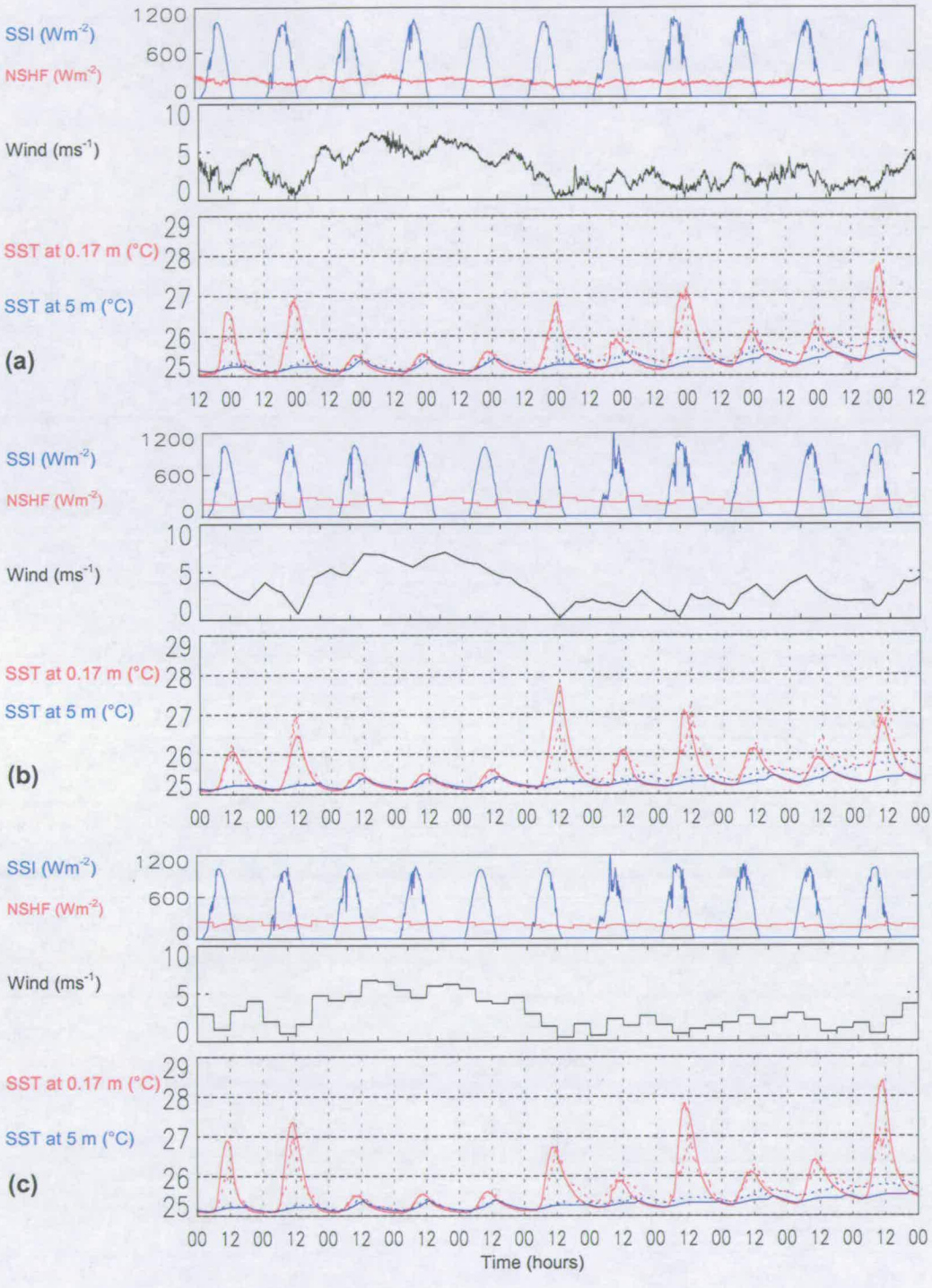

Figure 5.11 Simulations at 15 N 61 E in the Arabian Sea forced with: (a) hi-res buoy data, (b) hi-res SSI from buoy and ECMWF ERA 40 reanalysis meteorology (6 hourly), c) 6-hourly buoy data generated from high resolution buoy meteorological data.

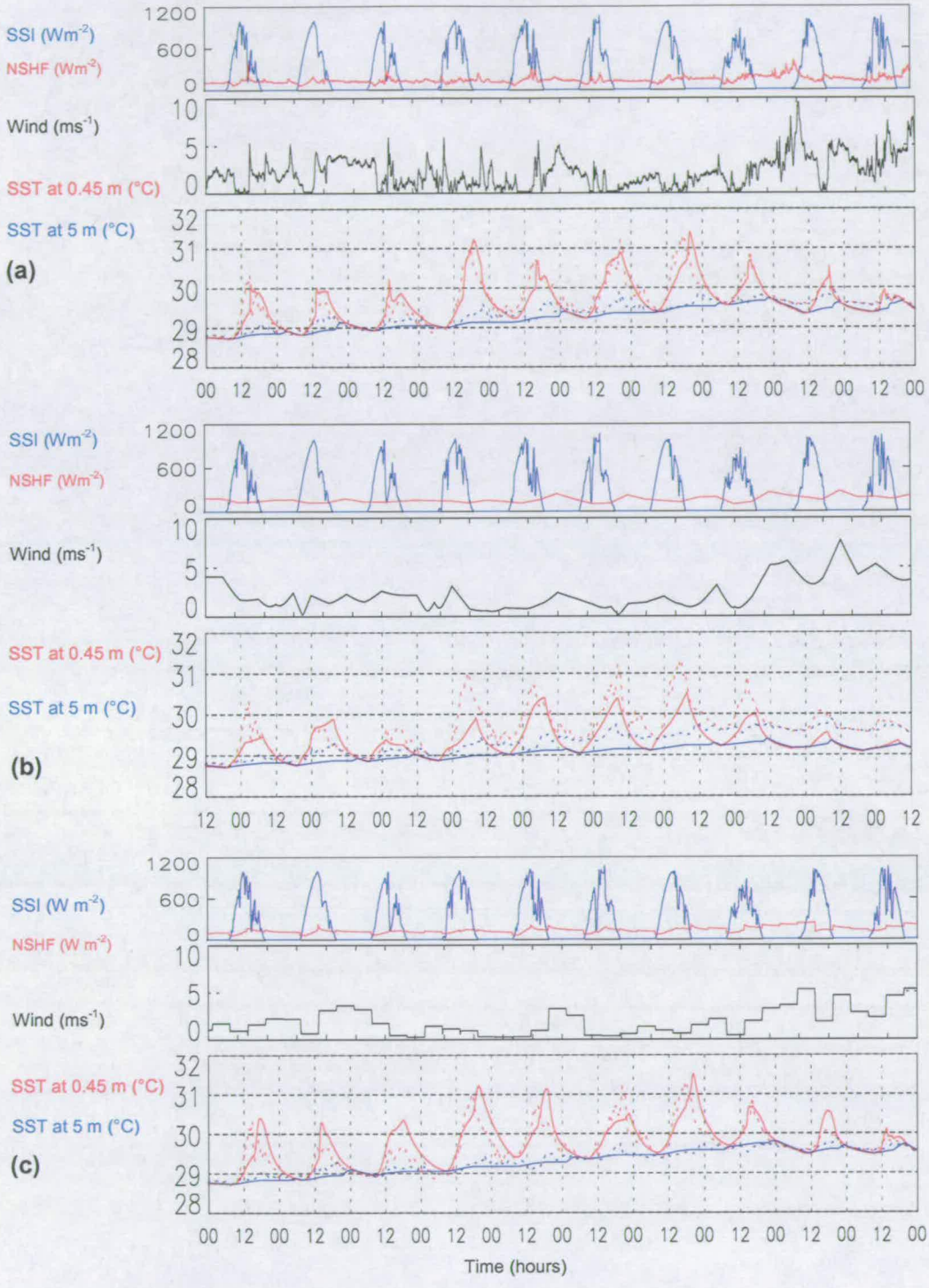

Figure 5.12 Simulations at 2 S 156 E in the pacific (COARE) forced with: (a) all hi-res buoy data, (b) hi-res SSI from buoy and ECMWF reanalysis meteorology (6 hourly), (c) 6-hourly buoy data generated from high resolution buoy meteorological data.

5.3 Summary

In the first part of this chapter, the sensitivity of model skill to resolution of the SSI and wind speed forcing was investigated. The RMS metrics are not so affected by worsening SSI resolution as they are by worsening wind-speed resolution. The RMS metrics worsen progressively with degradations in the time resolution of wind speed, with significant worsening of the metrics when time resolution is greater than of order half an hour. SSI time resolution, in contrast, must be degraded to of order 2 hours before significant worsening of the metrics is observed. The time scale of the response of SST to variations in wind speed is shorter than the response to variations in SSI.

Although the model skill was shown to be sensitive to only small degradations of wind speed resolution, the diurnal cycle can be modelled using 3 hourly wind and meteorology with useful agreement to the observations. When comparing the metrics of modelled SST to observed SST, for the Arabian Sea data set, there was very little loss in performance in comparison to the high-resolution 7.5 minute data.

Alternatives to *in situ* data, with the advantage of greater spatial coverage can be used to force the model and still obtain predictions of diurnal variability response suitable for the purpose of extending the modelling of SSTs to the global ocean. The research of the second part of chapter 5 suggests that ECMWF ERA 40 reanalysis data is as good as 6-hourly *in situ* data for the purpose of modelling diurnal warming.

Chapter 6 Comparisons with SST from Meteosat Second Generation

In chapter 1, the features of the near-surface temperature profile of the ocean were described and their significance to this research explained. Recall that the temperature at the air-sea interface, the 'skin' sea surface temperature (SSST), is the parameter to which radiometric satellite measurements are sensitive. Over the ocean, space-borne infrared-sensitive instruments detect radiation emitted from the top few microns and temperatures derived from the measurement of this radiation represent the SSST.

The estimates of SSST from measurements made by instruments on board the Meteosat Second Generation (MSG) satellite (also known as Meteosat 8) are known as SST retrievals. There are ten buoy locations in the Pilot Research moored Array in the Tropical Atlantic (PIRATA). This chapter presents comparisons of modelled SSST at buoy locations in the Atlantic Ocean with collocated SSST estimates from Meteosat 8.

6.1 Motivation

The motivation for this work is to explore whether it is possible to model SSSTs with useful agreement to SSSTs from satellite based measurements. This would be a useful test because a direct comparison with satellite observations of diurnal SSST hasn't been done. This is a first step toward assimilation of the diurnal cycle and as a validation of the model application to large horizontal scales rather than *in situ* point data.

Specifically, can the model predict Meteosat 8 satellite SSSTs within the accuracy of Meteosat 8 SST retrievals: ± 0.5 K rms. When there are sufficient satellite observations to define a diurnal cycle, can the model simulate the diurnal variation observed in the satellite derived SSSTs? If conditions arise

that promote stratification at the surface, does the model predict this stratification with the modelled SSST in agreement with the Meteosat 8 SST match-ups during diurnal warming events? Data from the Meteosat 8 geostationary satellite provides new opportunities for diurnal warming research because with clear skies, high-resolution time series of SSSTs can be retrieved with the potential to resolve the diurnal cycle.

6.2 The Data

The data used for this research are as follows.

- A year long record of Meteosat 8 satellite SSST, spanning July 2004 to July 2005, at the PIRATA buoy locations in the Atlantic Ocean.
- PIRATA buoy high-resolution meteorology, SSI and SST for July 2004.
- PIRATA daily average meteorology, SSI and SST for the period July 2004 to July 2005.
- ECMWF 6-hourly operational meteorology for the period July 2004 to July 2005.

6.2.1 The Meteosat 8 satellite

Meteosat 8 SST data are derived from radiometric measurements from the onboard Spinning Enhanced Visible and Infrared Imager (SEVIRI). Imaging is achieved with a bi-dimensional earth scan. East to west scanning is accomplished by means of the spacecraft's rotation about a north-south axis at a rate of 100 rpm. A scanning mirror is rotated from south to north, in steps of 125.8 microradians, to attain the latitudinal scan with 3 image lines acquired each revolution (ESA bulletin 111, August 2002). After cropping, the resulting full disk image has 3,712 x 3,712 pixels. This is a square image of approximately 13.8 million pixels that contains the visible earth disk as shown in Figure 6.1.

Figure 6. 1 A full disk image generated from near infra-red and two visible channels, reproduced from the Eumetsat image gallery

An image for each infrared channel is produced about every 12 minutes with a repeat cycle of 15 minutes. Calibration of the instrument and recovery of the mirror mechanism takes place in the interim. The imaging sampling distance at the sub-satellite point is 3 km for the infrared channels. The local pixel size depends on the latitude and longitude of the pixel. At the sub-satellite point, the resolution is 3 km, whereas over Central Europe the resolution is approximately 5 km

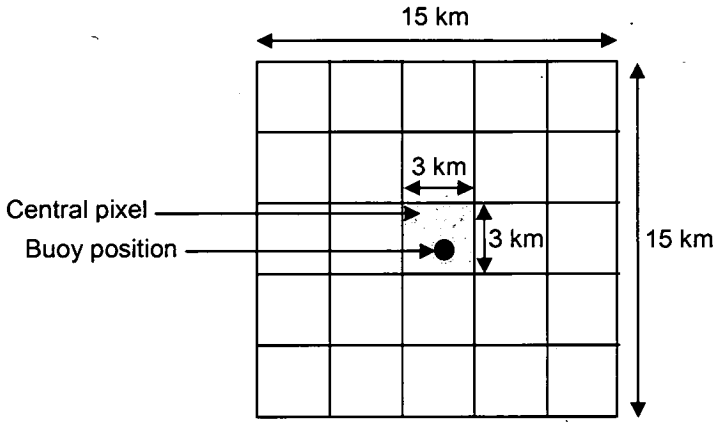

Figure 6. 2 Schematic diagram of a 5x5 validation box centred on the pixel containing the buoy location at nominally 0N 0W.

SST match-ups from the meteosat 8 satellite with the PIRATA array are derived from those pixels that collocate with the PIRATA buoy positions. Each SST match-up is derived with data from a validation box of 5x5 pixels centred on the pixel containing the buoy location see Figure 6.2. Therefore, ten 5x5 validation boxes make up the PIRATA database. The database contains many parameters. Those of importance here are: the central pixel SST; average calculated SST (from 25 pixels); 4 confidence levels (a measure of the confidence in the calculated SST) and the calculated SST standard deviation.

Over the whole match-up data base, the standard deviation of the central pixel SST from the average SST is 0.09K. In the figures that follow in this chapter, the central pixel SST is used as the match-up SST. Confidence levels refer to the percentage of pixels within the 25 pixel box with a given rating. The 4 confidence levels defined are: excellent, good, average and bad. It is recommended that match-ups with greater than 50% pixels in the 'bad' confidence level are rejected (personal communication with Pierre LeBorgne, Meteo-France, 08/09/2005)

6.2.2 PIRATA data

The Pilot Research moored Array in the Tropical Atlantic (PIRATA) is an array of ten instrumented buoys moored in the Atlantic Ocean. The purpose of PIRATA is to study ocean-atmosphere interactions in the tropical Atlantic that are relevant to regional climate variability on seasonal, interannual and longer time scales. The buoys are of the ATLAS type, equipped with a surface weather station (for measurements of wind, temperature, moisture, precipitation and solar radiation) and subsurface instruments, to record pressure, temperature and salinity between the surface and 500 m depth (on 11 levels for the temperature, 4 for salinity and 2 for the pressure). The depths of the instrument sensors are as follows:

PIRATA	SSC	TC1	TC2	T3	T4	T5	TC6	T7	T8	TP9	TP10
Depths (m), all sites	1	20	40	60	80	100	120	140	180	300	500

SSC is Sea Surface Conductivity and temperature. TC1, TC2 and TC6 are subsurface temperature and conductivity sensors. T3, T4, ..., T8 are subsurface thermistors. TP9 and TP10 are subsurface temperature and pressure sensors.

The meteorological data from the PIRATA buoys will be used to force the model and the *in situ* SSTs and the Meteosat 8 match-up SSTs will be compared with the model SSTs at the corresponding depths (i.e. one metre and the skin).

6.3 High-resolution satellite – buoy match-ups

There are only a few high-resolution SST match-ups presently available between the Meteosat 8 satellite SST data and the PIRATA data. High-

resolution PIRATA data is recorded and collected once per year and at the time of writing is available until the end of 07/2004, just one month of overlap with the Meteosat 8 SST match-up record. High-resolution PIRATA data for 08/2004 to 07/2005 has been retrieved but will not be publicly available until autumn 2005 (too late for the deadlines of this research).

Thirty days of modelled and observed SSTs at PIRATA buoy location 4 N 38 W, commencing on 01/07/2004 are plotted in Figure 6.3. (Figure 6.4 shows that only one of the match-ups is in the confidence level with more than 50% 'bad' pixels.) This is the only significant record presently available of high-resolution match-ups between a PIRATA buoy and Meteosat 8 SSTs. Figure 6.3 shows 30 days of modelled and observed SSTs at this location, between 01/07/2004 and 30/07/2004. The dashed blue lines are the high-resolution (10 minute) observed SSTs at the buoy's shallowest sensor (1 m). The solid lines are the modelled SST at 1 m (blue) and at the interface (red). Red + are Meteosat 8 SST and the labels are the percentage of pixels in the 'validation box' associated with the confidence level 'excellent'. Unfortunately in this data set, there are no periods of sustained low wind speed during any of the days of this period. Therefore, there are no large diurnal warming events and no significant stratification. Nevertheless, the model simulates SSST in agreement with the Meteosat 8 match-ups within the accuracy of the satellite SST (~ 0.5 K).

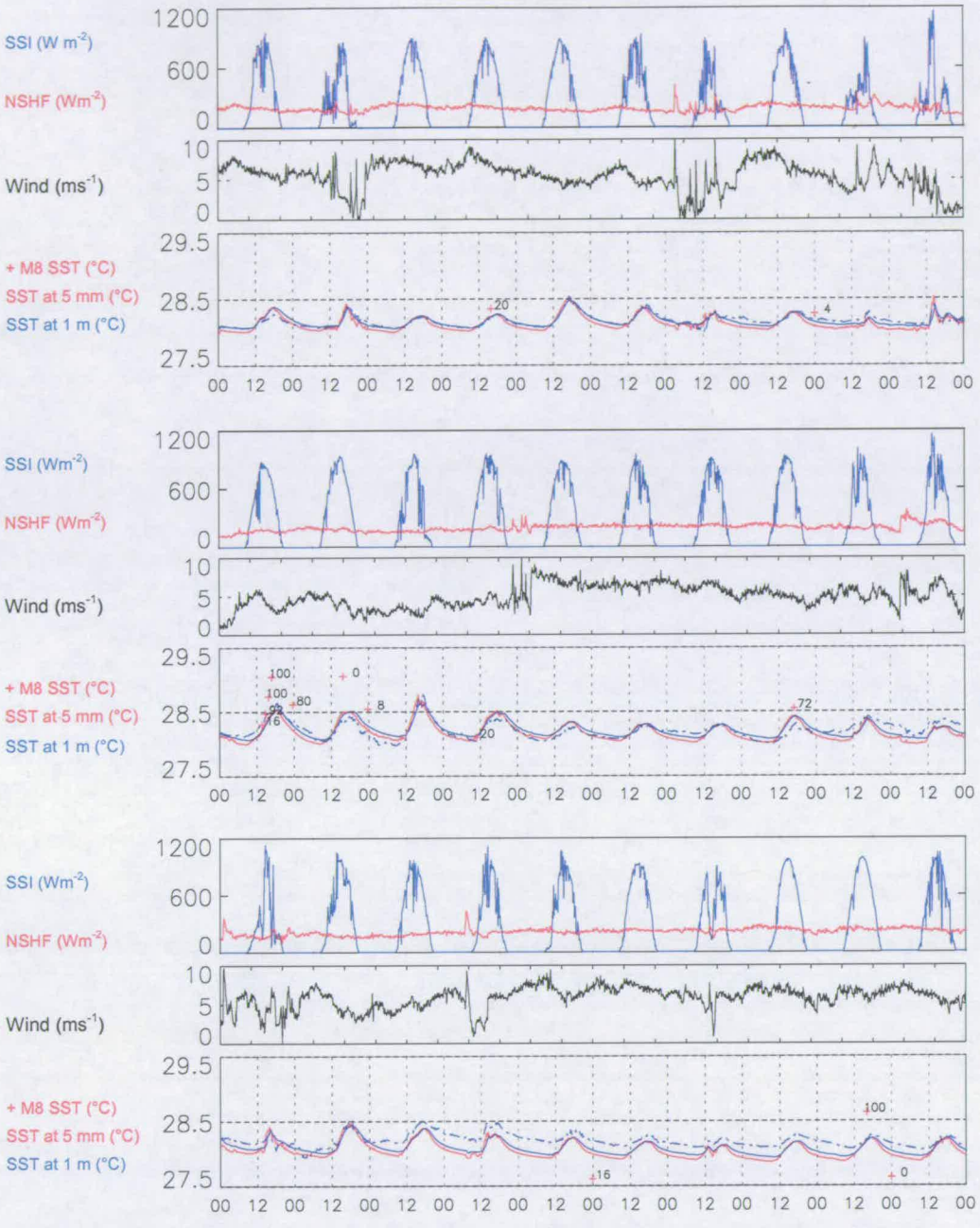

Figure 6.3 30 days of modelled and observed SSTs at PIRATA buoy 4 N 38 W, 01/07/2004 to 30/07/2004. The dashed blue lines are the high-resolution (10 minute) observed SSTs at the buoy's shallowest sensor (1 m). The solid lines are the modelled SST at 1 m (blue) and 5 mm (red). Red + are Meteosat 8 (M8) SST and the labels are the percentage of pixels in the 'validation box' associated with the confidence level 'excellent'.

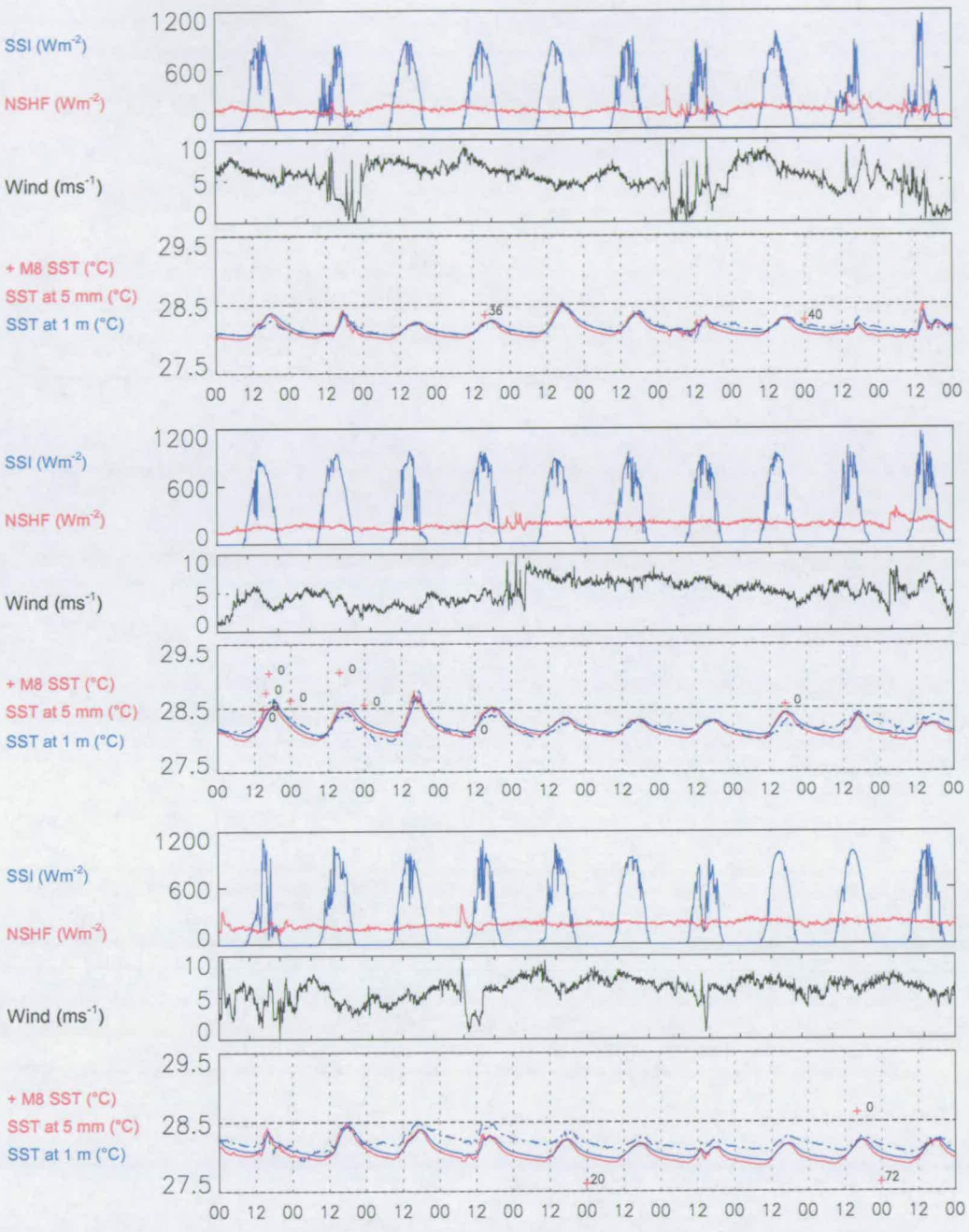

Figure 6.4 Similar to Figure 6.2 except the labels are the percentage of pixels in the 'validation box' associated with the confidence level 'bad'. 30 days of modelled and observed SSTs at PIRATA buoy 4 N 38 W, 01/07/2004 to 30/07/2004. The dashed blue lines are the high-resolution (10 minute) observed SSTs at the buoy's shallowest sensor (1 m). The solid lines are the modelled SST at 1 m (blue) and 5 mm (red). Red + are Meteosat 8 (M8) SST.

6.4 Low-resolution satellite – buoy match-ups

Although there are few Meteosat 8 match-ups with high-resolution buoy data presently available for the period 07/2004 to 07/2005, daily averages of the parameters measured at the PIRATA locations are telemetered from the buoys so that many of the daily records are available. The relevant parameters are solar radiation, meteorology (including winds), SST and subsurface temperatures. Forcing the model with daily averages however is too coarse to model the diurnal variation of SST. A way of simulating the sub-diurnal variation of the forcing fields is described below.

6.4.1 Methodology for producing 6-hourly forcing fluxes

Solar radiation

The daily solar radiation can be scaled to a half rectified sinusoidal form using a clear-sky solar radiation algorithm. The one used here is that of Rosati and Miyakoda (1988). In this way, the diurnal cycle in SSI is defined whilst the integrated solar heating is equal to the daily average recorded at the buoy. The limitation is that timing of fluctuations caused by cloud passage will not be represented in the SSI. Hourly surface solar irradiance (SSI) is calculated as follows:

$$SSI_t = SSI_t^{calc} \times \left[\frac{SSI_{daily}^{buoy}}{\sum_{t=1}^{24} SSI_t^{calc}} \right] \qquad t=1,2,.....24 \qquad (6.1)$$

where SSI_t is the (forcing) surface solar irradiance at time t, SSI_t^{calc} is the SSI calculated by the clear sky algorithm at time t and the term in square brackets is the ratio of daily SSI from the buoy to the daily calculated clear sky SSI.

Meteorology required for calculating non-solar fluxes

The European Centre for Medium Range Weather Forecasting (ECMWF) produces modelled data with 6-hourly resolution on a grid with spatial resolution of 1.125^{O} (latitude and longitude) that covers the earth's surface. Operational data (see Section 5.3) is available from 1st March 1994 to the present date. Reanalysis data is not available for the match-up period. Although the ECMWF operational data assimilates available observations, the daily averages at the buoy locations will not necessarily be equivalent to the daily averages observed at the buoys. To remedy this, the ECMWF wind fields are scaled each day by the daily averages observed at the buoys. This ensures that on a daily time scale, the ECMWF winds equal the buoy winds but the sub-daily scale variability of the ECMWF data is incorporated. The nominal height of ECMWF wind fields is 10 m whilst the buoy winds are measured at 4 m, so the scaling is done with the assumption that atmospheric stability does not change significantly during each day.

The 6-hourly forcing winds are generated by scaling the 6-hourly ECMWF operational wind speeds in the east and north directions by the daily wind speeds at the buoy, as follows:

$$u_{6hr} = u_{6hr}^{ECMWF} \times \left[\frac{\sqrt{\left(u_{daily}^{buoy}\right)^2 + \left(v_{daily}^{buoy}\right)^2}}{\sqrt{\left(u_{daily}^{ECMWF}\right)^2 + \left(v_{daily}^{ECMWF}\right)^2}} \right]$$

$$v_{6hr} = v_{6hr}^{ECMWF} \times \left[\frac{\sqrt{\left(u_{daily}^{buoy}\right)^2 + \left(v_{daily}^{buoy}\right)^2}}{\sqrt{\left(u_{daily}^{ECMWF}\right)^2 + \left(v_{daily}^{ECMWF}\right)^2}} \right] \qquad (6.2)$$

where $u6_{hr}$ and $v6_{hr}$ are the 6-hourly forcing winds and u_{6hr}^{ECMWF} and v_{6hr}^{ECMWF} are the 6-hourly ECMWF operational winds. The term in square brackets is the ratio of the daily wind speed at the buoy to the daily ECMWF wind speed.

Before employing this method for the match-up simulations, a test is carried out using high-resolution *in situ* data.

6.5 Testing this methodology

A test is carried out with a high resolution data set within the period of the operational ECMWF data, i.e. after 1st March 1994. ECMWF operational wind speed data at 15 N 61 E in the Arabian Sea are compared with high-resolution *in situ* wind-speed data in Figure 6.5 for the period 19/02/1995 to 01/03/1995. The ECMWF data compare well to the *in situ* data for much of the first half of the period but poorly in the second half of the period. The RMS of residuals between ECMWF operational wind speeds and high-resolution wind speeds is 2.11 m s^{-1}.

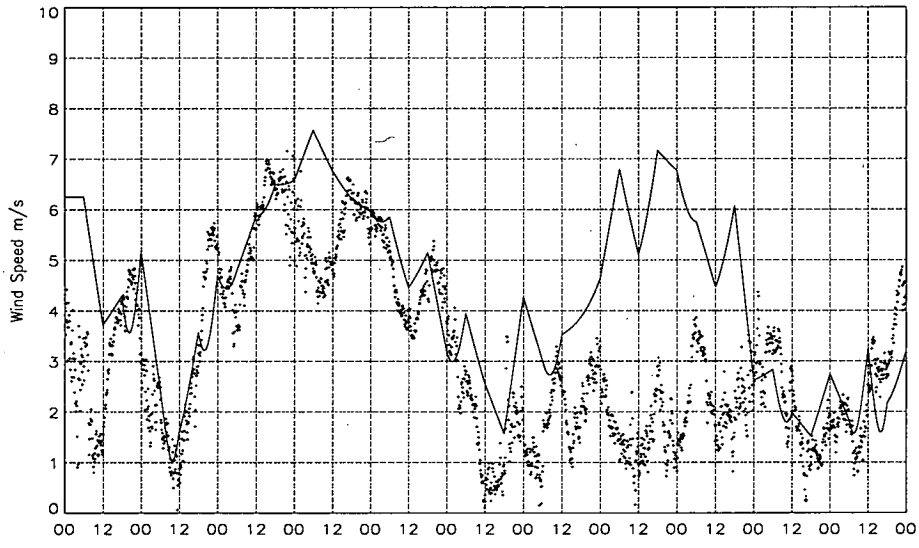

Figure 6.5 Wind speed from ECMWF operational forecast at the buoy location (solid line) compared with high resolution (7.5 minute) *in situ* wind speed data at the buoy (dots). Arabian Sea: 15 N 61 E, 19/02/1995 to 01/03/1995.

The ECMWF operational winds are scaled with daily average wind speed following the method given in Section 6.5 and are compared to the *in situ* wind

speeds in Figure 6.6. The agreement for the entire period is clearly much improved. Diurnal scale variations of the ECMWF data are still apparent in the scaled winds. The RMS of residuals between the scaled wind speeds and high-resolution wind speeds is 0.89 m s^{-1}.

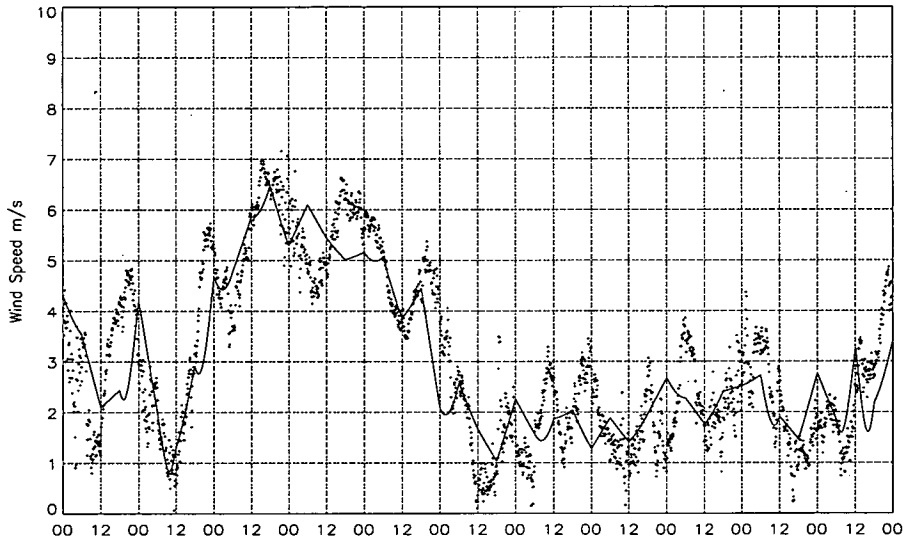

Figure 6.6 Wind speed from ECMWF operational forecast at the buoy location (solid line) is scaled by the average daily wind from the buoy *in situ* measurement. The scaled ECMWF wind is compared to the high resolution (7.5 minute) *in situ* wind speed data at the buoy (dots). Arabian Sea: 15 N 61 E, 19/02/1995 to 01/03/1995.

Modelled SSTs using ECMWF operational wind speeds before scaling are shown in Figure 6.7 and after scaling they are shown in Figure 6.8. It is evident from Figure 6.8 that by scaling the ECMWF winds with daily *in situ* winds, there is a significant improvement in modelled SST at 0.17 m compared to using the original ECMWF operational winds.

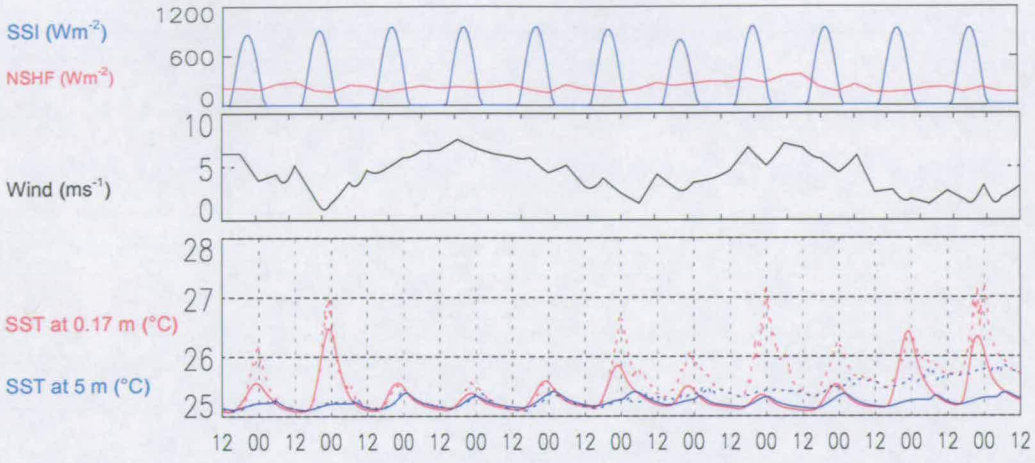

Figure 6.7 Modelled SSTs at 15 N 61 E in the Arabian Sea 19/02/1995 to 01/03/1995, forced with calculated SSI scaled with daily *in situ* SSI and ECMWF operational meteorology (6 hourly).

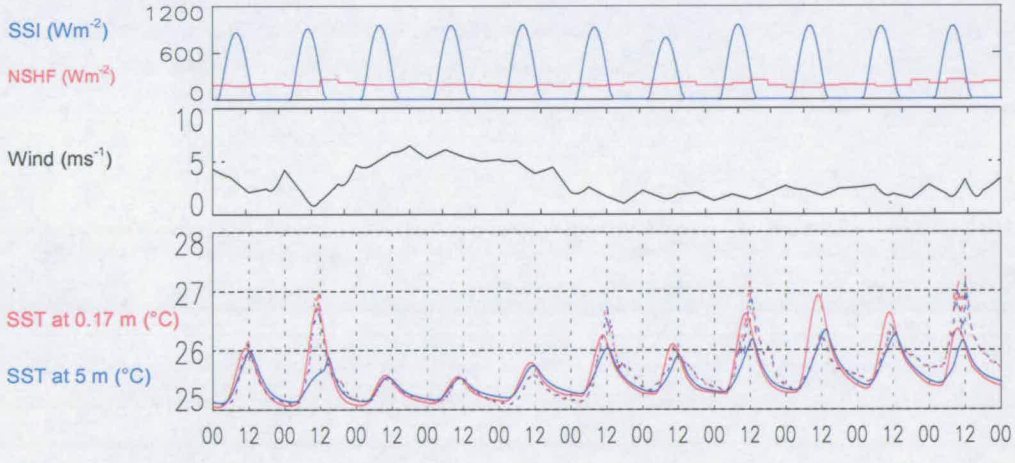

Figure 6.8 Modelled SSTs at 15 N 61 E in the Arabian Sea 19/02/1995 to 01/03/1995, forced with calculated SSI scaled with daily *in situ* SSI and ECMWF operational meteorology (6 hourly), rescaled with *in situ* meteorology.

The RMS of residuals (modelled vs. observed SSTs) from forcing with scaled ECMWF operational winds compared to forcing with original ECMWF operational winds and also *in situ* forcing data are given in Table 6.1.

Forcing combination. Arabian Sea, 15 N 61 E.	RMS of residuals (°C)		
	SST at 0.17 m	SST diurnal amplitude	Stratification
High-resolution SSI and winds.	0.19	0.20	0.20
High-resolution winds and calculated clear sky SSI scaled with daily *in situ* SSI.	0.19	0.27	0.18
6-hourly winds and high-resolution SSI	0.34	0.59	0.37
ECMWF operational winds and calculated clear sky SSI scaled with daily *in situ* SSI.	0.42	0.95	0.30
ECMWF winds scaled to daily buoy average and calculated clear sky SSI scaled with daily *in situ* SSI.	0.23	0.55	0.21

Table 6. 1 RMS of residuals of SST (modelled versus observed at top sensor) for the Arabian Sea for four forcing combinations. (15 N 61 E, 19/02/1995 to 01/03/1995).

There is little loss in model skill when using calculated SSI scaled with daily SSI instead of high-resolution SSI but this is to be expected because this period appears to be fairly cloud free i.e. the high-resolution SSI is similar to calculated clear-sky SSI for most of the days. Model skill would likely be affected more with this method if more cloud were present in the forcing data. This would be difficult to test because a fully validated method of determining the fluxes with cloudy conditions (without explicit cloud observations) is not available (see Section 3.3.1).

The model forced with scaled ECMWF winds predicts SSTs slightly better than the model with 6-hourly wind fields with respect to the properties given in Table 6.1. This test has been conducted with just one data set but the results show that the method is viable when high-resolution forcing data are not

available. PIRATA and TAO high-resolution data are collected only once per year and so this method is useful for modelling SSTs prior to the availability of the high-resolution data.

Figure 6.9 to Figure 6.12 are simulations at PIRATA buoys, forced with ECMWF winds scaled with *in situ* daily winds and calculated SSI scaled with *in situ* daily SSI. None of the match-ups plotted have boxes with 50% or more pixels in the 'bad' confidence level. The skin SSTs plotted in these figures is an adjustment to the model top layer temperature using the modified parameterisation of Saunders (1967) (see Chapter 1).

At buoy location 6 S 10 W, most of the modelled SSSTs agree with Meteosat 8 match-up SSTs within the accuracy of the satellite retrievals (~ 0.5 K rms). The only match-up that does not agree within this accuracy is more than a degree below the *in situ* SST at 1 m. Possible explanations are cloud or aerosol contamination. The warming phase of the diurnal cycle of the last two days at this buoy (Figure 6.10) is modelled in good qualitative agreement with the Meteosat 8 SSTs. The diurnal amplitude of the Meteosat 8 SSSTs is 0.75 °C and 0.60 °C for the last two days and agrees surprisingly well with the modelled skin SST diurnal amplitudes of 0.75 °C for both days considering the scatter expected with retrieval accuracy of ~ 0.5 K rms.

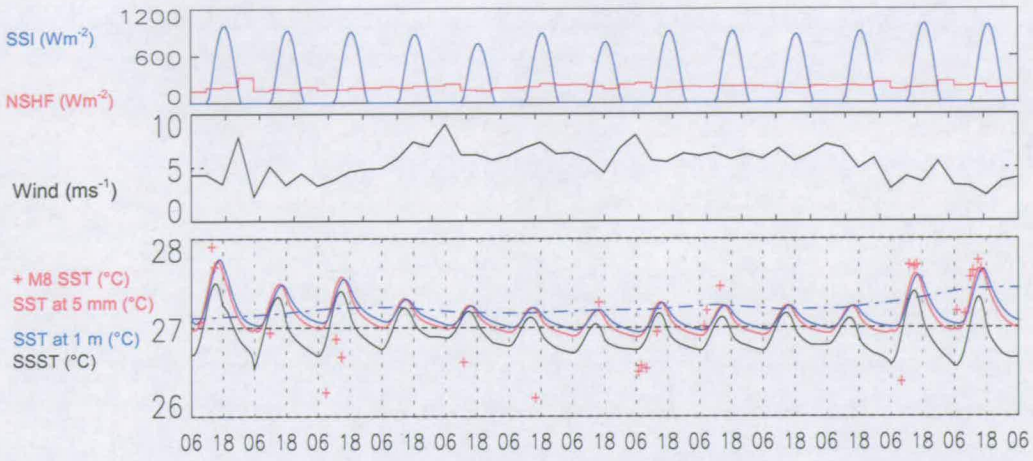

Figure 6.9 Meteosat 8 (M8) SST match-ups with PIRATA buoy at 6S10W, 26/01/2005 to 07/02/2005. The dashed lines are observed SST at 1m (the shallowest PIRATA buoy sensor). The red + are the Meteosat 8 SST at the buoy location.

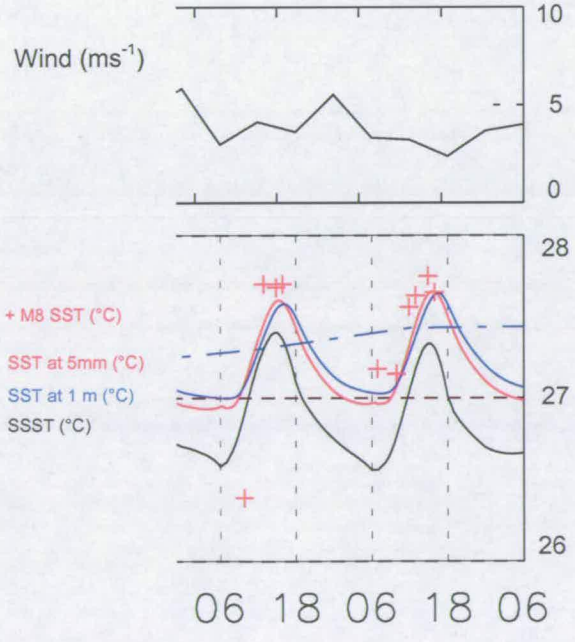

Figure 6.10 Enlargement of the last two days of the simulation shown in Figure 6.9

At buoy location 0 N 23 W (Figure 6.11), the model SSTs are in agreement with Meteosat 8 SSTs (within the accuracy of the satellite retrievals) for those days where advection is not significant. Considerable advection occurs on day 7 (Figure 6.11 a) as can be seen in the one metre *in situ* temperature. The warming of SST is over two degrees in one day and the wind speeds are too high for this to be a diurnal effect. However, the diurnal cycle of SSST compares well to the Meteosat 8 SSTs on days 4, 5 and 6 of this 10 day period with diurnal amplitudes of satellite SSTs agreeing within 0.2 °C of the modelled diurnal amplitude of SSST for these three days

The model was reinitialised on day 11 (Figure 6.11 b) but the SSTs of this next period of 10 days is also affected by advection.

Qualitatively, the modelled diurnal cycle of SSST in the last 8 day period (Figure 6.11 c) is similar to the Meteosat 8 SST diurnal cycle on days 4 and 7 with diurnal amplitudes of satellite SSTs again agreeing within 0.2 °C of the modelled diurnal amplitude of SSST (for day 4, the diurnal amplitude of satellite SSST must be defined as maximum day minus minimum following-night SST)

At buoy location 0 N 35 W, SSTs on days 1 and 2 compare well to the Meteosat 8 SSTs. Only day 2 can really be analysed for diurnal amplitude and the agreement is again better than 0.2 °C. The second half of the simulation is affected by advection.

Diurnal cycles of SSST appear to be resolved in many of the Meteosat 8 match-ups even though the expected scatter ~ 0.5 K would suggest that they should be obscured by noise. Nevertheless, it is encouraging that modelled diurnal amplitudes of SSST agree with the Meteosat 8 match-up SSTs to within 0.2 °C.

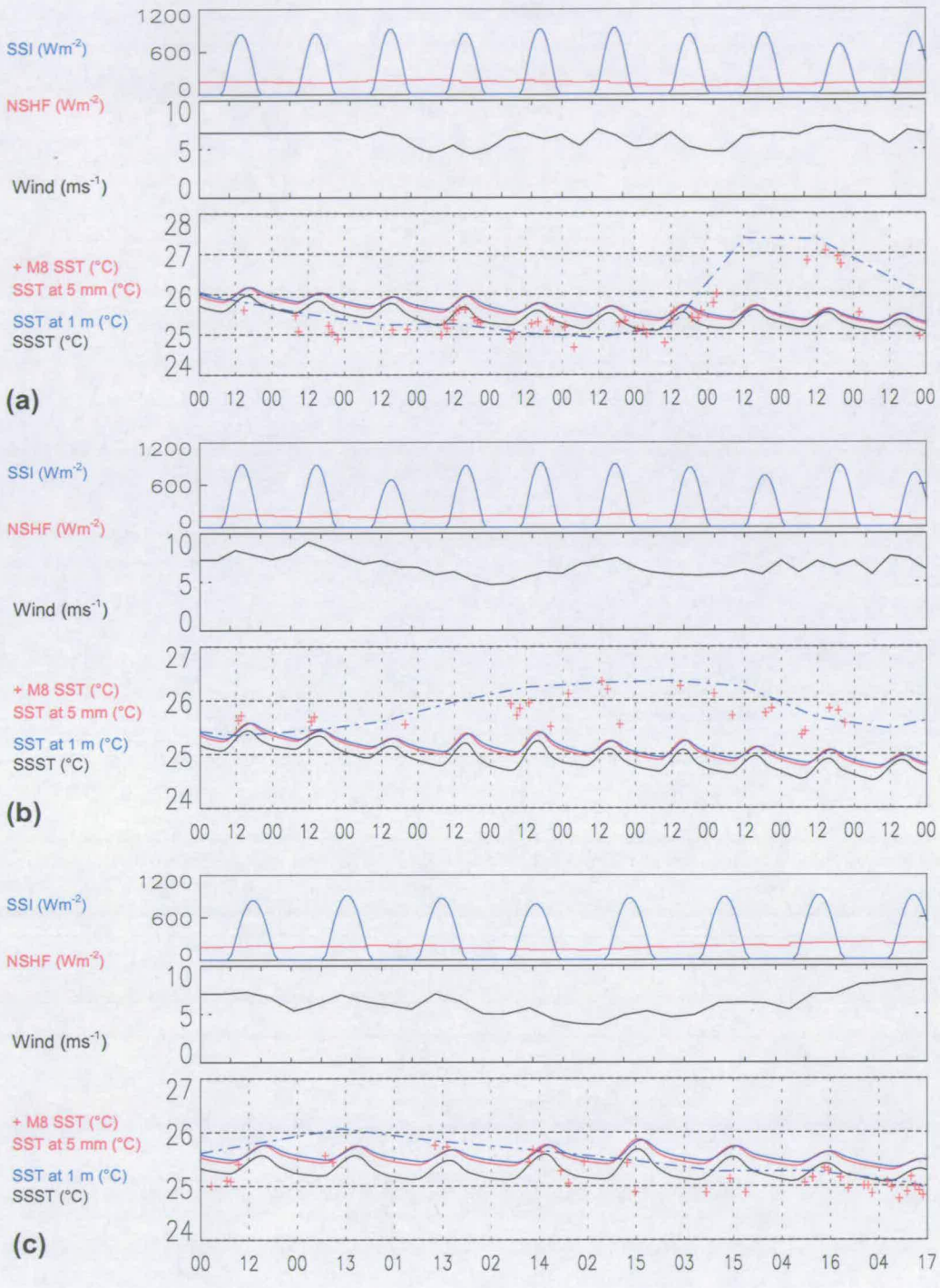

Figure 6.11 Meteosat 8 (M8) SST match-ups with PIRATA buoy at 0 N 23 W. The dashed lines are observed SST at 1m (the shallowest PIRATA buoy sensor). The red + are the Meteosat 8 (M8) SST at the buoy location.

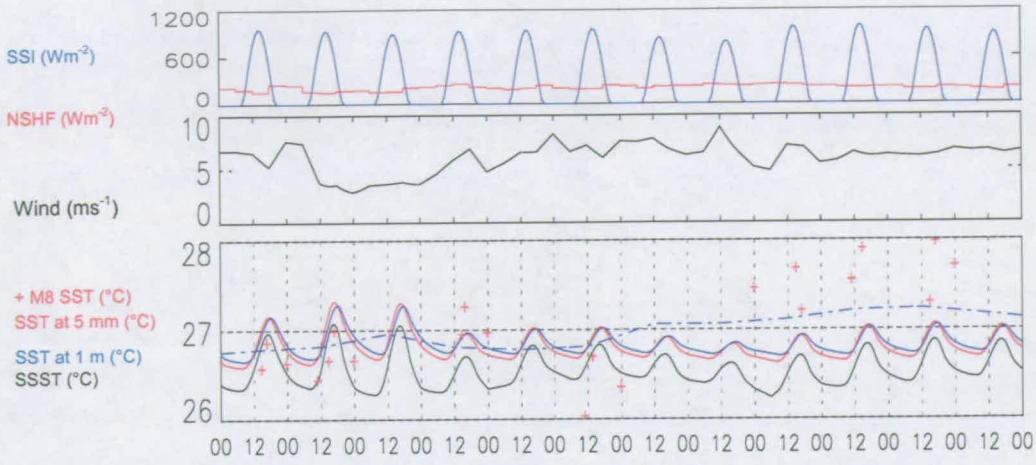

Figure 6.12 Meteosat 8 (M8) SST match-ups with PIRATA buoy at 0N 35W. The dashed lines are observed SST at 1m (the shallowest PIRATA buoy sensor). The red + are the Meteosat 8 SST at the buoy location.

6.6 Chapter 6 summary

A model simulation, forced with high-resolution *in situ* data was compared with Meteosat 8 satellite SST match-ups for the location 4 N 38 W. Unfortunately, there were only a few satellite match-ups for the location and period when the high-resolution *in situ* data were available. The modelled SSTs did agree with the Meteosat 8 SSTs within the accuracy of the satellite retrievals but a good assessment of the model skill in simulating warming or cooling phases or timing of the diurnal cycle could not be made.

A method was developed to make use of an alternative source of data (ECMWF operational meteorology) in conjunction with *in situ* daily data for other locations and time periods in the PIRATA record when more Meteosat 8 match-ups were available. The method showed some success in simulating the diurnal cycle and is a useful tool for modelling SSTs prior to availability of high resolution *in situ* data.

Diurnal warming of SSTs in the satellite retrievals is quite apparent on many of the days of the Meteosat 8 SST match-up data base, where there are sufficient consecutive match-ups to resolve the cycle. Even relatively small warming events are evident and this is surprising given the amount of scatter expected with a retrieval accuracy of ±0.5 K. The retrieval accuracy for the Meteosat 8 SSTs is good overall but the fact that smaller diurnal variations can be detected shows that for stable atmospheric conditions (at a given place on a given day) the relative accuracy of consecutive retrievals is << ±0.5 K. Qualitatively, many of the days modelled with this method show that the modelled SSTs agree with amplitude and timing of warming and cooling phases of the diurnal cycle of SST appearing in the Meteosat 8 SSTs.

Chapter 7 Conclusions and further work

My research aim was to investigate the relationship between SST at any given depth to around 5 m and SST at the air-sea interface under conditions that produce strong diurnal warming. To facilitate this I enhanced a one-dimensional turbulence model by the addition of many options for calculating fluxes and for specifying the distribution of solar radiation in the water column. By conducting an extensive sensitivity test with the enhanced model I found the best combination of options to skilfully model SST with respect to diurnal amplitude, surface stratification and temperature at the depth of the shallowest *in situ* measurements of SST available. The importance of the temporal resolution of forcing data with this model was investigated as was the applicability of sources of forcing data. The modelled interface SSTs at buoy locations in the Atlantic Ocean were compared with collocated match-ups of satellite SSTs. Taken together, my work has shown that a detailed turbulence model can effectively simulate diurnal warming events, using either *in situ* or high temporal resolution analysis fields, provided that the parameterisations used for near surface turbulence and for heat fluxes are carefully chosen. I have inferred and used one effective set of parameter options. Conclusions from each stage of this work are summarised in the remainder of this chapter.

7.1 Ocean model

The first part of my research was to consider what type of model to apply to my research. Numerical models suitable for researching diurnal warming of SSTs were reviewed and a one-dimensional turbulence model (k-ε) was compared with a bulk, mixed layer model (PWP) (Section 2.4). The turbulence model predicted shallower mixed layers at the time of peak SST than the bulk ML model. More stratification occurred in the turbulence model which matched more closely to the observed stratification for the two data sets used for this

comparison (Section 2.4). The turbulence model was selected for the remainder of the research. With the turbulence model, eight stability functions were assessed for suitability in modelling SST in conditions that produce strong diurnal warming. The Kantha and Clayson [1994], (quasi-equilibrium version) was found to be the most suitable (Section 2.5).

7.2 Solar radiation distribution.

Diurnal stratification is driven by solar heating of upper waters. A review of solar heating models shows that they are generally too simplified for the purpose of detailed study of diurnal warming so next I considered the different options for the solar heating model (Section 3.1).

To model the ocean heating from short-wave radiation, SSI was first divided into a number of discrete wavelength bands. The fractions of SSI in each band were obtained from a number of sources including the literature and two radiative transfer models, COART and MODTRAN. Wavelength dependent attenuation lengths of the entrant solar radiation within the water column were obtained from the literature.

SSI fractions derived by radiative transfer modelling, showed that the models presently used in 1-d ocean models (2 band and 9 band) do not accurately represent SSI distribution in the tropical regions. The fractions in the 9 stream model of Paulson and Simpson (1981) do not appear to have been reviewed or revised since they were first published in the early part of the 1900s (1901 to 1933). Fractions of SSI in discrete bands, of width 10 micrometres, were found for several locations in the tropics with radiative transfer models and these fractions differed markedly from those given in the literature. For example, 8.0 % of the solar radiation is assigned to band 5 in the Paulson and Simpson (1981) model, whereas only 5.5 % of SSI is calculated for this band using the radiative transfer model MODTRAN. When the SSI is high, e.g.

1000 W m^{-2}, the difference between the models for just this band is 25 W m^{-2} (Section 3.1.8).

New radiation distributions were derived, including a new 9 band model and a 278 band model (Section 3.1). The geometry of the incident solar radiation was also included in the model to further complete the physics of solar heating. The sensitivity analyses that were carried out (Section 4.7) show that one-dimensional turbulence models can benefit significantly from these revised models when modelling diurnal amplitudes of SST. The improvement in the RMS of residuals of modelled SST with new SSI fractions over the 9 band P&S (1981) SSI fractions, is as much as 0.2 K for top sensor SST and diurnal amplitude and 0.1 K improvement for stratification (with all else being equal).

7.3 Modelled SST sensitivity to fluxes, SSI distribution and turbulence model

An extensive sensitivity test of parameters that were expected to have the most influence on diurnal warming (fluxes, distribution of solar radiation in the ocean and wind induced mixing in the water column) was carried out with 200 combinations of options tested (Chapter 4). The best combination of options of the enhanced model is significantly improved over the public domain version in 3 important properties of modelling SST in conditions of strong diurnal warming: interface SST, diurnal amplitude (minimum night to maximum day SST), and surface stratification. Significant improvement with respect to these three properties was shown with the enhanced model over the original model, with The RMS metrics of interface SST were improved by as much as 0.5 K, those of diurnal amplitude by as much as 0.4 K and those of stratification as much as 0.5 K (Section 4.9).

7.4 Model sensitivity to forcing data resolution

The sensitivity of model skill to time resolution of the SSI and wind speed forcing was investigated. The RMS metrics are not so affected by worsening SSI resolution as they are by worsening wind-speed resolution (Section 5.1). The RMS metrics worsen progressively with degradations in the time resolution of wind speed, with significant worsening of the metrics when time resolution is greater than of order half an hour. SSI time resolution, in contrast, must be degraded to of order 2 hours before significant worsening of the metrics is observed.

Although the model skill was shown to be sensitive to only small degradations of wind speed resolution, the diurnal cycle can be modelled using 3 hourly wind and meteorology with useful agreement to the observations. When comparing the metrics of modelled SST to observed SST, for the Arabian Sea data set, there was very little loss in performance in comparison to the high-resolution 7.5 minute data.

The contrast between 6-hourly wind speeds and higher resolutions is particularly apparent for the Arabian Sea data set. The six hourly wind speed data can also model the diurnal cycle but there is a significant loss in performance.

7.5 Sources of data alternative to *in situ* data

For the vast majority of the ocean, *in situ* meteorology is not available. Alternatives to *in situ* data, with the advantage of greater spatial coverage can be used to force the model and still obtain predictions of diurnal variability response suitable for the purpose of extending the modelling of SSTs to the global ocean. The research of Section 5.2 suggests that ECMWF ERA 40 reanalysis data is as good as 6-hourly *in situ* data for the purpose of modelling diurnal warming.

A method was developed to make use of NWP data (ECMWF operational meteorology) in conjunction with *in situ* daily data for the purpose of modelling the diurnal cycle at PIRATA locations for periods when Meteosat 8 match-ups were available (chapter 6). The method showed some success in simulating the diurnal cycle and is a useful tool for modelling SSTs prior to the availability of high resolution *in situ* data.

7.6 Modelled SSTs compared to satellite SSTs

Diurnal warming of SSTs in the satellite retrievals is quite apparent on many of the days of the Meteosat 8 SST match-up data base, where there are sufficient consecutive match-ups to resolve the cycle. Even relatively small warming events are evident. The retrieval accuracy for the Meteosat 8 SSTs is good overall but the fact that smaller diurnal variations can be detected shows that for stable atmospheric conditions (at a given place on a given day) the relative accuracy of consecutive retrievals is << 0.5 K. Qualitatively, many of the days modelled with this method show that the modelled SSTs agree with the amplitude and timing of warming and cooling phases of the diurnal cycle of SST appearing in the Meteosat 8 SSTs. It may be possible to model large-scale diurnal variability with some accuracy from NWP fields. This is a useful result, since it supports the use of the model for exploring how to parameterise diurnal variability (for correcting SSTs) or use of it for directly correcting for diurnal variability when merging SSSTs obtained at different times of day.

7.7 Further Work

7.7.1 Validation of the model for large diurnal amplitudes

The new model could be further validated with Meteosat 8 SST match-ups as longer records of match-ups with high resolution PIRATA buoy data become available. Meteosat 8 SST match-ups with higher diurnal amplitudes than were available at the time of this research will test the model's skill at predicting strong surface stratification. The diurnal amplitude can exceed 6 K (Stuart-Menteth et al., 2003) and therefore it is important to know the model's accuracy when large diurnal amplitudes occur. This would support the validity of the model as a tool to estimate bulk SSTs from satellite SSTs or to assimilate satellite SSTs into ocean modelling.

7.7.2 Investigation of more properties of the diurnal cycle

There are features of the diurnal cycle of SST other than diurnal amplitude that are important to the interpretation of measurements of SSTs. These include the timing of the peak of SST during the cycle and also the shape of the time series of SST. Some very preliminary work is shown here using artificial data to illustrate the model response to the timing of changes in wind speed and changes in incident radiation due to cloud passage.

SST response to timing of a rapid increase in wind speed

The SST response to the timing of a rapid increase in wind speed (wind-burst) is shown in Figure 7.1. Here, the timing of the wind-speed increase is varied hourly from peak wind at 12:00 to peak wind at 15:00 and the time-evolution of SST response is shown. The model predicts that the magnitude of SST and the shape of the SST time-series depend on the time of day that a burst of wind arrives.

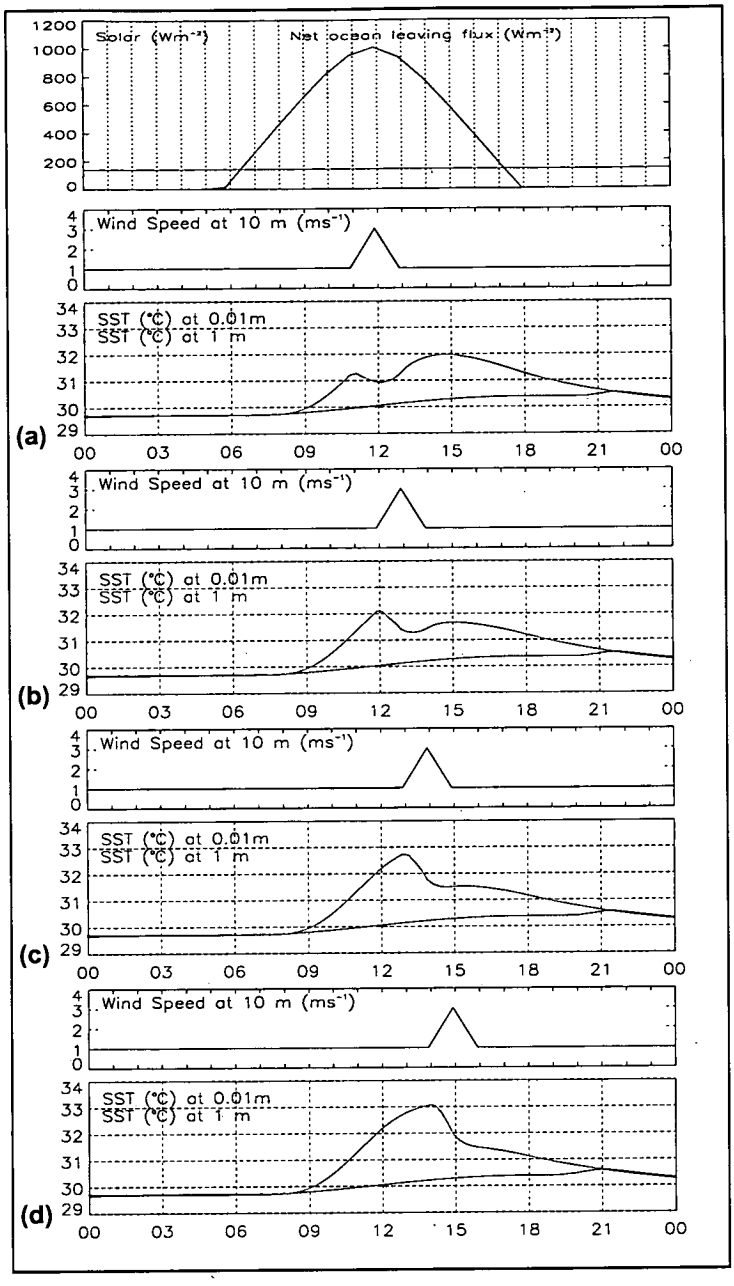

Figure 7. 1 Time dependent response of SST to an increase in windspeed. (a), (b), (c) and (d): wind bursts at 12:00, 13:00, 14:00 and 15:00 respectively.

In this test, it is clear that the timing of the SST maximum at 1 cm is affected by the timing of the wind-burst. The surface heat fluxes are set identical for each wind-burst scenario. The largest time difference (3 hours) in the peak of

SST at the surface (1 cm) is observed between Figure 7.1 (a) (wind-burst at 12:00) and figure 5.5 (b) (wind-burst at 13:00). The peaks of SST in figures 5.5 (c) and 5.5 (d) (wind bursts at 14:00 and 15:00 respectively) occur earlier than the SST maximum for the wind burst at 12:00. The relationship between the timing of the wind burst and the timing of the SST maximum is not linear. The magnitude of SST maximum is also affected by the timing of the wind-burst. The largest difference in SST maximum occurs between the wind burst at 12:00 (a) and the wind burst at 15:00 (d).

Further research is required to assess whether such conditions occur in real data sets and with sufficient frequency to warrant consideration. These initial findings show that there could be implications for SST predictions from satellite measurements. For orbiting satellites, it may not be possible to relate the SST determined at the time of the satellite overpass to the actual peak SST. If detailed surface wind data are available, then the diurnal cycle of SST could be modelled and the peak SST determined from a combination of the modelled and satellite SSTs.

SST response to timing of partial cloud cover.

Cloud conditions will also affect the shape and magnitude of the SST profile. Figure 7.2 (a) shows the SST response to a build up and then dispersal of partial cloud cover in the morning. Figure 7.2 (b) shows the SST response to a build up and then dispersal of partial cloud cover in the afternoon.

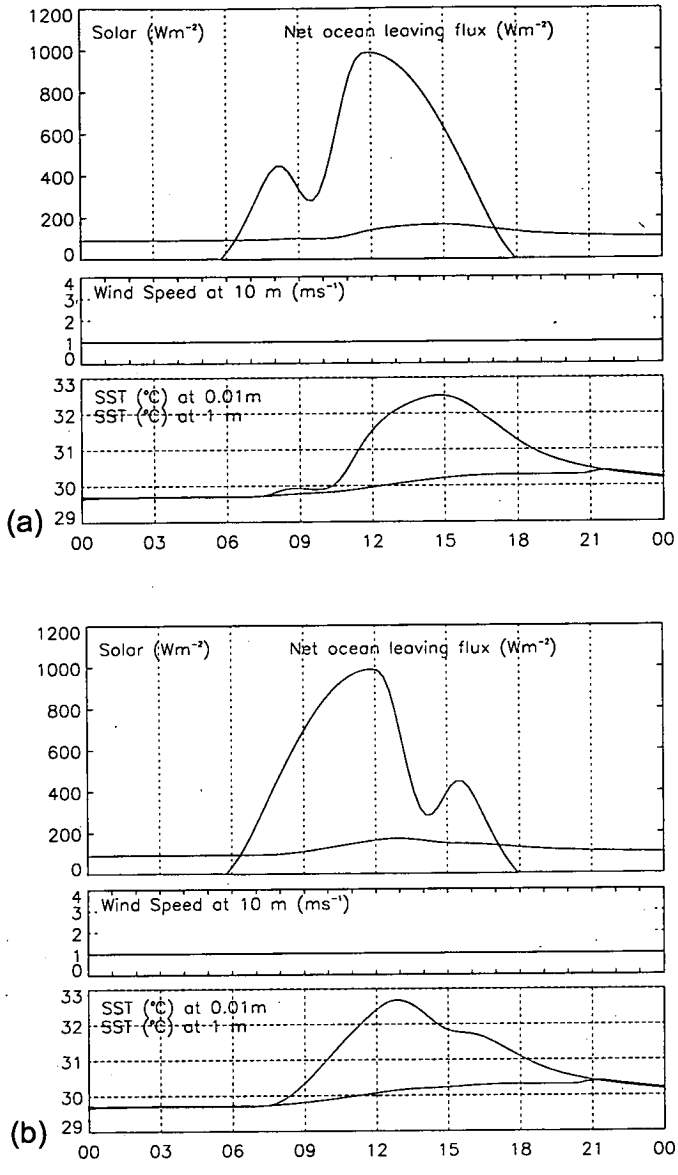

Figure 7. 2 Response of SST to timing of cloud passage. Wind speed kept constant at 1 ms^{-1}. (a) cloud in the morning. (b) cloud in the afternoon

In scenario (a), the morning SSI is reduced by cloud and the diurnal warming of the sea surface is suppressed until the cloud begins to dissipate. The heat budget is the same for both scenarios and there is little difference between the magnitudes of the peak SSTs.

Although the solar-radiation peak is the same magnitude and at the same time (midday) for both these scenarios, the response of the peak SST is 2 hours later for the morning cloud scenario (a) than for the afternoon cloud scenario (b). With scenario (b), most of the day's solar heating occurs in the morning. The peak SST has already passed before the cloud builds up. Further work could investigate the timing of the peak SST to cloud passage inferred from satellite data or surface solar irradiance measurements.

7.7.3 Longer time scales

In Chapter 1, it was put forward that the diurnal cycle of SST is important to the modelling of processes with intraseasonal timescales (30 to 60 days), such as the Madden-Julian Oscillation (MJO). Bernie *et al.* (2003), show that the rectification of the diurnal cycle of SST onto the daily mean SST accounts for about one third of the magnitude of intraseasonal variability of SST associated with the MJO in the west Pacific warm pool. This research employed the so called K-Profile Parameterisation (KPP) model with a top layer vertical grid resolution of 1 metre.

The improved GOTM model has been calibrated and validated to skilfully predict diurnal cycling of SST. The new model may be able to predict the intraseasonal variability of SST in the tropics with improved accuracy over previous studies. Further work on modelling intraseasonal variablilty of SST with the improved GOTM model could investigate the effect of detailed inclusion of diurnal variability using high resolution forcing data versus completely ignoring the diurnal cycle of SST. Scenarios within those extremes

could also be investigated to ascertain the minimum resolution of forcing data required to accurately model SST variability on MJO timescales.

Abdella, K. and S. J. D. d'Allessio, A parameterization of the roughness length for the air-sea interface in free convection. *Environmental Fluid Mechanics* 3 (1): 55-77, Mar 2003.

Andrews D.G., An introduction to atmospheric physics. *Cambridge University Press*, 2000.

Bernie D. J., S. W. Woolnough, J. M. Slingo and E. Guilyardi,. Modelling Diurnal and Intraseasonal Variability of the Ocean Mixed Layer. *Journal of Climate*, 18, 8, 1190-1202, 2005.

Beljaars, A. C. M., The parametrization of surface fluxes in large-scale models under free convection. *Q. J. R. Meteorol. Soc.,* 121, 255-270, 1994.

Brunt, D., Notes on Radiation in the Atmosphere. *Quart. J. Roy. Meteor. Soc.,* 58, 389-418, 1932.

Buiteveld, H., J. M. H. Hakvoort and M. Donze, The optical properties of pure water, *SPIE Proceedings on Ocean Optics XII,* edited by J. S. Jaffe, 2258, 174-183, 1994.

Burchard, H. and H. Baumert. On the performance of a mixed-layer model based on the *k-epsilon* turbulence closure. *J. Geophys. Res.*, 100:8523-8540, 1995.

Burchard, H., Karsten Bolding, and Manuel Ruiz Villarreal. GOTM - a general ocean turbulence model. Theory, applications and test cases. *Technical Report EUR 18745 EN, European Commission*, 1999.

Burchard, H., Ole Petersen, and Tom P. Rippeth. Comparing the performance of the Mellor-Yamada and the *k-epsilon* two-equation turbulence models. *J. Geophys. Res.*, 103:10543-10554, 1998.

Burchard, H., Applied turbulence modelling in marine waters, volume 100 of Lecture Notes in Earth Sciences. *Springer, Berlin, Heidelberg, New York*, 2002.

Charnock, H., Wind stress on a water surface. *Quart. J. Roy. Meteor. Soc.,* 81, 639–640, 1955.

Clark, N. E., L. Eber, R. M. Laurs, J. A. Renner, and J. F. T. Saur. Heat exchange between ocean and atmosphere in the Eastern North Pacific for 1961-1971. *Technical Report NMFS SSRF-682, NOAA, U.S. Dept. of Commerce, Washington, D.C.*, 1974.

Clayson C. A., and J. A. Curry, Determination of surface turbulent fluxes for the TOGA COARE: comparison of satellite retrievals and in situ measurements. J. Geophys. Res., 101, 28,525-28,528, 1996.

Curry, J.A., P. J. Webster, Thermodynamics of atmospheres and oceans, pp 471. *Academic Press*, 1999.

Defant A., Physical oceanography. *Pergamon Press*, 1961.

Deleersnijder, E. and P. Luyten, On the practical advantages of the quasi-equilibrium version of the Mellor and Yamada level 2.5 turbulence closure applied to marine modelling. *Applied Mathematical Modelling*, 1994 Vol. 18, pt. 5 pp 281-287.

Denman, K. L. and M. Miyake, Behavior of Mean Wind, Drag Coefficient, snd Wave Field in Open Ocean. *Journal Of Geophysical Research*, 78 (12): 1917-1931, 1973.

Donlon C. J., Minnett P. J., Gentemann C., Nightingale T. J., Barton I. J., Ward B., Murray M. J, Toward improved validation of satellite sea surface skin temperature measurements for climate research. *Journal of Climate* 15(4), 353-369, 2002.

Fairall C.W., E. F. Bradley, J. E. Hare., A. A. Grachev, J. B. Edson., Bulk parameterization of air-sea fluxes: Updates and verification for the COARE algorithm. *Journal Of Climate*, 16 (4): 571-591, 2003.

Fairall, C. W., E. F. Bradley, D. P. Rogers, J. B. Edson, and G. S. Young, Bulk parameterization of air-sea fluxes for TOGA-COARE. *J. Geophys. Res., 101*, 3747-3764, 1996a.

Fairall, C.W., E. F. Bradley, J.S. Godfrey, J.B. Edson, G.S. Young, and G.A. Wick, Cool skin and warm layer effects on the sea surface temperature. J. Geophys. Res., 101, 1295-1308, 1996b.

Flament, P., J. Firing, M. Sawyer and C. Trefois, Amplitude and horizontal structure of a large sea surface warming event during the Coastal Ocean Dynamics Experiment. *J. Phys. Oceanogr.*, 24, 124-139, 1994.

Fung I. Y., D. E. Harrison and A. A. Lacis, On the Variability of the Net Longwave Radiation at the Ocean Surface. *Reviews Of Geophysics* 22 (2): 177-193, 1984.

Garratt, J. R., The Atmospheric Boundary Layer. *Cambridge University Press*, 1992.

Grant, A. L. M. and P. Hignett, Aircraft observations of the surface energy balance in TOGA-COARE. *Q. J. R. Meteorol. Soc.*, 124, pp. 101-122, 1998.

Hale, G. M. and M. R. Querry, Optical constants of water in the 200 nm to 200 μm wavelength region, *Appl. Opt.*,12, 555-563, 1973.

Haney and Davies, Role of Surface Mixing in Seasonal-Variation of Ocean Thermal Structure. *Journal of Physical Oceanography*, 6 (4): 504-510, 1976.

Hasse L., The sea surface temperature devation and the heat flow at the sea-air interface. *Boundary-Layer Meteorology*, 1, 368-379, 1971.

Hastenrath, S., and P. J. Lamb, Heat Budget Atlas Of The Tropical Atlantic And Eastern Pacific Oceans. *The University of Wisconsin Press*, 90 pp., 1978.

Irvine, W. M. and J. B. Pollack, "Infrared optical properties of water and ice spheres," *Icarus*,8, 324-360, 1968.

Jassby, A. and T. Powell, Vertical Patterns of Eddy Diffusion During Stratification in Castle Lake, California. Limnology And Oceanography 20 (4): 530-543, 1975.

Jerlov, N. G., Optical oceanography. Elsevier, 1968.

Kantha L. H. and C. A. Clayson, An improved mixed layer model for geophysical applications. *J. Geophys. Res.*, 99, C12, 25,235-25,266, 1994.

Kantha, L.H., and C. A. Clayson, Small Scale Processes in Geophysical Fluid Flows. *Academic Press*, 2000.

Kondo, J., Air-sea bulk transfer coefficients in diabatic conditions. *Bound.-Layer Meteor.*, *9*, 91-112, 1975.

Kopelevich, O. V., Optical properties of pure water in the 250- 600 nm range, *Opt. Spectrosc.*,41, 391- 392, 1976.

Large, W. G. and S Pond, Open Ocean Momentum Flux Measurements in Moderate to Strong Winds. *J. Phys. Oceanogr* 11 (3): 324-336, 1981.

Large, W. G., J. C. Mcwilliams, S. C. Doney, Oceanic Vertical Mixing - A Review and a Model with a Nonlocal Boundary-Layer Parameterization. *Reviews Of Geophysics*, 32 (4): 363-403, Nov 1994.

Lighthill, M. J., Waves in Fluids. *Cambridge University Press*, 1978.

Morel, A. and L. Prieur, Analysis Of Variations In Ocean Color. *Limnology And Oceanography* 22 (4): 709-722, 1977.

Paulson C. A. and J. J. Simpson., The Temperature Difference Across the Cool Skin of the Ocean. *J. Geophys. Res.*, 86, C11, 11,044-11,054, 1981.

Paulson, C. A. and J. J. Simpson, Irradiance Measurements in the Upper Ocean. *J. Phys. Oceanogr.*, *7*, 952-956, 1977.

Pope, R. M. and E. S. Fry, Absorption spectrum (380-700 nm) of pure water. II. Integrating cavity measurements, *Appl. Opt.*,36, 8710-8723, 1997.

Price J. F., C. N. K. Mooers and J. C. Vanleer, Observation and Simulation of Storm-Induced Mixed-Layer Deepening. *Journal of Physical Oceanography* 8 (4): 582-599, 1978.

Price James. F., R. A. Weller, R. Pinkel, Diurnal Cycling: Observations and Models of the Upper Ocean Response to Diurnal Heating, Cooling and Wind Mixing. *J. Geophys. Res.*, 91, 8,411-8,427, 1986.

Querry, M. R., P. G. Cary and R. C. Waring, Split-pulse laser method for measuring attenuation coefficients of transparent liquids: application to deionized filtered water in the visible region, *Appl. Opt.*,17, 3587-3592, 1978.

Quickenden, T. I. and J. A. Irvin, The ultraviolet absorption spectrum of liquid water, *J. Chem Phys.*,72, 4416-4428, 1980.

Reed R. K., Estimating Insolation over the Ocean. *Journal Of Physical Oceanography,* 7 (3): 482-485, 1977.

Report (Final) of the Joint WCRP/SCOR Working Group on Air-Sea Fluxes, June 2000.

Robinson I. S., Wells N. C. and Charnock H., The sea surface thermal boundary layer and its relevance to the measurement of sea surface temperature by airborne and spaceborne radiometers. *Int. J. Remote Sensing*, 5, 1, 19-45, 1984.

Rodi, W., Examples of Calculation Methods for Flow and Mixing in Stratified Fluids. *Journal of Geophysical Research-Oceans 92* (C5): 5305-5328, May 15 1987.

Rosati, A. and K. Miyakoda, A general circulation model for upper ocean circulation, *J. Phys. Oceanography.* 18, 1601-1626, 1988.

Saunders P. M., The temperature at the ocean-air interface. *J. Atmospheric Sciences*, Vol 24, 269-273, 1967.

Segelstein, D. J., The complex refractive index of water, MS Thesis. *University of Missouri-Kansas City*, 1981.

Simpson, J. J. and T. D. Dickey, Alternative Parameterizations of Downward Irradiance and Their Dynamical Significance. *Journal Of Physical Oceanography*, 11 (6): 876-882, 1981.

Smith, R. C. and K. S. Baker, Optical properties of the clearest natural waters (200-800 nm), *Appl. Opt.*,20, 177-184, 1981.

Smith, S. D., C. W. Fairall, G. L. Geernaert and L. Hasse, Air sea fluxes, 25 years of progress. *Bound.- Layer Meteor.*, 78, 247-290, 1996.

Smith, S. D., Coefficients for sea surface wind stress, heat flux, and wind profiles as a function of wind speed and temperature. *J. Geophys. Res.*, 93, 15,467-15,472, 1988.

Sogandares, F. M. and E. S. Fry, Absorption spectrum (340- 640 nm) of pure water. I. Photothermal Measurements, *Appl. Opt.*,36, 8699-8709, 1997.

Stramma L., P. Cornillon, R. A. Weller, J. F. Price and M. G. Briscoe, Large Diurnal Sea-Surface Temperature Variability - Satellite and Insitu Measurements. *Journal Of Physical Oceanography,* 16 (5): 827-837 May 1986.

Stull, R. B., An Introduction to Boundary Layer Meteorology. *Kluwer Academic Publishers*, 1988.

Taylor, P. K., E. F. Bradley, C. W. Fairall, L. Legler, J. Schulz, R. A. Weller and G. H. White, 1999: Surface Fluxes and Surface Reference Sites. *The Ocean Observing System for Climate - Oceanobs 99*, St Raphael, 25 - 27 October, 1999.

Toba, Y., Ocean Atmosphere Interactions. *Kluwer Academic Publishers*, 2003.

Webster, P. J., The Role Of Hydrological Processes in Ocean-Atmosphere Interactions. *Reviews Of Geophysics,* 32 (4): 427-476, Nov 1994.

Zapadka, T. and S. B. Woźniak, Preliminary comparison between various models of longwave radiation budget of the sea and experimental data for the Baltic Sea. *Oceanologia*, 42(3), 359-369, 2000.